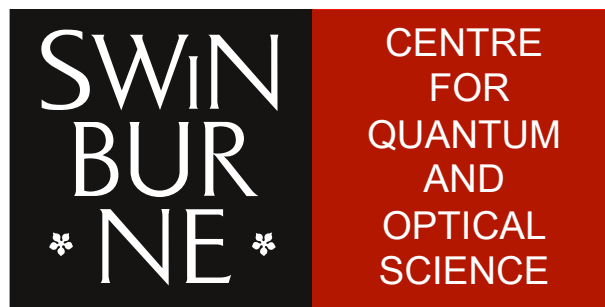


Coherence of a bosonic Josephson junction



Centre for Quantum and Optical Science
Faculty of Science, Engineering and Technology
Swinburne University of Technology
Melbourne, Australia

November 2017

*“Che mi piaci tutti li ragazzi italiano perche’ sono
vera-veramente bravo per fare amore”*

Lia de Bahia

Abstract

Bose-Einstein condensates (BECs) of dilute atomic gases are coherent macroscopic systems with a well defined phase able to interfere and exhibit an interference pattern ultimately given by their phase relationship. If the phase relationship between two BECs randomly changes from realization to realization, it is considered that the two BECs are phase incoherent even though they interfere in each individual realization. In this thesis we present a set of experiments whose aim is to "rephase", i.e. to increase the coherence factor defined as the average of the cosine of the relative phase of two initially incoherent condensates. The original idea was proposed by Dalla Torre et al. in their 2013 paper (Phys. Rev. Lett. 110, 090404, 2013) where the authors dealt with two condensate trapped in a double well potential weakly coupled by tunneling, thus forming an external bosonic Josephson junction and theoretically predicted the existence of universal scaling laws for the time dependence of physical observables, focusing on the time evolution of the coherence factor. We have extended the model to two component Bose-einstein condensates of different hyperfine states trapped in the same magnetic trap and coupled by an external microwave field, i.e. an internal bosonic Josephson junction. This extension of the original idea shows that universal dynamics (particularly rephasing of two independent condensates) can be achieved in both external and internal bosonic Josephson junctions.

We use Ramsey interferometry to obtain information about the phase relationship of two interacting BECs. Our model shows that the effect of a weak coupling com-

bined with the nonlinear interactions experienced by the two-component BECs can rephase an initially incoherent ensemble, giving a well-defined phase relationship to the system. For an incoherent system, we observe a uniform distribution of relative phase ϕ after a given Ramsey evolution time t . For a given evolution time t in the Ramsey interferometer, the relative phase distribution should cluster around $\phi = 0$. Controlling rephasing is no trivial task and it is dependent on how much the wave functions of our two component overlap and how strong is the coupling between them. To increase the atomic interactions, we exploit the intrinsic immiscible behaviour of two wave-functions.

To decrease the influence of technical noise on phase uncertainty, crucial for accurate Ramsey interferometry, a new MW system was implemented in the experimental setup. Our measurements, performed on thermal clouds, clearly show a reduction of the phase diffusion from 0.5 rad/s, obtained using the old apparatus, to 0.1 rad/s. In our quest to increase the interaction strength by minimising wave-function overlapping we explored three different methods to produce spatially separated two-component BEC (2CBEC): independent condensation, fast $\pi/2$ transfer and subsequent collective oscillations and adiabatic transfer to a 50:50 superposition. We attempted to observe the rephasing effect in two-component BEC but unfortunately we could not detect it in our experimental conditions. Possible reasons explaining the lack of direct observation of the rephasing dynamics in 2CBEC, along with all experimental data, are provided in the body of this thesis.

Acknowledgments

During the completion of this project, I had the valuable help and support of various people. First of all, I want to thank my primary supervisor Prof. Andrei Sidorov, who was giving me excellent support during these years of the PhD research. His assistance was extremely valuable. The next person I would like to thank is Prof. Russell McLean, my cosupervisor, who gave valuable support through all the years of the research till the end of my project. Thanks to Prof. Peter Hannaford, who wasn't my supervisor but was always there, to Dr. Yun Li for the excellent theoretical discussions, to Prof. Peter Drummond, for the summer school and the Quantum field theory lectures, to Prof. Margareth Reid (I still have the assignments somewhere, I think under a pile of papers in the lab).

I would like to thank the other members of our group: Yibo, whose discussion were very precious and whose presence was always welcome, Tien, for your exemplar determination, Ivan and Yurii, which have taught me what I know about the subtleties of our setup.

Finally my friends deserve the biggest credit, because life is nothing without friends and so is a PhD. They help you push forward. Of all my friends, three in particular, my closest: Chiara, Elena and Fabio. After them, other great friends: Umberto, with our discussions and his almost prophetic foresight, Run, with all the tennis we played, Pavel, because of his simplicity, the Iranian guys of sunday soccer... I'm sure I'll get the spelling all wrong but I'll try anyway: Ali Rezha, Ali, Rezha (many of them are called like that, apparently it's a popular name in Iran) Masoud, Merbod,

Mohammed, Ben, thanks people, four amazing years! Lawrence and Nigel, I guess the only two Australians I can call friends. Philip, a great friend, even though you left early, too early. But as they say "Leaves early who's dear to the gods".

I almost forgot my mother which has historically been the biggest contributor in all my achievements; this thesis is for you.

Declaration

The work presented in this thesis entitled “Coherence of a bosonic Josephson junction” has been carried out in the Centre for Quantum and Optical Science (CQOS) at Swinburne University of Technology in Melbourne between March 2013 and March 2017. The thesis contains no material that has been accepted for the award of any other degree or diploma. To the best of my knowledge, the thesis contains no material previously published or written by another author, except where due reference is made in the text of the thesis.

Alessandro Brolis

Melbourne, Victoria, Australia

2 November 2017

A handwritten signature in black ink, appearing to read "Ale Brolis". The signature is written in a cursive, flowing style.

Contents

Abstract	iii
Acknowledgments	v
Declaration	vii
List of Figures	xii
List of Tables	xvii
1 Introduction	1
1.1 Thesis structure	5
2 Two-Component BEC	9
2.1 Coupled Gross-Pitaevskii Equations	9
2.1.1 Hydrodynamic equations	12
2.1.2 Ground state and Thomas-Fermi approximation	13
2.1.3 Reduction to lower dimensions	15
2.1.4 Simulation of the non-equilibrium dynamics of 2CBEC	17
3 Experimental Apparatus	19
3.1 Magnetic trapping	20
3.1.1 Interaction of an atom with a magnetic field	20

3.1.2	Quadrupole coils	22
3.1.3	Ioffe-Pritchard trap	25
3.1.4	Magnetic traps on a chip	27
3.2	Laser Cooling	29
3.2.1	The MOT	29
3.2.2	Polarization Gradient Cooling	31
3.2.3	Optical pumping	32
3.3	Hyperfine Manipulation	33
3.3.1	Atomic system	33
3.3.2	Microwave setup	38
3.3.3	Magnetic field calibration	41
3.4	Imaging	42
3.4.1	Absorption imaging	42
3.4.2	Imaging System	45
3.4.3	Dual state imaging, adiabatic passage	49
4	Quantum Noise	53
4.1	The Bloch sphere	53
4.1.1	Ramsey interferometry	57
4.2	Decoherence factors in a Ramsey sequence	59
4.2.1	Standard Quantum Limit	60
4.2.2	Quantum phase diffusion	62
4.2.3	Losses	62
4.2.4	Collisional Shift	64
4.2.5	Inhomogeneous phase growth	65
4.2.6	Interaction with a thermal cloud	66
5	Coherence of thermal clouds and BEC, Experimental results	69

5.1	Experimental sequence and fringe analysis	70
5.1.1	Phase diffusion experiments	71
5.1.2	Quantum Decoherence of BEC experiments	74
5.2	Phase diffusion, results	76
5.2.1	Phase diffusion with Agilent E8257D	77
5.2.2	Phase diffusion with QuickSyn MW synthesizer	80
5.2.3	Inhomogenous dephasing and identical spin rotation effect	84
5.2.4	Other sources of technical noise	86
5.3	Quantum decoherence of a BEC	89
5.3.1	Ramsey interferometry with BEC	90
5.4	Conclusion	95
6	Rephasing dynamics of a bosonic Josephson junction	97
6.1	Double well Josephson junctions	98
6.2	Two component Josephson junction	103
6.3	Universal rephasing dynamics in a quenched Josephson junction	104
6.4	Immiscible 2CBEC and nonlinear interactions	112
7	Rephasing Dynamics of a bosonic Josephson Junction, experimen-	
	tal results	117
7.1	Independent Condensation	119
7.2	Rephasing through engineered phase	123
7.2.1	Rephasing with a fast $\pi/2$ splitting	126
7.2.2	Adiabatic transfer to 50:50 superposition	134
7.3	Conclusions	146
8	Summary and future directions	153
	Bibliography	156

Publications

173

List of Figures

3.1	Zeeman split of the hyperfine levels $F=2$ and $F=1$ in ^{87}Rb calculated using the Breit-Rabi formula	22
3.2	Schematics of the switch used to drive the quadrupole coils	26
3.3	^{87}Rb energy levels together with the transitions used in the laser cooling stage.	31
3.4	Optical pumping transitions	34
3.5	Ground state of ^{87}Rb showing the two hyperfine levels $F=1$ and $F=2$ and their Zeeman splitted sublevels.	35
3.6	Energy difference of the levels $ F = 1, m_F = -1\rangle$ and $ F = 2, m_F = 1\rangle$ for different values of the external magnetic field	36
3.7	MW transitions and RF transitions used in the experiments	39
3.8	MW setup scheme	41
3.9	Microwave spectroscopy on the σ^+ transition $ F = 1, m_F = -1\rangle$ to $ F = 2, m_F = 0\rangle$	43
3.10	Imaging system setup	47
3.11	Absorption images acquired using different imaging setups	48
3.12	Adiabatic passage technique	51
3.13	Adiabatic population transfer efficiency	52
4.1	Bloch sphere representation	56

4.2	Ramsey evolution on a Bloch sphere	58
4.3	Bloch sphere representation of a coherent state	61
4.4	Quantum phase diffusion on a Bloch sphere	63
4.5	Loss induced dephasing	65
4.6	Simulated time evolution of the local relative phase in the presence and absence of losses	68
5.1	Phase uncertainty evolution in a Ramsey sequence. Adapted from [1]	70
5.2	Experimentally measured axial and radial oscillation frequencies . . .	72
5.3	Ramsey interferometry and zero crossing experiment for a thermal cloud after 500 ms of free evolution	73
5.4	Comparison between CGPE simulations and simplified fitting func- tion for a ramsey interferometry sequence	75
5.5	Experimental results for Ramsey interferometry in phase domain and zero crossing experiment using Agilent E8257D synchronized by in- ternal clock	78
5.6	Experimental results for a Ramsey interferometry in phase domain and zero crossing experiment using Agilent E8257D synchronized by OXCO quartz oscillator	80
5.7	Experimental results for a Ramsey interferometry in time domain and zero crossing experiment using QuickSyn Mw generator synchronized by OCXO quartz oscillator	82
5.8	Phase diffusion growth rate for a Ramsey interferometry with thermal atoms using different setup configurations	84
5.9	Ramsey interferometry for long evolution times	85
5.10	Measured preparation pulse uncertainty for a two photon transition .	88
5.11	GPE simulation including losses of Ramsey sequences with variable total atom number	91

5.12	Experimental measurements for a Ramsey interferometry in time domain of a two-component BEC with $\approx 3 \cdot 10^4$ atoms	92
5.13	Experimental measurements for a Ramsey interferometry in time domain of a BEC fitted with a simplified fitting function, equation (5.24)	92
5.14	Experimental measurements for a Ramsey interferometry in time domain and zero crossing obtained using BEC	93
5.15	Zero-crossing experiment with sudden phase jump	94
5.16	Phase evolution under current, degraded state of the system	95
6.1	Rephasing dynamics on a Bloch sphere	108
6.2	Relative phase distribution of two initially independent condensates, semiclassical method	109
6.3	Time evolution of the Coherence factor $\langle \cos(\phi) \rangle$, semiclassical approach	110
6.4	Time evolution of the coherence factor for different coupling strength, exact diagonalization. Adapted from [2].	110
6.5	Simulated axial density distribution for a 2CBEC ground state.	115
6.6	Nonlinear coefficient χ dependence on total atom number	116
7.1	Absorption image and density profiles for independently condensed 2CBEC	122
7.2	Measured and simulated spatial density distributions for a 2CBEC with $N_{tot} = 2 \cdot 10^4$	123
7.3	Engineered rephasing sequence and Bloch sphere representation of the rephasing dynamics	125
7.4	Simulated time evolution of the root mean square width for a 2CBEC.	127
7.5	Time evolution of the normalized density overlap	128
7.7	Coherence measurements using Ramsey interferometry	131
7.8	Coherence factor's time dependence	131
7.9	Relative phase distribution for fast $\pi/2$ pulse rephasing experiment	132

7.10	Coherence factor evolution for different rephasing pulse duration in a fast $\pi/2$ pulse rephasing experiment	133
7.11	Axial density evolution and population losses for a adiabatic 50:50 transfer with Rabi frequency $\Omega_r = 2\pi \cdot 5$ Hz and detuning $\delta_r = -2\pi \cdot 30$ Hz	136
7.12	Axial density evolution and population losses for a adiabatic 50:50 transfer with Rabi frequency $\Omega_r = 2\pi \cdot 5$ Hz and detuning $\delta_r = -2\pi \cdot 40$ Hz	137
7.13	Axial density evolution and population losses for a adiabatic 50:50 transfer with Rabi frequency $\Omega_r = 2\pi \cdot 10$ Hz and detuning $\delta_r = -2\pi \cdot 40$ Hz	138
7.14	Axial density evolution and population losses for a adiabatic 50:50 transfer with Rabi frequency $\Omega_r = 2\pi \cdot 10$ Hz and detuning $\delta_r = -2\pi \cdot 40$ Hz	139
7.15	Time evolution of the Measured and simulated density distributions for an adiabatic 50:50 superposition transfer, $\Omega_r = 2\pi \cdot 10$ Hz, $\delta_r = -2\pi \cdot 40$ Hz	141
7.16	Time evolution of the Measured and simulated spatial density distributions for an adiabatic 50:50 superposition transfer, $\Omega_r = 2\pi \cdot 10$ Hz, $\delta_r = -2\pi \cdot 40$ Hz	142
7.17	Experimentally measured spatial evolution of the optical density . . .	143
7.18	Temporal evolution of the axial oscillations width for an adiabatic 50:50 superposition transfer	143
7.19	Coherence measurements using Ramsey interferometry for an adiabatic 50:50 superposition transfer sequence	145
7.20	Relative phase distribution for an adiabatic 50:50 superposition transfer rephasing experiment	146

7.21 Coherence factor evolution for different rephasing pulse duration in an adaibatic transfer rephasing experiment	147
7.22 Bloch sphere representation for an uneven superposition of atoms undergoing rephasing dynamics	151

List of Tables

3.1	Phase noise for an Agilent E8257D	38
3.2	Phase noise for an FSW-0010 QuickSyn	40
5.1	Summary of the visibility and phase standard deviation measured in the phase diffusion experiment with Agilent E8257D MW synthesizer.	79
5.2	Summary of the visibility and phase standard deviation measured in the phase diffusion experiment with QuickSyn MW synthesizer and OXCO local oscillator.	81

CHAPTER 1

Introduction

The discovery of ^4He superfluidity [3, 4] was for decades the only experimental example of “a new kind of fluid” that shows collective phenomena. The remarkable discovery opened up the challenge to understand very unusual properties this new phase transition displayed, i.e. the absence of the fluid viscosity and the quantization of vortices when the system is forced to rotate. It was quickly realized that such unique features were the first realization of a statistical intrinsic nature the ^4He possesses. Indeed, the seminal work by Satyendra Nath Bose [5] already enlightened, with several years of advance, the existence of a net separation of the behavior a bosonic system should assume at low temperatures with respect to how fermionic systems would react in the very same configuration. The spin statistics was then understood to be the key that allows bosonic particles to undergo *condensation* when the temperature isn't high enough to promote them from the ground state. The work of Fritz London [6] recognized this deep connection between bosons and condensate while the fermionic superfluidity of ^3He needed to be understood through another mechanism that now is known to be a Cooper pair formation. The phase transition temperature towards superfluidity of ^4He , at $T_c = 2.172$ K, also called the λ -point, turned out to be a thousand times higher than the ^3He counterpart due to

a macroscopic occupation of the system's ground state, a condition that cannot be exactly reproduced by a fermion where the Pauli exclusion principle denies multiple occupation of the same state.

These early ideas and great insight in quantum mechanics impressed many when the experimental techniques became as sophisticated enough to cool down a mixture of bosonic gas. Finally, in 1995 the first Bose-Einstein condensation was observed [7–9] with a vapor of ^{87}Rb atoms, confined by magnetic fields and evaporatively cooled. This discovery undoubtedly boosted the research on ultracold gases that were recognized to be the main benchmark towards which address the quest for understanding the quantum mechanical effects on a larger macroscopic scale. Since then indeed many groundbreaking achievement have characterized the field of ultracold gases, like the observation of macroscopic matter wave interference [10], the quantum vortices in a rotating condensate [11], the presence of solitons [12–15], and the observation of the Mott insulator transition [16].

Most of the physics involved was easily modeled by mean-field interactions, due to the dilute and weakly-interacting nature of Bose-Einstein condensates. The Gross-Pitaevskii equation [17, 18] served the purpose since the interactions in a bosonic mixture are not strictly required to obtain condensation, but, they are needed to understand the properties of the condensate. Replacing the Schrödinger equation with the Gross-Pitaevskii had also applications outside the scenario of bosonic mixtures, for example to model superconductors [19] and also describe optical vortices [20]. Still a major challenge has been to proceed beyond the simple scheme of a one-particle picture, to investigate strong interactions and the correlation of condensates. In this context we have seen one great development of experimental techniques to ensure controllability and tunability of ultracold gases, e.g. the reduction of dimensionality to observe the leading role of fluctuation around the mean-field approach, the implementation of optical lattices [21, 22], and the use of Feshbach resonances [23, 24] to tune interactions.

Multi-component BECs experiments have been of particular interest because of the

rich physics their study allows. Cornell's group was the first to achieve condensation of rubidium 87 atoms in the states $|F = 2, m_F = 2\rangle$ and $|F = 1, m_F = -1\rangle$ using sympathetic cooling [25] and, one year later, to produce a two component BEC by transferring atoms from $|F = 1, m_F = -1\rangle$ to $|F = 2, m_F = 1\rangle$ by two-photon microwave and radio frequency radiation [26]. Information on the relative phase of a two component BEC can be obtained using Ramsey interferometry [27, 28] where the first pulse prepares a coherent superposition and the second pulse extracts the phase information as a population imbalance. The coherence of the system is lost over time with corresponding loss of interferometric contrast. Inter-particle interactions are primary contributors to the decoherence of trapped Bose-Einstein condensates [29–31]. It is possible to reduce the dephasing associated with collisional events by tuning the s-wave scattering length to zero using a Feshbach resonance, as was done by Gustavsson et al. [32] or by using noncondensed atoms where the combined contributions coming from greatly reduced densities and the identical spin rotation effect (ISRE) [33] cooperate to increase the coherence time.

So far, these examples had proven the deleterious effects that interactions have on the coherence of a system. However, interactions can have the rather surprising effect of creating a coherent system out of an initially incoherent one. This "rephasing" mechanism was first proposed by Dalla Torre et al. [2], where the authors considered a quantum quench in which two initially independent condensates trapped in a double well were suddenly coupled through uniform tunneling to form an external Josephson junction. They predicted the system would undergo "rephasing" dynamics whose effect was to increase the coherence factor [34]. Furthermore the "rephasing" evolution was expected, in the limit of weak coupling, to follow a universal scaling law, with profound implication in the extension of universal behavior from an equilibrium system, where they are well established, to a system out of thermal equilibrium [35]. Extending the concepts of universality to non equilibrium systems has indeed been the focus of different groups in recent years, especially for closed systems, with some authors finding universal scaling laws at long evolu-

tion times by using the Kibble-Zurek mechanism [36, 37] in systems slowly driven across a second-order phase transition [38, 39] or suddenly quenched [40, 41]. The rephasing dynamics predicted by Dalla Torre et al. differ from those predicted by other authors because they show universality at both short and long times, with relevant implication connecting short-time dynamics, appropriately described by perturbation theory, to long-time, intrinsically non-perturbative dynamics [42].

In this thesis we have extended this model to two-component BECs coupled by an external microwave field, forming an internal Josephson junction, and our simulations are in excellent agreement with the results published by Dalla Torre et al. We have run extensive simulations of the Gross-Pitaevski equation to obtain quantitative result for the evolution of the nonlinear coefficient χ , which in our model takes the place of the tunneling strength and is a crucial parameter for the observation of rephasing dynamics. One major difference between the two models lies in the fact that the rephasing characteristic time depends on the nonlinear interaction strength χ , defined as [43]

$$\chi = \frac{1}{2\hbar}(U_{11} + U_{22} - 2U_{12}) \quad U_{jk} = g_{jk} \int dr^3 |\psi_j|^2 |\psi_k|^2 \quad (1.1)$$

whose strength depends on the value of the interaction strength $g_{jk} = 4\pi\hbar^2 a_{jk}/m$ and on the overlapping of the wave-functions ψ . For ^{87}Rb the scattering lengths have values $a_{11} = 100.40a_0$, $a_{12} = 98.006a_0$ and $a_{22} = 95.47a_0$ [44], all very close together, making $\chi \approx 0$ and therefore suppressing rephasing in a perfectly overlapping two component BEC. The overlapping is therefore crucial in controlling the strength of the nonlinear interactions and can be modified by exploiting the intrinsic immiscible behavior of the wave-functions, a consequence of the fact that the scattering lengths satisfy the immiscibility condition $a_{12}^2 \leq a_{11}a_{22}$ [45, 46]. We have run extensive simulations of the coupled Gross-Pitaevski equation to obtain quantitative results for the evolution of the nonlinear coefficient χ . We have explored three different experimental methods to create initially incoherent and spatially separated condensates, the prerequisites for rephasing to happen: independent evaporation of each component,

fast $\pi/2$ pulse transfer and subsequent collective oscillations and adiabatic transfer to a 50:50 superposition. All these methods will be thoroughly detailed in the chapters to come. We have performed Ramsey measurements of the relative phase distribution with the aim of detecting oscillations of the coherence factor that follow the universal scaling laws obtained theoretically, the signature of rephasing. Finally, the microwave setup used in the experiments has been improved, with a substantial reduction of phase diffusion due to technical noise. The time evolution of the phase stability has been accurately characterized using Ramsey interferometry with thermal atoms and an almost fivefold reduction, from ~ 0.5 rad/s to ~ 0.1 rad/s, measured.

1.1 Thesis structure

This thesis has the following organization:

In the **second chapter** we review the theoretical basis necessary to describe a BEC in a mean-field framework. We outline the derivation of the Gross-Pitaevskii [47] equations for two components coupled by an external field and in the presence of losses using a variational principle, the Thomas-Fermi approximation and we discuss dimensionality reduction methods starting from non-polynomial nonlinear coupled Schrödinger equations which still capture transverse dynamics as variational parameters and ending, with the neglect of the radial terms, in a purely one dimensional model. We briefly present the main ideas employed in the simulations of the coupled Gross-Pitaevskii equations widely used throughout the thesis.

Chapter three provides an overview of the experimental setup. We describe the optical excitation scheme, the magnetic potentials and the radio frequency and microwave systems used to cool, trap and manipulate the atoms. The microwave field intensity for each polarization component is characterized using Rabi oscillations and the magnetic field is calibrated with single photon MW spectroscopy. We have implemented a new imaging system with increased magnification and resolution,

from $\sim 27\mu\text{m}$ to $\sim 10\mu\text{m}$. Finally we have increased the flexibility of the adiabatic passage method for dual-state imaging [48], allowing it to be tuned to any transition frequency by changing the timing of the microwave pulse as well as an external bias field.

In the **fourth chapter** we introduce the Bloch sphere formalism and describe the Ramsey interferometry technique, central to most of our experiments. A theoretical analysis of the major contribution to the phase noise is given, with a distinction between purely quantum (intractable in a mean field approach), mean field (predicted by mean field theory) and technical factors affecting phase noise.

The **fifth chapter** presents the results obtained in a set of Ramsey interference experiments in phase and time domain performed on thermal atoms using a new and improved microwave setup. We provide evidence for the reduction of technical noise to a level below the corresponding quantum noise experienced by a BEC of $\sim 5.5 \cdot 10^4$ atoms. An analysis of other major sources of decoherence is performed and Ramsey interferometry on BECs with small populations is carried out to try to obtain quantum limited clock stability.

Chapter six is an introduction to the physics of bosonic Josephson junctions, both external and internal. The theoretical foundation for the existence of the rephasing effect is illustrated using initially the double well model developed by Dalla Torre et al. [2] and then extended to the two-component case. We present internal Josephson junction simulations that are in agreement with the original model by Dalla Torre. Extensive two component GPE simulations are performed to characterize the behavior of the nonlinear χ coefficient.

In the **seventh chapter** we present the measurements for the rephasing experiment. We use three different approaches to create the right condition for rephasing: independent condensation, fast $\pi/2$ splitting and adiabatic transfer to a 50:50 superposition. Each approach has its pros and cons, which we detail. Ramsey interferometry is used to characterize the relative phase distribution from where the coherence

factor is extracted and compared with the theoretical predictions. The coherence of the system before the application of the rephasing sequence is also studied in a similar way.

Finally, **chapter eight** provides concluding remarks and a brief summary of the results of the thesis.

CHAPTER 2

Two-Component BEC

This chapter provides an introduction to the theory of two-component Bose-Einstein condensates, quantum systems composed of two interacting BECs. Condensates of different elements and condensates of the same element in two different internal states are all examples of two-components BECs. In Swinburne we focus on the creation and manipulation of two-component condensates in different hyperfine states, chiefly $|F = 1, m_F = -1\rangle$ and $|F = 2, m_F = +1\rangle$ in the ground level of ^{87}Rb . Throughout this chapter the coupled Gross-Pitaevski equations (CGPE) are used to provide a mean field description that has been successful in predicting with accuracy many properties of these quantum systems. The hydrodynamic description of a two-component BEC is also briefly introduced and constitutes a useful complement to a CGPE description, particularly when excitations need to be calculated.

2.1 Coupled Gross-Pitaevskii Equations

In the mean-field approximation the state of each BEC component can be described by the condensate's order parameter Ψ_i . The wave functions are normalized as $\int |\Psi_i|^2 d^3\mathbf{r} = N_i$, where N_i is the number of atoms in state $|i\rangle$. The mean-field energy

functional of a two component BEC is [47, 49]

$$E = \int d\mathbf{r} \left[\frac{\hbar^2}{2m} |\nabla\Psi_1|^2 + \frac{\hbar^2}{2m} |\nabla\Psi_2|^2 + V_1(\mathbf{r})\Psi_1 + V_2(\mathbf{r})\Psi_2 + \frac{1}{2}g_{11}|\Psi_1|^4 + \frac{1}{2}g_{22}|\Psi_2|^4 + g_{12}|\Psi_1|^2|\Psi_2|^2 \right] \quad (2.1)$$

with $g_{11} = 4\pi\hbar^2 a_{11}/m$ and $g_{22} = 4\pi\hbar^2 a_{22}/m$ the coupling constants expressed in terms of the s-wave scattering lengths for collisions between atoms occupying the same state, while $g_{12} = 4\pi\hbar^2 a_{12}/m$ is determined by the scattering length of atoms occupying different states. The first four terms in eq. (2.1) correspond to the kinetic and potential energy in the external potential V_i and the remaining terms takes into account the interaction between condensed atoms, well described in the low energy limit by the s-wave scattering length a_{jk} . It is possible to derive from eq. (2.1) the coupled Gross-Pitaevskii equations (CGPE) for the two-component BEC from the variational principle $i\hbar\partial\Psi_i/\partial t = \delta E/\delta\Psi_i^*$:

$$\begin{aligned} i\hbar\frac{\partial}{\partial t}\Psi_1 &= \left(-\frac{\hbar^2\nabla^2}{2m} + V_1(\mathbf{r}) + g_{11}|\Psi_1|^2 + g_{12}|\Psi_2|^2 \right)\Psi_1 \\ i\hbar\frac{\partial}{\partial t}\Psi_2 &= \left(-\frac{\hbar^2\nabla^2}{2m} + V_2(\mathbf{r}) + g_{22}|\Psi_2|^2 + g_{12}|\Psi_1|^2 \right)\Psi_2 \end{aligned} \quad (2.2)$$

Equations (2.2) do not take into account losses or electromagnetic coupling terms. If we couple two components with the electromagnetic radiation $\hbar\Omega e^{i\omega t}$, the inclusion of such terms in the rotating-wave approximation leads to [50]

$$\begin{aligned} i\hbar\frac{\partial}{\partial t}\Psi_1 &= \left(-\frac{\hbar^2\nabla^2}{2m} + V_1(\mathbf{r}) + g_{11}|\Psi_1|^2 + g_{12}|\Psi_2|^2 - i\hbar\Gamma_1 + \frac{\hbar\delta}{2} \right)\Psi_1 + \frac{\hbar\Omega}{2}\Psi_2 \\ i\hbar\frac{\partial}{\partial t}\Psi_2 &= \left(-\frac{\hbar^2\nabla^2}{2m} + V_2(\mathbf{r}) + g_{22}|\Psi_2|^2 + g_{12}|\Psi_1|^2 - i\hbar\Gamma_2 - \frac{\hbar\delta}{2} \right)\Psi_2 + \frac{\hbar\Omega}{2}\Psi_1 \end{aligned} \quad (2.3)$$

where $\delta = \omega - \omega_1$ is the detuning, Ω is the resonant Rabi frequency, $\Gamma_1 = \frac{1}{2}(\gamma_{111}|\Psi_1|^4 + \gamma_{12}|\Psi_2|^2)$, $\Gamma_2 = \frac{1}{2}(\gamma_{12}|\Psi_1|^2 + \gamma_{22}|\Psi_2|^2)$ are the loss rate and γ_{12} , γ_{22} , γ_{111} are loss coefficients for two and three-body losses [51]. For the case of two-body losses, the dominant process is spin-exchange interactions. However spin-exchange interactions

are suppressed for the $|1\rangle = |F = 1, m_F = -1\rangle$ state used in our experiment due to the conservation of total m_F . In fact there is no state with $m_F < -1$ in the $F = 1$ manifold and the transfer of one of the atoms in the $F = 2$ manifold is energetically forbidden due to the very low temperature. Two body losses are therefore only relevant for the other state used in our experiment, $|2\rangle = |F = 2, m_F = 1\rangle$, where collisions of the type $|2, 1\rangle + |2, 1\rangle \Rightarrow |2, 0\rangle + |2, 2\rangle$ leads to the loss of particle $|2, 0\rangle$ from the trap. In a superposition of two states collisions of the type $|1\rangle + |2\rangle \Rightarrow |2, 0\rangle + |1, 0\rangle$ are also possible and leads to two-body losses with loss coefficient γ_{12} . The experimentally measured values [52] for $\gamma_{22} = 8.1 \cdot 10^{-14} \text{ cm}^3\text{s}^{-1}$ and for $\gamma_{12} = 1.51(19) \cdot 10^{-14} \text{ cm}^3\text{s}^{-1}$.

Momentum conservation prevents molecule formation in two body collisions, but in three-body collisions two atoms can form a molecule while the third carries away momentum. When a molecule is formed the energy released is usually enough to expel both the molecule and the atom from the trap. Both states experience three body losses, but this loss process is negligible when compared to two-body losses for atoms in state $|2\rangle$. The experimentally measured value [44] for the three body coefficient is $\gamma_{111} = 5.8 \cdot 10^{-30} \text{ cm}^6\text{s}^{-1}$.

It is worth recalling the conditions of applicability for the CGPE of equations (2.2) and (2.3); the total number of atoms N should be large, both to justify the concept of Bose-Einstein condensation and to ensure the orthogonality of the many-body wave functions $\Phi_{i,a}$ and $\Phi_{i,b}$, defined, in the Hartree-Fock approximation, as

$$\Phi_{i,a}(\mathbf{r}_1, \mathbf{r}_2, \dots, \mathbf{r}_N) = \left(\frac{1}{\sqrt{N}} \Psi_{i,a}(\mathbf{r}_1) \right) \left(\frac{1}{\sqrt{N}} \Psi_{i,a}(\mathbf{r}_2) \right) \dots \left(\frac{1}{\sqrt{N}} \Psi_{i,a}(\mathbf{r}_N) \right) \quad (2.4)$$

In fact, if $\Psi_{i,a}$ and $\Psi_{i,b}$ are two solutions of the CGPE corresponding to two different values of the chemical potentials μ_a and μ_b for component i , they are not, in general, orthogonal [47], but the corresponding many-body wave functions become orthogonal in the thermodynamic limit since $(\Phi_{i,a}, \Phi_{i,b}) = (N^{-1} \int d\mathbf{r} \Psi_{i,a}^* \Psi_{i,b})^N$ tends to zero when $N \rightarrow \infty$ because $\int d\mathbf{r} \Psi_{i,a}^* \Psi_{i,b} \leq N$. The diluteness condition $|a_{ij}| \ll n^{-\frac{1}{3}}$ must also be satisfied and the temperature should be low enough to allow us to

ignore the quantum and thermal depletion of the condensate, respectively. Finally the CGPE can only be used to investigate phenomena that take place over distances much larger than the scattering length a_{ij} .

2.1.1 Hydrodynamic equations

It is possible, under general conditions, to use, instead of the CGPE equations (2.2), an exactly equivalent set of equations for the density $n = |\Psi_i|^2$ and the condensate phase θ_i . If we multiply equations (2.2) by Ψ_i^* and then subtract the complex conjugate of the resulting equations we obtain [47, 49]

$$\frac{\partial |\Psi_i|^2}{\partial t} + \nabla \cdot \left[\frac{\hbar}{2mi} (\Psi_i^* \nabla \Psi_i - \Psi_i \nabla \Psi_i^*) \right] = 0 \quad (2.5)$$

which has the form of a continuity equation for the particle density. With the introduction of the velocity of the condensate, defined as

$$\mathbf{v}_i = \frac{\hbar}{2mi} \frac{(\Psi_i^* \nabla \Psi_i - \Psi_i \nabla \Psi_i^*)}{|\Psi_i|^2}. \quad (2.6)$$

Equation (2.6) can be rewritten in the form

$$\frac{\partial n_i}{\partial t} + \nabla \cdot (n_i \mathbf{v}_i) = 0. \quad (2.7)$$

We can further simplify equation (2.6) by expressing Ψ_i in terms of amplitude and phase $\Psi_i = \sqrt{N_i} e^{i\theta_i}$

$$\mathbf{v}_i = \frac{\hbar}{m} \nabla \theta_i \quad (2.8)$$

and finally obtain the equation of motion for the velocity

$$m \frac{\partial \mathbf{v}_i}{\partial t} = -\nabla (\tilde{\mu}_i + \frac{1}{2} m v_i^2) \quad (2.9)$$

where

$$\tilde{\mu} = V(\mathbf{r}) + n_1 g_{1i} + n_2 g_{i2} - \frac{\hbar^2}{2m\sqrt{n_i}} \nabla^2 \sqrt{n_i} \quad (2.10)$$

Equation (2.9) can be derived by taking the gradient of

$$-\hbar \frac{\partial \phi}{\partial t} = -\frac{\hbar^2}{2m\sqrt{n_i}} \nabla^2 \sqrt{n_i} + \frac{1}{2} m v_i^2 + V(\mathbf{r}) + n_1 g_{1i} + n_2 g_{i2} \quad (2.11)$$

Equation (2.11) explicitly gives the time evolution of the phase and can be obtained after inserting the order parameter $\Psi_i = \sqrt{N_i}e^{i\theta_i}$ into the CGPE and separating real and imaginary parts. The quantity $n_1g_{1i} + n_2g_{i2}$ in equation (2.10) is the chemical potential for a 2CBEC and, at zero temperature, can be related to the pressure through the Gibbs-Duhem relation $dp = nd\mu$, giving $p = -\partial E/\partial V = n_1^2g_{1i}/2 + n_2^2g_{i2}/2$. Using the expression for the pressure, equation (2.9) can be cast in the form

$$\frac{\partial \mathbf{v}_i}{\partial t} = -\frac{1}{mn_i}\nabla p - \frac{1}{m}\nabla V(\mathbf{r}) + \frac{1}{m}\nabla \frac{\hbar^2}{2m\sqrt{n_i}}\nabla^2\sqrt{n_i} - \nabla \frac{v_i^2}{2} \quad (2.12)$$

Equations (2.7) and (2.12) resemble very closely the hydrodynamic equations for a perfect fluid, with equation (2.7) having exactly the same form, while equation (2.12) differing slightly from the corresponding Euler equation for a perfect fluid

$$\frac{\partial \mathbf{v}_i}{\partial t} = -\frac{1}{mn_i}\nabla p - \frac{1}{m}\nabla V(\mathbf{r}) + \mathbf{v}_i \times (\nabla \times \mathbf{v}_i) - \nabla \frac{v_i^2}{2} \quad (2.13)$$

the differences being the irrotationality of equation (2.12) in the absence of vortices and the quantum pressure term $\frac{1}{m}\nabla \frac{\hbar^2}{2m\sqrt{n_i}}\nabla^2\sqrt{n_i}$. The quantum pressure term describes forces due to spatial variations in the magnitude of the wave function and dominates the pressure term on a length scale of the order of the coherence length $\xi \sim \hbar/(mn_i g_{ii})$. The hydrodynamic equations are particularly suited to investigate excitations and vortex behavior in BEC.

2.1.2 Ground state and Thomas-Fermi approximation

The ground state of a single BEC satisfies the time-independent GPE equation [53, 54]

$$\mu\Psi = \left(-\frac{\hbar^2\nabla^2}{2m} + V(\mathbf{r}) + g|\Psi_0|^2 \right)\Psi \quad (2.14)$$

where $g = 4\pi\hbar^2 a/m$ is the coupling constant and a is the scattering length. Equation (2.14) can be derived from the minimization of the energy functional

$$E = \int d\mathbf{r} \left[\frac{\hbar^2}{2m}|\nabla\Psi|^2 + V(\mathbf{r})|\Psi|^2 + \frac{1}{2}g|\Psi|^4 \right] \quad (2.15)$$

with respect to Ψ^* with the constraint that the total number of atoms N is constant. Throughout this thesis, the ground state is computed using the imaginary time propagation method [55–57]. This method uses a time-dependent GPE

$$i\hbar \frac{\partial}{\partial t} \Psi = \left(-\frac{\hbar^2 \nabla^2}{2m} + V(\mathbf{r}) + g|\Psi|^2 \right) \Psi \quad (2.16)$$

and makes a Wick rotation to imaginary time $t \rightarrow \tau = it$. A trial function $\Psi(\mathbf{r}, \tau_0) = \Psi_0(\mathbf{r})$ is then propagated and normalized for every time interval $[\tau_n, \tau_{n+1}]$. Every step decreases the energy functional eq. (2.15) and in the limit $\tau \rightarrow \infty$ the ground state is reached. Practically the computation ends when the energy functional drops below a predefined value. The correct choice of the trial function $\Psi_0(\mathbf{r})$ is very important to ensure the convergence. In the limit of small particle number or weak interaction we can neglect the nonlinear term in the GPE eq. (2.14). The ground state, when the potential $V(x, y, z)$ is an anisotropic harmonic-oscillator given by

$$V(x, y, z) = \frac{1}{2}m(\omega_1^2 x^2 + \omega_2^2 y^2 + \omega_3^2 z^2) \quad (2.17)$$

is a Gaussian function of the form

$$\Psi_G = \frac{1}{\pi^{3/4}(a_1 a_2 a_3)^{1/2}} e^{x^2/2a_1^2} e^{y^2/2a_2^2} e^{z^2/2a_3^2}. \quad (2.18)$$

When the particle number is large and the interactions repulsive, a trial wave function can be obtained by neglecting the kinetic energy term in equation (2.14), or equivalently the quantum pressure term in equation (2.12). This is the well known Thomas-Fermi approximation and the ground state takes the simple form

$$\Psi_{TF} = \begin{cases} \sqrt{\frac{\mu_{TF} - V(x, y, z)}{g}} & \text{if } V(x, y, z) < \mu_{TF} \\ 0 & \text{if } V(x, y, z) \geq \mu_{TF} \end{cases} \quad (2.19)$$

It is possible to simulate the ground state for a 2CBEC using the CGPE (2.2), but this approach does not reproduce the conditions usually found in the experiment. The condensate is normally prepared all in state $|1\rangle$ and then half of it is transferred in state $|2\rangle$ through the application of a 2-photon MW+Rf pulse ($\pi/2$ pulse). This

leaves the 2CBEC in a non-stationary state that exhibits collective oscillations in the form of breathing modes [58, 59].

It is worth mentioning that the imaginary time propagation method can produce accurate estimates of the first excited state as well, provided that the initial trial wave function has an odd symmetry [56].

2.1.3 Reduction to lower dimensions

In our experiment the condensate is trapped in an external potential with cylindrical symmetry. The confinement is tighter in the radial direction compared to the axial ($\omega_r \sim 10\omega_z$). This geometry is commonly known as a "cigar shape" trap. Due to the high energy cost ($\sim \hbar\omega_r$ compared to $\sim \hbar\omega_z$) of producing an excitation along the radial direction, we can assume the dynamics happen along the axial direction only. This allows us to describe the 3D 2CBEC with an effective 1D treatment. The 3D 2CGPE equation can be reduced to a 1D 2CGPE by minimizing the action [60, 61] with respect to Ψ_i^*

$$A = \int \mathcal{L}_1 + \mathcal{L}_2 - U_{12}|\Psi_1|^2|\Psi_2|^2 d\mathbf{r} dt \quad (2.20)$$

where

$$\mathcal{L}_i = i\frac{\hbar}{2} \left(\Psi_i^* \frac{\partial \Psi_i}{\partial t} - \Psi_i \frac{\partial \Psi_i^*}{\partial t} - \frac{\hbar}{2m} |\nabla \Psi_i|^2 - V|\Psi_i|^2 - \frac{1}{2} U_{ii} |\Psi_i|^4 \right) \quad (2.21)$$

given the trial wave function

$$\Psi_i = \phi_i(r, z, t) f_i(z, t) = \frac{e^{r^2/(2a_{ir}^2)}}{\sqrt{\pi a_{ir}}} f_i(z, t) \quad (2.22)$$

with $a_{ir} = \sqrt{\hbar/(m_i\omega_{ir})}$ the characteristic length of the harmonic oscillator and ϕ_i a Gaussian function that correctly models the condensate in the weak interaction limit and is acceptable in the strong coupling limit (a rigorous mathematical treatment of the strong coupling limit can be found in [60, 62]).

Assuming ϕ_i varies slowly along the axial direction

$$\nabla^2 \phi_i \approx \left(\frac{\partial^2}{\partial x^2} + \frac{\partial^2}{\partial y^2} \right) \phi_i \quad (2.23)$$

we replace the trial wave function in equation (2.20) and after integrating along x and y we are left with the Euler-Lagrange equation for the two variational functions $f_1(z, t)$ and $f_2(z, t)$

$$i\hbar \frac{\partial}{\partial t} f_1 = \left[-\frac{\hbar^2}{2m} \frac{\partial^2}{\partial z^2} + \frac{m\omega_{1z}^2 z^2}{2} + \frac{g_1}{2\pi a_{1r}^2} |f_1|^2 + \hbar\omega_{1r} + \frac{g_{12}}{\pi(a_{1r}^2 + a_{2r}^2)} |f_2|^2 \right] f_1 \quad (2.24)$$

$$i\hbar \frac{\partial}{\partial t} f_2 = \left[-\frac{\hbar^2}{2m} \frac{\partial^2}{\partial z^2} + \frac{m\omega_{2z}^2 z^2}{2} + \frac{g_2}{2\pi a_{2r}^2} |f_2|^2 + \hbar\omega_{2r} + \frac{g_{12}}{\pi(a_{1r}^2 + a_{2r}^2)} |f_1|^2 \right] f_2 \quad (2.25)$$

Equations (2.24) and (2.25) are the 1D equivalent of the 3D CGPE and can be further simplified by neglecting the constant $\hbar\omega_{ir}$ since it does not affect the dynamics. Equations (2.24) and (2.25) are valid in the weakly interacting regime, when $a_{ii}|f_i|^2 \ll 1$. For the strongly interacting regime we cannot use the harmonic oscillator characteristic length as the width of the Gaussian trial function, but we have to introduce an additional variational parameter $\sigma_i(z, t)$ and solve two additional Euler-Lagrange equations that will eventually give us explicit expressions for σ_i in terms of f_i (details in [60]).

The 1DCGPE can be obtained from equations (2.2) in a general way by neglecting the radial terms and by replacing the nonlinear coefficient with

$$g_{ij}^{1D} = g_{ij} \int_0^\infty |\Psi_i(r, z, t)|^2 |\Psi_j(r, z, t)|^2 dr \quad (2.26)$$

where Ψ_i and Ψ_j are suitable trial function. It is important to remember the different conditions in which a 1D BEC can be found. In the limit $a_{ii}|f_i|^2 \gg 1$ the system is geometrically one dimensional but the BEC locally retains its three dimensional features; if $a_{ii}|f_i|^2 \ll 1$ the condensate enters the 1D regime. This regime can still be treated using a mean field theory if $|f_i|^2 a_{ir}^2 / a_{ii} \gg 1$, otherwise one should use Lieb and Liniger theory [63], which introduces beyond mean field effects. In the limit of very low density, when $a_{ir}^2 |f_i|^2 / a_{ii} \ll 1$, we enter the Tonks-Girardeau regime [64, 65]

where particles behave like impenetrable objects and an interacting Bose gas can be described as a Fermi gas.

2.1.4 Simulation of the non-equilibrium dynamics of 2CBEC

The first step to efficiently solve equations (2.3) is to cast them in dimensionless form. By introducing the harmonic oscillator length

$$\omega_m = \min(\omega_x, \omega_y, \omega_z), \quad a_0 = \sqrt{\frac{\hbar}{m\omega_m}} \quad (2.27)$$

and by making the following change of variables

$$\begin{aligned} \mathbf{r} &\rightarrow \mathbf{r}' = \frac{\mathbf{r}}{a_0}, & t &\rightarrow t' = \omega_m t, \\ E &\rightarrow E' = \frac{E}{\hbar\omega_m}, & \Psi &\rightarrow \Psi' = a_0^{3/2} \Psi \end{aligned} \quad (2.28)$$

we obtain

$$\begin{aligned} i \frac{\partial}{\partial t} \Psi'_1 &= \left(-\frac{\nabla^2}{2} + V'_1(\mathbf{r}) + g'_{11} |\Psi'_1|^2 + g'_{12} |\Psi'_2|^2 - i\Gamma'_1 + \frac{\delta'}{2} \right) \Psi'_1 + \frac{\Omega'}{2} \Psi'_2 \\ i \frac{\partial}{\partial t} \Psi'_2 &= \left(-\frac{\nabla^2}{2} + V'_2(\mathbf{r}) + g'_{22} |\Psi'_2|^2 + g'_{12} |\Psi'_1|^2 - i\Gamma'_1 - \frac{\delta'}{2} \right) \Psi'_2 + \frac{\Omega'}{2} \Psi'_1 \end{aligned} \quad (2.29)$$

with

$$\begin{aligned} V'_1 = V'_2 &= \frac{1}{2} (\lambda_x^2 x^2 + \lambda_y^2 y^2 + \lambda_z^2 z^2), & \lambda_{x,y,z} &= \frac{\omega_{x,y,z}}{\omega_m}, & g'_{ij} &= \frac{4\pi a_{ij}}{a_0}, \\ \gamma'_{111} &= \frac{\gamma_{111}}{\omega_m a_0^6}, & \gamma'_{ij} &= \frac{\gamma_{ij}}{\omega_m a_0^3}, & \Omega' &= \frac{\Omega}{\omega_m}, & \delta' &= \frac{\delta}{\omega_m} \end{aligned} \quad (2.30)$$

The solution to Equations (2.29) has the approximate form [66, 67]

$$\Psi_i^{(n+1)} \approx e^{-i\Delta t \hat{A}} e^{-i\Delta t \hat{B}} \Psi_i^{(0)}(\mathbf{r}) \quad (2.31)$$

and is found in two steps with a time splitting spectral scheme (TSSP). The first step consist of finding a solution for the differential operator \hat{A}

$$\left\{ \begin{aligned} i \frac{\partial}{\partial t} \Psi_i^{(1)}(t, \mathbf{r}) &= -\frac{\nabla^2}{2} \Psi_i^{(1)}(t, \mathbf{r}) \quad \text{with} \quad n\Delta < t \leq (n+1)\Delta t \\ \Psi_i^{(1)}(n\Delta t, \mathbf{r}) &= \Psi_i^{(0)}(\mathbf{r}) \end{aligned} \right. \quad (2.32)$$

by Fourier transforming $\mathcal{F}(\nabla^2\Psi_i^{(1)})$, solving the resulting algebraic equation and then inverse Fourier transforming the result. The second step solves the remaining nonlinear operator \hat{B}

$$\left\{ \begin{array}{l} i\frac{\partial}{\partial t}\Psi_i^{(2)} = \left(V_1'(\mathbf{r}) + g'_{11}|\Psi_i^{(2)}|^2 + g'_{12}|\Psi_j^{(2)}|^2 - i\Gamma_1' + \frac{\delta'}{2} \right) \Psi_i^{(2)} + \frac{\Omega'}{2}\Psi_i^{(2)} \\ \Psi_i^{(2)}(n\Delta t, \mathbf{r}) = \Psi_i^{(1)}((n+1)\Delta t, \mathbf{r}) \quad \text{with} \quad n\Delta < t \leq (n+1)\Delta t \end{array} \right. \quad (2.33)$$

with an exact integration of equation (2.33). With the splitting scheme of equation (2.31), called a Lie split, the approximation is first order in time and spectral in space. This means we have to set a relatively small time step Δt for precise results, while the spatial grid can be coarse. The method can be improved by using a different splitting scheme, called a Strang split [68], that approximates the solution with

$$\Psi_i^{(n+1)} \approx e^{-i(\Delta t/2)\hat{A}} e^{-i\Delta t\hat{B}} e^{-i(\Delta t/2)\hat{A}} \Psi_i^{(0)}(\mathbf{r}) \quad (2.34)$$

and improves the scheme to second order in time.

CHAPTER 3

Experimental Apparatus

In this chapter we provide a comprehensive description of the setup and the methods used in the experiments. The system is designed to prepare a ^{87}Rb Bose-Einstein condensate (BEC) in the stretched state $|F = 1, m = -1\rangle$ of the ground state manifold. The ^{87}Rb atoms are trapped in an ultra high vacuum (UHV) chamber using a magnetic field produced by multiple sets of coil surrounding the chamber and an "atom chip" placed inside the chamber, compatible with the requirement for UHV. The atoms are cooled to temperatures in the range of several tens of μK by the combined application of Doppler-limited optical molasses and sub-Doppler polarization gradient cooling (PGC). The final cooling needed to reach the critical temperature for BEC formation is achieved using the radio frequency evaporation technique. Once the BEC phase has been reached, we manipulate the condensed atoms by applying radio-frequency (RF) and micro-wave (MW) fields. The application of these fields leads to coupling between the different hyperfine sub levels and allows us to perform the two component BEC experiments (2CBEC) described in the following chapters. Finally we extract information about the populations of two states using a dual state absorption imaging technique combining adiabatic population transfer with the Stern-Gerlach separation.

3.1 Magnetic trapping

Neutral atoms can be trapped using the interaction between their permanent magnetic-dipole moment and a static magnetic field, by inducing an electric-dipole moment through the application of an inhomogeneous laser field, or using time varying fields (e.g. TOP traps). Compared to the trapping of ions, who have a charge on which an electromagnetic field can exert considerable Coulomb or Lorentz force, the forces that can be applied on neutral atoms are rather weak, hence it is necessary to laser cool them. The technique and the setup for our laser cooling system will be the topic of the next section. In this section we focus our attention on magnetic trapping, the interaction of a static magnetic field with a neutral atom, the types of magnetic traps used in the experiment and the equipment employed to create them.

3.1.1 Interaction of an atom with a magnetic field

We start by considering the Hamiltonian describing the hyperfine energy levels of an atom in a static magnetic field B . The total Hamiltonian H_{tot} is the sum of the hyperfine Hamiltonian H_{hfs} and the Hamiltonian describing the interaction with the magnetic field H_B :

$$H_{tot} = H_{hfs} + H_B \quad (3.1)$$

with [69,70]

$$H_{hfs} = A_{hfs} \mathbf{I} \cdot \mathbf{J} + \overbrace{B_{hfs} \frac{3(\mathbf{I} \cdot \mathbf{J})^2 + \frac{3}{2} \mathbf{I} \cdot \mathbf{J} - I(I+1)J(J+1)}{2I(2I-1)J(2J-1)}}^{=0 \text{ for levels with } J=1/2, \text{ as in } ^{87}\text{Rb ground state}} \quad (3.2)$$

$$H_B = \frac{\mu_B}{\hbar} (g_J J_z + g_I I_z) B_z \quad (3.3)$$

where A_{hfs} is the magnetic dipole constant, B_{hfs} is the electric quadrupole constant, \mathbf{I} is the total nuclear angular momentum, \mathbf{J} is the total electron angular momentum,

μ_B is the Bohr magneton, $g_{j,i}$ are respectively the electron and nuclear g -factors. The static magnetic field \mathbf{B} is taken to be along the z axis and the quantization axis is chosen in the same direction. For weak magnetic field ($B < 1000$ G, see figure 3.1), H_B is a perturbation of H_{hfs} , $F = J + I$ is a good quantum number, the state of the atom can be expressed in the $|F, m_F\rangle$ base and the energy levels split according to [70]:

$$\Delta E_{|F, m_F\rangle} = \mu_B g_F m_F B_z \quad (3.4)$$

where g_F is given by [71]:

$$g_F = g_J \frac{F(F+1) - I(I+1) + J(J+1)}{2F(F+1)} + g_I \frac{F(F+1) + I(I+1) - J(J+1)}{2F(F+1)} \quad (3.5)$$

For strong magnetic fields H_{hfs} becomes a perturbation of H_B , J and I are good quantum numbers, the state can be expressed in the $|J, m_J I, m_I\rangle$ base and the energies are given by:

$$E_{|J, m_J I, m_I\rangle} = A_{hfs} m_J m_I + \mu_B (g_J m_J + g_I m_I) B_z \quad (3.6)$$

For intermediate fields, perturbation theory cannot be applied and the Hamiltonian $H_{tot} = H_{hfs} + H_B$ needs to be diagonalized numerically. However, for states with $J = 1/2$, as is the case of the ground state of alkali metals, we can apply the Breit-Rabi formula [70, 72] (figure 3.1), that provides an analytical solution to the problem:

$$E_{|J=1/2, m_J I, m_I\rangle} = -\frac{\Delta E_{hfs}}{2(2I+1)} + g_I \mu_B m B \pm \frac{\Delta E_{hfs}}{2} \left(1 + \frac{4mx}{2I+1} + x^2 \right)^{1/2} \quad (3.7)$$

where $x = (g_J - g_I) \mu_B B / \Delta E_{hfs}$ and $m = m_I \pm 1/2$ depending on the sign chosen in equation (3.7)

As can be seen from equation (3.4), the energy of a state depends on the magnetic field. Atoms in an inhomogeneous magnetic field will experience a spatially-varying

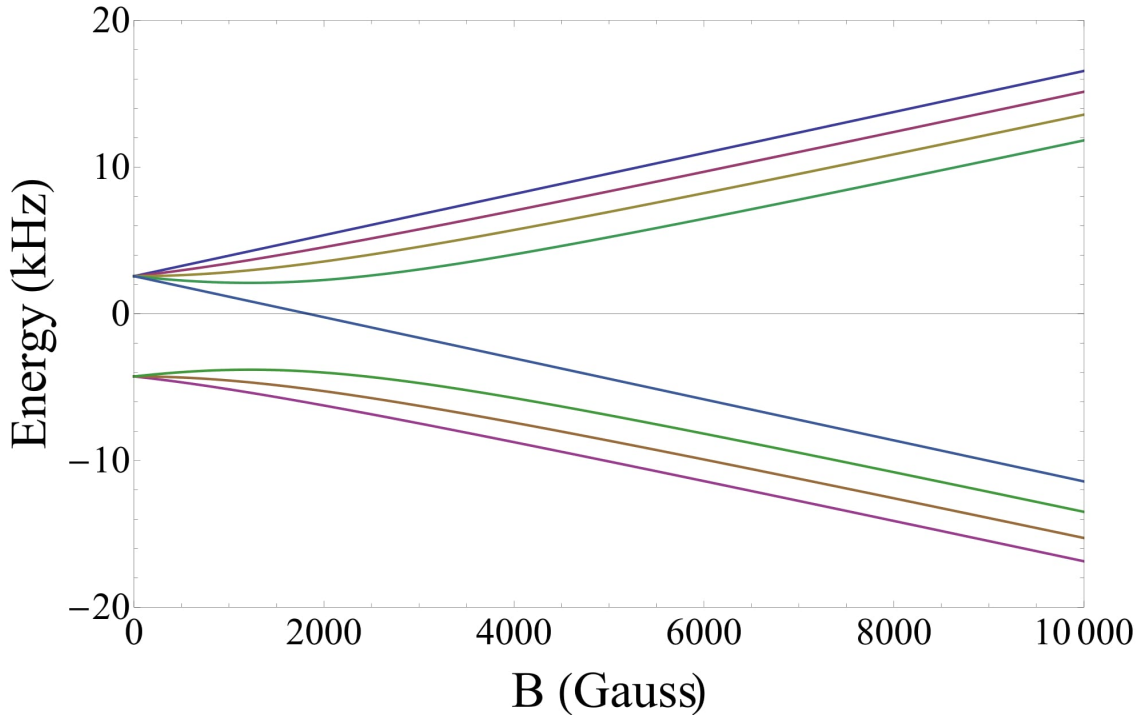


Figure 3.1: Zeeman split of the hyperfine levels $F=2$ and $F=1$ in ^{87}Rb calculated using the Breit-Rabi formula, equation 3.7

potential proportional to $g_F m_F$. If $g_F m_F > 0$, the atom will experience a force toward the regions of lower magnetic field and the corresponding states are called *low-field seekers*. States with $g_F m_F < 0$ on the other hand will experience a force toward the region of high magnetic field and are therefore called *high-field seekers*. In regions where there are no electric currents it is impossible to have a local maximum of the magnetic field and therefore the only states relevant for magnetic trapping are *low-field seeking* states.

3.1.2 Quadrupole coils

We use a pair of identical coaxial coils carrying equal currents in opposite directions to create a quadrupole magnetic field. In our experiments the quadrupole field is used in conjunction with laser beams during the initial cooling stages (MOT and

CMOT, see section 3.2.1). The coils used have a radius $R = 7.5$ cm, with $n = 400$ turns each. In order to produce a quadrupole field which is nearly uniform around the minimum of the field, the coils should be in an *anti-Helmholtz* configuration, which means they should satisfy the following conditions:

the current in each coil is *equal* in magnitude and *opposite* in direction;

the distance d between the two coils is $d = \sqrt{3}R$.

The condition on the current is satisfied by wiring the coils in series and driving them with a single power supply. The usual values of the current range between 9.0 A and 9.2 A. The condition on the distance is not satisfied due to the constraint imposed by the size of the vacuum chamber. The separation between the coils is currently $d \approx 4R$ and cannot be reduced. Increasing the radius of the coils will lead to an increase in inductance and resistance, with a consequent increase in switching time and heating, both undesirable. Magnetic field simulations show only a small departure from the ideal quadrupole potential, both in terms of linearity and gradient strength for the present configuration. The current is controlled by a switching circuit based around a high-power bipolar-junction transistor (BJT) and an OP-amp feedback loop (figure 3.2). There are independent switches for every element creating a magnetic field, with the exception of the Z and U-Wire traps that share the same switch [73]. The switching speed differs by the nature of the load, with mostly resistive loads, Z and U wire, being the fastest (few μs) and highly inductive loads, quadrupole coils and large bias field coils, being the slowest (hundreds of μs). Additionally, with an inductive load, is very important to set the right parameters for the feedback loop, in order to damp the inevitable LCR resonances (usually in the range of tens of kHz). The stability in time of the magnetic field produced is also very important and we infer it by measuring the stability of the voltage across a sense resistor. For the fields used during evaporative cooling, when trap stability is paramount, we use water-cooled monitor resistors built to strict tolerances to minimize fluctuations in the readings due to variations

in the resistor itself. The voltage is stable in the mV range over a 20 seconds period. The magnetic field generated by a single coil is [74], using cylindrical coordinates, with the z-axis coaxial with the center of the coils:

$$\mathbf{B}_z = \frac{\mu_0 I}{2\pi} \frac{1}{\sqrt{(R+\rho)^2 + (z-A)^2}} \left(\frac{R^2 - \rho^2 - (z-A)^2}{(R-\rho)^2 + (z-A)^2} E(k^2) + K(k^2) \right) \quad (3.8)$$

$$\mathbf{B}_\rho = \frac{\mu_0 I}{2\pi\rho} \frac{z-A}{\sqrt{(R+\rho)^2 + (z-A)^2}} \left(\frac{R^2 + \rho^2 + (z-A)^2}{(R-\rho)^2 + (z-A)^2} E(k^2) - K(k^2) \right) \quad (3.9)$$

$$k^2 = \frac{4R\rho}{(R+\rho)^2 + (z-A)^2} \quad |\mathbf{B}| = \sqrt{\mathbf{B}_z^2 + \mathbf{B}_\rho^2} \quad (3.10)$$

where $E(k^2)$ and $K(k^2)$ are elliptic integrals, A is the distance along the z-axis, $\rho = \sqrt{x^2 + y^2}$ is the distance on a plane perpendicular to the z-axis, R is the coil radius and $\mu_0 = 4\pi \cdot 10^{-7}$ T·m/A is the vacuum permeability. The fields of a pair of coils in anti-Helmholtz configuration can be calculated as a superposition of two such field with opposite currents I. From eqs. (3.8) and (3.9) it is clear that such a configuration has only one point where the field is zero, and this point lies on the z-axis halfway between the coils. The magnetic field around the minimum has the form:

$$\mathbf{B} = B'_x x + B'_y y + B'_z z \quad (3.11)$$

The potential generated is proportional to the field gradient and varies linearly, providing a confining force $\vec{F} = \vec{\nabla}(\mu \cdot \vec{B})$ in all three directions. However, due to the Maxwell's equations requiring that $B'_x + B'_y + B'_z = 0$, the force is neither harmonic nor central. The gradient of the magnetic field for the usual experimental condition $I = 9.2$ A is ≈ 4.5 G/cm in the radial direction and ≈ 9.5 G/cm in the axial direction.

It is a well known fact that the quadrupole field cannot be used to achieve BEC due to Majorana spin-flip losses. This loss mechanism arises because atoms confined in a quadrupole trap explore, as they move, regions where the magnetic field changes in magnitude and direction. For the atoms to remain trapped, as we have seen in 3.1.1, they must remain in a weak-field seeking state. The atoms will remain in a specific magnetic sub level as long as the Larmor frequency $\omega_L = g_F m_f \mu_B B / \hbar$,

describing the precession of the magnetic moment around the magnetic field is fast compared to the field variations. The assumption that the spin follows adiabatically the local direction of the magnetic field is valid if

$$\mathbf{v} \cdot \nabla \mathbf{B} \ll \omega_L \quad (3.12)$$

where \mathbf{v} is the speed of a particle and ω_L is the Larmor frequency. In regions of the trap where the magnetic field is very weak, this condition is not satisfied, and atoms will be ejected. For hot enough atoms, however, the losses will be small, because the size of the region where Majorana spin-flip is relevant has size $\propto \sqrt{2\hbar v / \pi \mu B'}$, with v being the speed of the atoms, which is much smaller than the size of the cloud. When the temperature drops, v decreases, decreasing the size of the "hole", but the size of the cloud decreases even faster, giving a T^{-2} dependence of the loss rate with the temperature [75]. For this reason condensation is achieved in a different field configuration, a configuration with non-zero magnetic field everywhere, achievable in a Ioffe-Pritchard trap.

3.1.3 Ioffe-Pritchard trap

One way to overcome the Majorana spin-flip losses is to confine atoms in a trap with a non-zero minimum. The most common realization of such a trap is the Ioffe-Pritchard (IP) [74–76]. The trapping field has the form:

$$\mathbf{B} = B_b \begin{pmatrix} 1 \\ 0 \\ 0 \end{pmatrix} + B' \begin{pmatrix} 0 \\ -y \\ z \end{pmatrix} + \frac{B''}{2} \begin{pmatrix} x^2 + (y^2 + z^2)/2 \\ -xy \\ -xz \end{pmatrix} \quad (3.13)$$

where B_b is a bias field. The modulus of the field, obtained by expanding to second order near the minimum, which we make to coincide with the origin of our reference frame, is:

$$|\mathbf{B}| \approx B_b + \frac{B''}{2} x^2 + \frac{1}{2} \left(\frac{B'^2}{B_b} - \frac{B''}{2} \right) (z^2 + y^2) \quad (3.14)$$

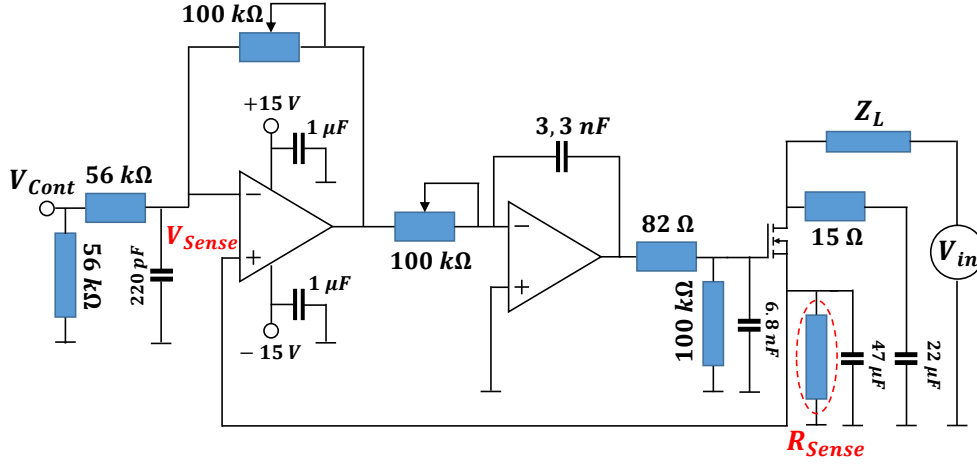


Figure 3.2: Schematics of the switch used in the experiment to drive the quadrupole coils. The current through the inductive load Z_L is kept at the desired value by a feedback loop that compares the voltage drop V_{Sense} across the sensing resistor R_{Sense} with the control voltage V_{Cont} selected by the user. To avoid fluctuation in the current value due to change in the value of R_{Sense} , the sensing resistor is water cooled .

The trapping potential created by this trap is well approximated, near the origin, with an anisotropic harmonic potential of the form:

$$U \approx \frac{\mu_m}{2} \left[\left(\frac{B'^2}{B_0} - \frac{B''}{2} \right) \rho^2 + B'' x^2 \right] \quad (3.15)$$

where $\rho^2 = z^2 + y^2$ and $\mu_m = g_F \mu_B m_F$. Far from the origin the potential is linear along the radial direction ($U_\rho = \mu B' \rho$) and harmonic along the axial.

The presence of a gravitational field modifies the potential to:

$$U = \mu_m \cdot |\mathbf{B}| - mgz \quad (3.16)$$

Gravity displaces the minimum so that the atoms are not positioned in it anymore. The magnetic field gradient required to compensate gravity is $B' = mg/\mu_m$, which is ≈ 30 G/cm for atoms in $|F = 1, m = -1\rangle$. Atoms with different magnetic moment

μ_1, μ_2 will then clearly occupy different positions in the trap, with a separation given by:

$$\Delta z = \frac{g}{\omega^2} \left(\frac{\mu_1}{\mu_2} - 1 \right) \quad (3.17)$$

and ω is the trapping frequency in the direction of gravity for atoms with magnetic moment μ_1

3.1.4 Magnetic traps on a chip

The main advantages in using miniaturized current-carrying structures on a chip surface to generate the magnetic field needed to trap atoms are:

- **Very strong confinement** (high field gradients)
- **Strong anisotropy** (extreme aspect ratios)

The magnetic field generated by an infinitely thin wire carrying a current I is:

$$B = \frac{\mu_0 I}{2\pi r} \quad (3.18)$$

It is clear from the previous equations that the closer the trap is to the wire, the stronger will be the confinement. However, losses induced by temporal fluctuations of the charge density inside the conducting wire, which creates a time dependent magnetic field that can induce spin-flips, and heating effects on the trapped atoms limit the minimum trap distance for copper wires to about 4 micrometers [77–79]. With superconducting wires these effects can be greatly suppressed, and the new limiting factors come in the form of van der Waals and Casimir-Polder forces, that cause atoms closer than a few hundred nanometers to fall on the trap surface [80]. In our experiments we use copper wires to generate our trap and the minimum distance of the cloud from the surface ranges from 140 to 180 micrometers.

A Z-shaped wire, combined with an homogeneous external bias magnetic field B_b perpendicular to the central part of the wire, produces an harmonic potential analogous to a Ioffe-Pritchard trap [81]. The application of an additional field B_\perp

perpendicular to B_b in the y direction allows the trap bottom B_0 of the Ioffe trap to be adjusted. The field created by such a configuration is, for thin wire, infinite end wires, close to the minimum and up to second order:

$$B(x, y, z) = B_0 + \frac{(y^2 + z^2)}{2B_0} \left(\frac{2\pi B_b^2}{\mu_0 I} \right)^2 + \frac{2\mu_0 r_0 I d_h^2 x^2}{\pi(d_h^2 + r_0^2)^3} \quad (3.19)$$

where d_h is the length of the middle wire, r_0 is the distance of the field minimum from the wire and the equation is valid if $r_0 \ll d_h$. We use such a configuration to trap atoms during the evaporation stage, in what we call a compressed magnetic trap (CMT). The trap frequencies can be calculated using:

$$\omega_y = \omega_z = \frac{2\pi B_b^2}{\mu_0 I} \sqrt{\frac{\mu_B}{2mB_0}} \quad (3.20)$$

$$\omega_x = \frac{\mu_0 I d_h}{\pi} \sqrt{\frac{\mu_B}{mB_b(d_h^2 + r_0^2)^3}} \quad (3.21)$$

and m is the mass of the atoms. For the typical experimental conditions with $I = 17$ A, $B_0 = 3.23$ G, $B_b = 26$ G and $d_h = 6.353$ mm we have $\omega_x = \omega_y \approx 2\pi \cdot 99.794$ Hz and $\omega_z \approx 2\pi \cdot 13.1$ Hz, not far from the measured values $\omega_{x,y} \approx 2\pi \cdot 97$ Hz and $\omega_z \approx 2\pi \cdot 11.7$ Hz. These formulae don't take into account the finite size of the end wires, providing results that differ slightly from the actual measured results. It is possible to calculate the field more precisely by adding the field generated, using the Biot-Savart law, by wire segments. Following this procedure, the field at a point \mathbf{P} created by a segment of length \mathbf{A} is [82]:

$$\mathbf{B} = \frac{\mu_0 I}{4\pi} \frac{\mathbf{C} \times \mathbf{A}}{|\mathbf{C} \times \mathbf{A}|^2} \left(\frac{\mathbf{A} \cdot \mathbf{C}}{|\mathbf{C}|} - \frac{\mathbf{A} \cdot \mathbf{B}}{|\mathbf{B}|} \right) \quad (3.22)$$

A U-shaped wire, again with a bias field B_b applied along the y direction, creates a quadrupole trap and it is used, due to the increased strength when compared with the field created by quadrupole coils, in the compressed MOT (CMOT) stage of the BEC production.

3.2 Laser Cooling

Laser cooling allows atoms to be cooled from the $\sim 500K$ of rubidium vapour released from the dispenser to $\sim 40\mu K$ of the atoms just after polarization gradient cooling (PGC). In this section a description is provided of the principles and realization of the various stages of cooling.

3.2.1 The MOT

The first step in the cooling process is achieved by exploiting the dissipative and confining force generated by two counter propagating, circularly polarized laser beams on atoms moving in an inhomogeneous magnetic field. This step can be achieved using a magneto-optical trap (MOT). To understand how this force is created we should consider a 1D model of an atom with an $F=0$ ground state and $F'=1$ excited state. The model can then be extended to 3D and $F \rightarrow F' = F + 1$ transitions.

The magnetic field created by quadrupole coils is zero at the origin. Its magnitude increases linearly with position, while its direction always points away from the origin. Two counter propagating laser beams of opposite circular polarization, σ^+ and σ^- , red detuned by δ from the $F = 0 \rightarrow F' = 1$ transition, illuminate the atom. If this atom is moving away from the origin in the $x > 0$ region, the Zeeman shift cause the $m_F = +1$ sub level to be shifted up, away from resonance and the $m_F = -1$ sub level to be shifted down, closer to resonance. If the polarization of the beam coming from the right is chosen to be σ^- then the atom will scatter more photons from the σ^- beam than from the σ^+ and the atom will experience a force toward the center of the trap. on the other side of the trap, for $x < 0$, the sub levels are reversed and more photons will be scattered from the left propagating σ^+ beam, again sending the atom towards the center. The total force is [75]:

$$F = \frac{\hbar k \gamma}{2} \frac{s_0}{1 + s_0 + (2\delta_+/\gamma)^2} - \frac{\hbar k \gamma}{2} \frac{s_0}{1 + s_0 + (2\delta_-/\gamma)^2} \quad (3.23)$$

where $s_0 = I/I_{sat}$, with I_{sat} the saturation intensity (for ^{87}Rb and isotropic light

polarization $I_{sat} = 3.576 \text{ mW/cm}^2$) [69], γ is the spontaneous emission rate, $\hbar k$ is the momentum per photon and δ_{\pm} is the detuning given by:

$$\delta_{\pm} = \delta \mp k \cdot v \pm \frac{\mu' B}{\hbar} \quad (3.24)$$

$\mu' = (g_{F+1}m_{F+1} - g_F m_F)\mu_B$ is the effective magnetic moment, $k \cdot v$ is the Doppler shift and $\mu' B/\hbar$ is the Zeeman shift. When the Zeeman shift and the Doppler shift are small compared to the detuning δ we can expand eq. (3.23) and obtain:

$$F = -\beta \cdot v - \kappa \cdot r \quad \beta = \frac{8\hbar k^2 \delta s_0}{\gamma[1 + s_0 + (2\delta_+/\gamma)^2]^2} \quad \kappa = \frac{\mu' b}{\hbar k} \beta \quad (3.25)$$

and β is the damping coefficient while b is the magnetic field gradient. As we can see from eq. (3.25) the force is both cooling (term proportional to v) and confining (term proportional to r). The lowest temperature (Doppler limit) achievable by exploiting this damping force is:

$$T_D = \frac{\hbar \gamma}{2k_B} \quad (3.26)$$

and for rubidium is $T_D = 146 \mu\text{K}$. This limit, which is called Doppler limit, arises because the spontaneous emission of photons is a stochastic process and the force has fluctuations that produce heating. Such a process can be analyzed using the Fokker-Planck equation [75].

The MOT laser used in the experiment is a commercial Littrow external cavity Topptica DLX110, red detuned by $\delta = -18 \text{ MHz}$ from the cyclic transition $5^2S_{1/2}(F_g = 2) \rightarrow 5^2P_{3/2}(F_e = 3)$ to which it is locked by Doppler-free polarization spectroscopy. The detuning is controlled by acousto-optical modulators (AOM) that also serve as a high speed switch due to the fact that only the +1 diffraction order is coupled to the fiber and delivered to the atoms. The power delivered to the atoms is 200 mW. To prevent population loss to the dark state $5^2S_{1/2}(F_g = 1)$ from the short-lived $5^2P_{3/2}(F_e = 3)$ ($\tau \approx 26 \text{ ns}$) a repumping beam is mixed with the MOT laser. This repumping beam is created by an external cavity Littrow configured Topptica DL100 laser, frequency locked by Doppler free saturation spectroscopy to

the transition $5^2S_{1/2}(F_g = 1) \rightarrow 5^2P_{3/2}(F_e = 2)$. This transition is more favorable than $5^2P_{3/2}(F_e = 1)$ because Clebsch-Gordan coefficients are an order of magnitude larger and repumping occurs faster. The repumping power delivered to the atoms is ≈ 7 mW. Figure 3.3 provides a representation of the transitions used during laser cooling.

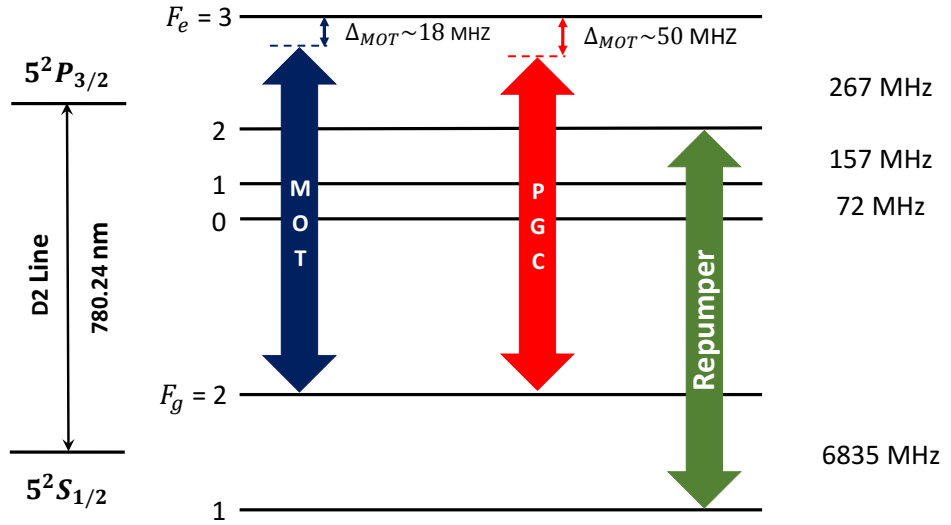


Figure 3.3: ^{87}Rb energy levels together with the transitions used in the laser cooling stage.

3.2.2 Polarization Gradient Cooling

It is possible to achieve further cooling by using polarization gradient cooling (PGC). In our experiment use two counter propagating $\sigma^+ - \sigma^-$ beams to create a linearly polarized electric field which rotates by 2π over one optical wavelength. Atoms at rest in such field will have the populations of their $F = 1$ state equally distributed between the light shifted $m_F = \pm 1$ substates, with the sub-state $m_F = 0$ more strongly populated. Moving atoms, by contrast, experience a rotation of the polarization vector and we can think of them as dipoles trying to follow the polarization vector. However, due to the finite optical pumping time, the population of

the ground substates always lags behind the steady state-distribution for the local polarization direction. This lag translates into an imbalance of population of the $m_f = \pm 1$ substates. More specifically, for atoms traveling toward the σ^+ beam the $m_f = 1$ will be more populated than the $m_f = -1$ and vice-versa for atoms moving toward the σ^- beam. This imbalance in turn cause more photons to be scattered from one beam than the other, cooling down the atoms. The minimum temperature achievable with PGC is [83]:

$$T_{PGC} \approx \frac{\hbar\gamma^2}{I_{sat}k_B} \frac{I}{|\delta|} \quad (3.27)$$

and depends inversely on the detuning δ and directly on the intensity I of the laser beam. In the experiment, PGC is performed by using the MOT laser beams, which already have the correct polarization pattern and by increasing the detuning from 18 MHz to ≈ 50 MHz. At the same time, the magnetic field gradient is reduced by a factor of ten. This is done because in the presence of magnetic field the atoms are damped toward a non-zero velocity given by ω_z/k , where ω_z is the Zeeman precession frequency. The repumper beam is applied, for the same reasons explained in the MOT section, throughout the PGC. At the end of a 10 ms cycle, the atoms have a temperature of about 40 μ K. The measured value is quite close to the result $T_{PGC} = 26 \mu$ K obtained by applying equation (3.27) with the typical experimental parameters $I = 200 \text{ mW/cm}^2$ and $\delta = 2\pi \cdot 50 \text{ MHz}$.

3.2.3 Optical pumping

Optical pumping is not a cooling process, but it is a crucial step in BEC preparation. After the PGC the atoms are spread across all the magnetic substates from $m_F = -2$ to $m_F = +2$. Only the low field seeking atoms can be trapped in our compressed magnetic trap (CMT). In order to maximize the transfer of atoms into the magnetic trap we optically pump them to $|F = 1, m_F = -1\rangle$, which is also the stretched state we use for BEC creation. The laser employed for optical pumping is a home-made external cavity, Littrow configured, diode laser similar in

design to a Toptica DL100. The laser is locked, using polarization spectroscopy, to the $5^2S_{1/2}(F_g = 2) \rightarrow 5^2P_{3/2}(F_e = 3)$ transition and then shifted down, by double passing through an AOM, by 260 MHz to be detuned by ≈ 10 MHz from the $5^2S_{1/2}(F_g = 2) \rightarrow 5^2P_{3/2}(F_e = 2)$ transition. We chose to lock the laser around $5^2S_{1/2}(F_g = 2) \rightarrow 5^2P_{3/2}(F_e = 3)$ because this transition has a stronger polarization resonance. The transition $5^2S_{1/2}(F_g = 2) \rightarrow 5^2P_{3/2}(F_e = 2)$ was chosen because it does not lead to cloud heating that would have occurred if a cycling transition such as $5^2S_{1/2}(F_g = 2) \rightarrow 5^2P_{3/2}(F_e = 3)$ was used. The optical pumping is performed in two stages. In the first stage a mostly σ^- with a small π -polarization component optical pumping beam is applied simultaneously with a σ^- polarized repumper beam to avoid population loss to the dark state $F_g = 1$. This stage lasts for 1.6 ms. At the end of the first stage, most of the atoms are in $|F = 2, m_F = -2\rangle$. In the second stage the repumper is shut off and the population is transferred from $|F = 2, m_F = -2\rangle$ to $|F = 1, m_F = -1\rangle$ via relaxation of the intermediate $5^2P_{3/2}(F_e = 2)$ state. The second stage lasts for 0.7 ms. The efficiency of the process is $\sim 90\%$. A schematic representation of the transitions involved in the optical pumping process is presented in figure 3.4

3.3 Hyperfine Manipulation

In our experiments we often deal with BECs of atoms in more than one hyperfine state. This section describes the structure of ^{87}Rb hyperfine states and how we experimentally manipulate them.

3.3.1 Atomic system

Atoms of ^{87}Rb in the $5^2S_{1/2}$ state have electron angular momentum quantum number $J = 1/2$ and nuclear angular momentum $I = 3/2$. The total angular momentum F can take values $|J - I| \leq F \leq J + I$, hence we have two hyperfine states, $F = 1$

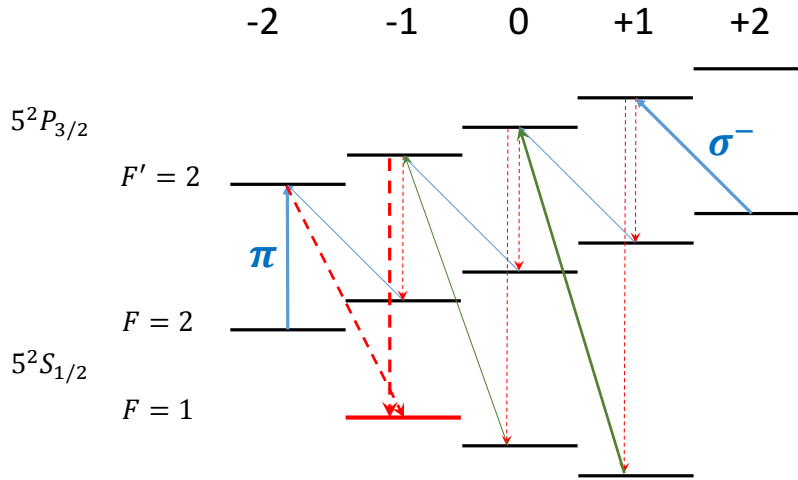


Figure 3.4: Optical pumping to the $|F = 1, m_F = -1\rangle$ state. Blue lines represent light absorbed from the optical pumping beam, with mainly σ^- and a fraction of π polarization. Green lines represent repumper radiation that prevents states different than $|F = 1, m_F = -1\rangle$ from being populated. Red dashed lines describe spontaneous emission. A full description of the process is provided in the text.

and $F = 2$. In an external magnetic field, these hyperfine levels split into three and five Zeeman sublevels, respectively. For a weak magnetic field ($B \ll 10^3$ G) the magnetic moment is $\mu_1 \approx -m_F \mu_B / 2$ for $F = 1$ and $\mu_2 \approx m_F \mu_B / 2$ for $F = 2$ (see figure 3.5). The hyperfine splitting energy between $F = 1$ and $F = 2$ is $\Delta_{hfs} \approx 6.83462861090429(9)$ GHz [69] and lies in the microwave range. To create a two-component BEC (2CBEC) in a magnetic trap we are left with only two possible low-field seeking states, $|F = 2, m_F = +1\rangle$ and $|F = 2, m_F = +2\rangle$, apart from $|F = 1, m_F = -1\rangle$, which is the state we condense to. We choose $|F = 2, m_F = +1\rangle$ over $|F = 2, m_F = +2\rangle$ because:

- $|F = 1, m_F = -1\rangle$ and $|F = 2, m_F = +1\rangle$ have the same magnetic moment, apart from a very small second order Zeeman shift correction and they occupy the same position in the trap.

- $|F = 1, m_F = -1\rangle \rightarrow |F = 2, m_F = +1\rangle$ is a two photon transition, more efficient by a factor $\sim 10^3$ than the three photon $|F = 1, m_F = -1\rangle \rightarrow |F = 2, m_F = +2\rangle$

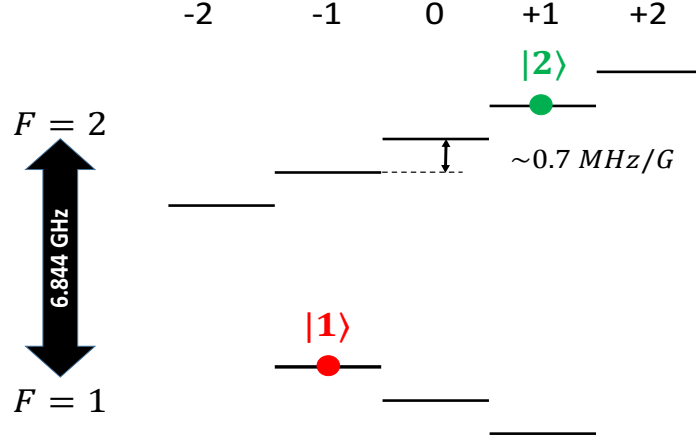


Figure 3.5: Ground state of ^{87}Rb showing the two hyperfine levels $F=1$ and $F=2$ and their Zeeman split sublevels. The frequency separation between $F=2$ and $F=1$ is ≈ 6.844 GHz while the separation between sublevels is ≈ 0.7 MHz/G. The states $|F = 1, m_F = -1\rangle$ and $|F = 2, m_F = 1\rangle$ used in the experiments have been highlighted.

However this choice is not without a cost, since in the state $|F = 2, m_F = +1\rangle$ two body recombinations are not suppressed and lifetime is shorter. For the special case of $B_0 = 3.228917$ G, the difference in Zeeman energy between the states $|F = 1, m_F = -1\rangle$ and $|F = 2, m_F = +1\rangle$ is independent of the fluctuations of B to first order [84] (see figure 3.6). This provides us with the added benefit of differential magnetic field noise insensitivity for the chosen transition. The Zeeman sublevels of each hyperfine state experience a B dependent shift that can be precisely calculated using the Breit-Rabi formula eq. (3.7), but is often approximated with ≈ 0.7 MHz/G. For our usual condition of $B = 3.229$ G this shift amounts to 2.26 MHz. The splitting between the states $|F = 1, m_F = -1\rangle$ and $|F = 2, m_F = +1\rangle$ around B_0 is [84]

$$\Delta E = 2\pi\hbar[f_0 + \beta(B - B_0)^2] \quad (3.28)$$

$$f_0 = 6.834678113.59 \text{ Hz} \quad \beta = 431.35947 \text{ Hz/G}^2 \quad (3.29)$$

The hyperfine states and relative Zeeman sublevels are coupled by an electromag-

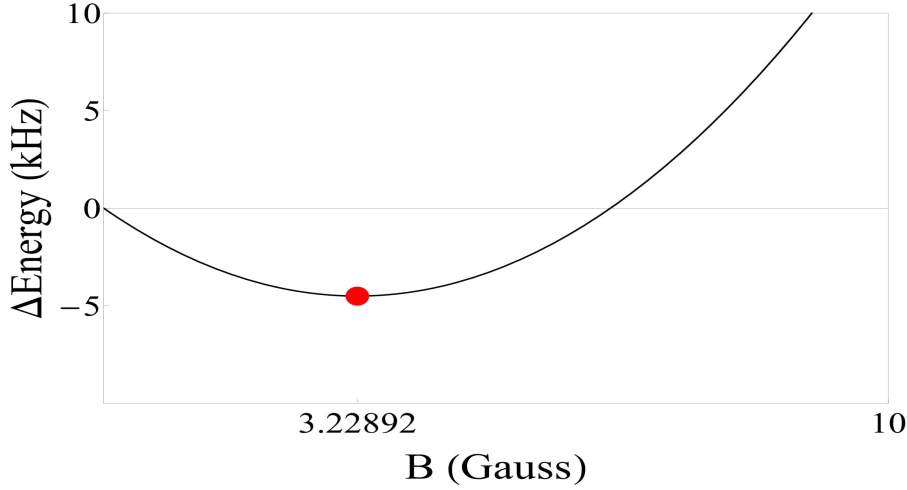


Figure 3.6: Energy difference of the levels $|F = 1, m_F = -1\rangle$ and $|F = 2, m_F = 1\rangle$ relative to the hyperfine splitting energy $E_{hfs}/h = f_{hfs}$ for different values of the external magnetic field \mathbf{B} . The minimum is reached for $\approx 3.229 \text{ G}$ leading to the cancellation of the first order Zeeman shift (**red dot**). The dependence of the energy for small values of B around B_0 is parabolic, see equation (3.28).

netic field through magnetic dipole transitions. The transition frequency can be in the radiofrequency range (between Zeeman states) or in the microwave range (between hyperfine states) and can be single or multiphoton. By considering the coupling Hamiltonian $\hat{H}_{rf} = -\hat{\mu} \cdot B_{rf} \cos \omega_{rf} t$, where B_{rf} is the amplitude of the RF field and ω_{rf} is the angular frequency of the RF field, it is possible to calculate the coupling strength for every given transition and field polarization. If we assume:

$$\hat{\mu} = \frac{\mu_B g_f}{\hbar} \hat{F} \quad (3.30)$$

then the off-diagonal matrix elements of H_{ref} in the $|F, m_f\rangle$ basis are:

$$\text{RF } \sigma^\pm \text{ transitions: } \langle F, m_F \pm 1 | \hat{H}_r f | F, m_F \rangle = \frac{\hbar\Omega_\sigma}{2} \sqrt{F(F+1) - m_F(m_F \pm 1)} \quad (3.31)$$

$$\text{MW } \sigma^\pm \text{ transitions: } \langle F', m_F \pm 1 | \hat{H}_r f | F, m_F \rangle = \pm \frac{\hbar\Omega_\sigma}{2} \sqrt{(I \pm m_F + 1)^2 - \frac{1}{4}} \quad (3.32)$$

$$\text{MW } \pi \text{ transitions: } \langle F', m_F \pm 1 | \hat{H}_r f | F, m_F \rangle = \frac{\hbar\Omega_\pi}{2} \sqrt{(2I+1)^2 - 4m_F^2} \quad (3.33)$$

where $\Omega_\sigma = \mu_B g_F B_\perp / 2\hbar$ is the Rabi frequency for the σ^\pm transitions and $\Omega_\pi = \mu_B g_F B_\parallel / 2\hbar$ is the Rabi frequency for π transitions. With the coupling strength and by assuming that all atoms start at $t = 0$ in a stretched state $|F, m_F = \pm F\rangle$, we can calculate the populations at time t in each state by using [48]:

$$|\psi_{m_F}\rangle^2 = \frac{(2F)!}{(F+m_F)!(F-m_F)!} |c_1^{F+m_F}|^2 |c_2^{F-m_F}|^2 \quad (3.34)$$

where

$$|c_1|^2 = \frac{\delta^2}{\Omega_{rf}^2} + \frac{\Omega_{rf}^2}{\Omega_{rf}^2 + \delta^2} \cos^2 \left(\frac{\sqrt{\Omega_{rf}^2 + \delta^2}}{2} t \right) \quad (3.35)$$

$$|c_2|^2 = \frac{\Omega_{rf}^2}{\Omega_{rf}^2 + \delta^2} \sin^2 \left(\frac{\sqrt{\Omega_{rf}^2 + \delta^2}}{2} t \right) \quad (3.36)$$

and δ is the detuning while Ω_{rf} is the coupling strength calculated before.

For two photon transitions like $|F = 1, m_F = -1\rangle \rightarrow |F = 2, m_F = +1\rangle$ the treatment is slightly different. If both photons are sufficiently detuned from the intermediate state ($|F = 1, m_F = 0\rangle$ or $|F = 2, m_F = 0\rangle$), then the three level system can be reduced to two levels by *adiabatic elimination* [48]. The two photon Rabi frequency is, to first order in the detuning from the intermediate level Δ :

$$\Omega_{2ph} \approx \frac{\Omega_1 \Omega_2}{2\Delta} \quad (3.37)$$

where Ω_1, Ω_2 are the coupling strengths for the RF and Mw transitions, respectively, and we have assumed the two photon detuning $\delta_{2ph} = 0$.

The leakage to an intermediate state is well approximated by [48]:

$$\sum_{|i\rangle \neq |1\rangle, |2\rangle} \langle |c_i|^2 \rangle \approx \frac{6\Omega_1^2 + 3\Omega_2^2}{3\Delta^2} \quad (3.38)$$

Equations(3.37) and (3.38) shows that the smaller is the detuning Δ from the intermediate state, the faster is the Rabi frequency, but the higher will be the unwanted leakage of atoms to the intermediate level. For this reason we keep $\Delta = 2\pi \times 1$ MHz, which limits leakage to negligible levels and gives a two-photon Rabi frequency, in typical experimental conditions, of $\Omega_{2ph} = 2\pi \times 510$ Hz. Figure 3.7 provides a summary of the relevant transitions, their polarizations and Rabi frequencies.

3.3.2 Microwave setup

We use two different microwave synthesizers to produce the microwave signal. The first one is an Agilent E8257D with a frequency resolution of 0.001 Hz, switching speed of 7 ms and phase noise as in table 3.1. With switching speed we refer to the time required by the MW synthesizer internal electronics to modify the phase of a signal.

Phase Noise at 10 GHz	dBc/Hz
100 Hz	-84
1 kHz	-106
10 kHz	-115
100 kHz	-115

Table 3.1: Phase noise for an Agilent E8257D

The second synthesizer is a FSW-0010 QuickSyn with a frequency resolution of 0.001 Hz, switching time of 100 μ s and phase noise as in table 3.2.

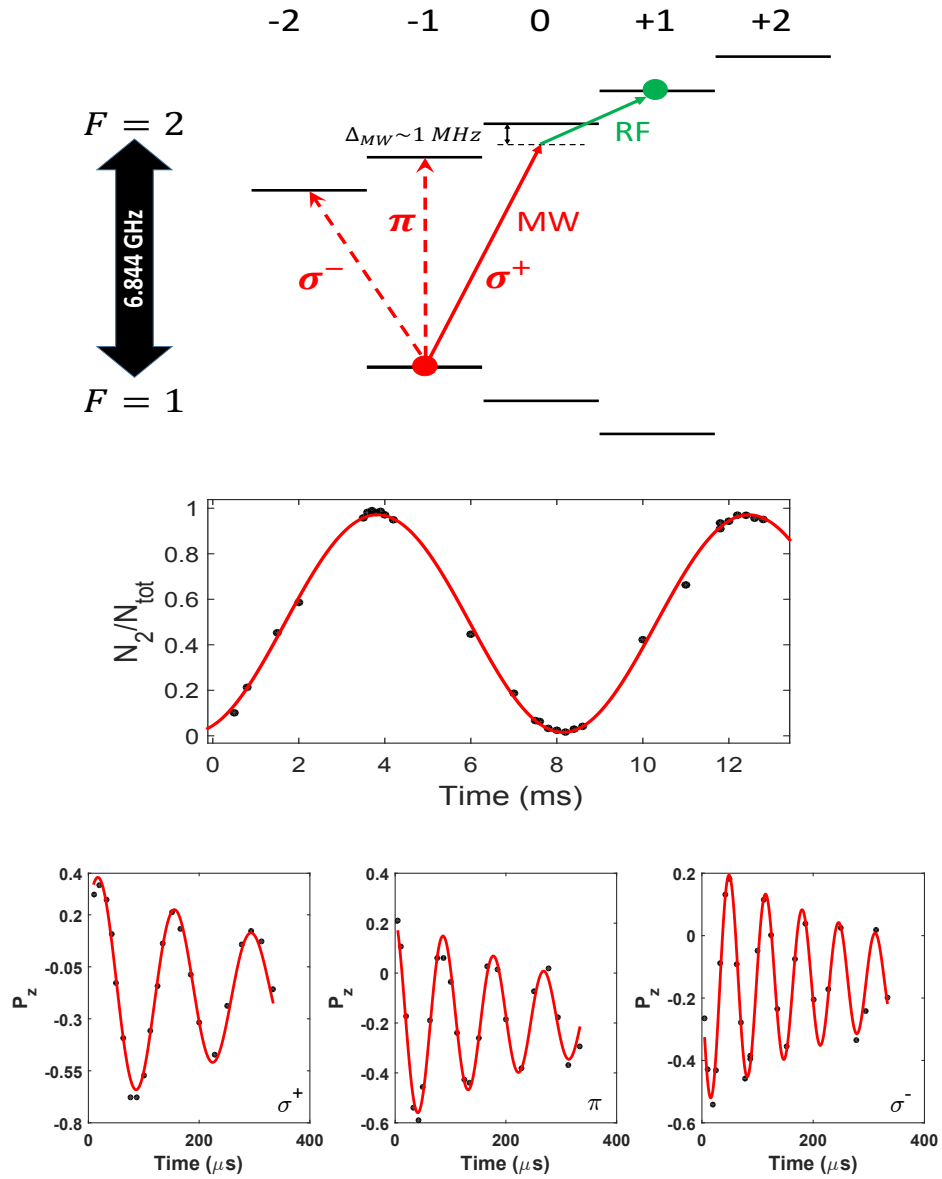


Figure 3.7: MW transitions (red lines) and RF transitions (green line) used in the experiments (top). The solid lines represent two photon transitions between the clock states $|F = 1, m_F = -1\rangle$ and $|F = 2, m_F = +1\rangle$. To avoid population of $F = 2, m_F = 0\rangle$, the MW field is detuned by $\approx 1 \text{ MHz}$. The two photon detuning is close to zero. The Rabi frequency for the two-photon transition is typically $\Omega_2 \approx 2\pi \cdot 125 \text{ Hz}$ and the amplitude, obtained by fitting a sinusoid, is close to 1 (center). One-photon MW transitions are used for MW spectroscopy and adiabatic passage imaging sequence, particularly the π polarized $|F = 1, m_F = -1\rangle$ to $|F = 2, m_F = -1\rangle$ transition (bottom). P_z is defined as the relative atom number difference (e.g. $N_2 - N_1/N_2 + N_1$)

Phase Noise at 10 GHz	dBc/Hz
100 Hz	-83
1 kHz	-112
10 kHz	-122
100 kHz	-121

Table 3.2: Phase noise for an FSW-0010 QuickSyn

The FSW-0010 has a much faster switching time and better phase noise characteristics, but due to a problem with the triggering, which prevents us from doing Ramsey spectroscopy in the phase domain, we use both. Both synthesizers are locked to an external 10 MHz OCXO 8607 quartz oscillator for improved stability. The signal produced by both synthesizers has a typical power of 3 dBm. This signal is sent to a reflective switch (Agilent N9397A) that can be switched between a 50 Ω terminator and a 20 W MW amplifier. After being amplified it propagates along a 50 Ω coaxial line to a uni-directional coupler which can be used as part of a diagnostic circuit. After the unidirectional coupler, two MW isolators, circulators with one absorbing port, dissipate all the power reflected by the antenna. We use two different kinds of antenna: the first, now removed from the setup but used until recently, was an impedance matched dipole antenna that radiated $\approx 90\%$ of the power and the other, currently in use, is a toroidal antenna that creates a field ≈ 3 times stronger than the dipole antenna at the atom position. The antennas are located outside the vacuum chamber, about 12 cm away from the atoms. Figure 3.8 provides a schematic description of the setup. The MW field generated has all three polarization components with the power distributed unevenly between the different polarizations (figure 3.7). Measurements [82] based on the Rabi frequency of the single photon transitions $|F = 1, m_F = -1\rangle \rightarrow |F = 2, m_F = -2, -1, 0\rangle$ show $\Omega_- = 2\pi \times 15.23(6)$ kHz for σ_- , $\Omega_+ = 2\pi \times 7.23(5)$ kHz for σ_+ , $\Omega_\pi = 2\pi \times 11.01(8)$ kHz for π , signaling a higher distribution of power in σ^- and π .

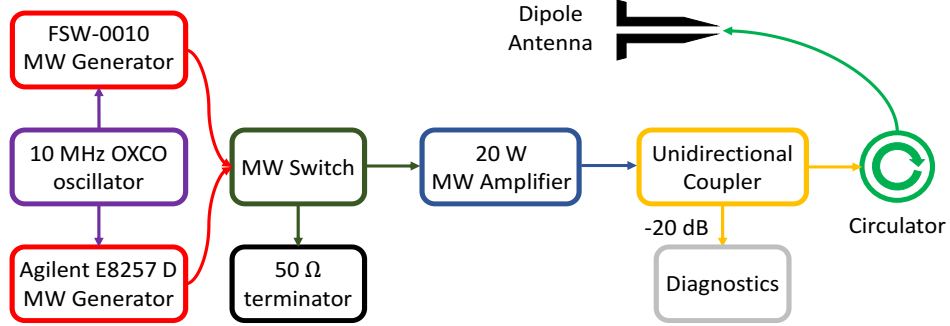


Figure 3.8: MW setup scheme. The signal is produced by either the Agilent E8257 D or the FSW-0010 synthesizers clocked by the OXCO quartz oscillator or the internal clock (not shown) of the Agilent synthesizer. The signal from the reference oscillator is fed directly to the MW synthesizers. A switch then sends the signal to the 20 W amplifier and, via components that assure no reflected power can harm the amplifier, to a dipole antenna. A small part of the signal (≈ -20 dB) is sent to diagnostic instruments for measurements.

3.3.3 Magnetic field calibration

In order to measure the magnitude of the magnetic field, we perform single photon microwave spectroscopy. The idea is to transfer the atoms from the condensed state $|F = 1, m_F = -1\rangle$ to one of the untrapped states $|F = 2, m_F = -2, -1, 0\rangle$ via the application of a MW pulse whose lengths $t_{pulse} > \Omega$ for the chosen transition. Typical pulse length are $t_{pulse} = 500 \mu\text{s}$, corresponding to five full cycles for the σ^+ transition, which has the smallest Rabi frequency. Then the MW field is switched off and the atoms are held in the trap for $t_{hold} = 0.3$ ms. During this holding time the Stern-Gerlach effect separates the clouds, making it easy to measure the population of outcoupled N_2 relative to the total number of atoms N . By scanning the frequency of

the MW field we obtain a Lorentzian shaped profile with the maximum corresponding to the energy separation of the two coupled levels for the given magnetic field (see figure 3.9). We want our magnetic field to be $B_0 \approx 3.229$ G at the trap bottom and this implies a separation between the Zeeman substates $f_{B_0} \approx 2.26$ MHz and a MW resonant frequency $f_{tot} \approx \Delta_{hfs} + f_{B_0}$. The widths of the Lorentzian profiles are different for different polarizations and range from $\Gamma_+ \approx 10$ kHz for σ^+ to $\Gamma_\pi \approx 20$ kHz for π . The main reason for this width lies in the size of the cloud and gravitational sag. In fact, because of gravitational sag the cloud does not sit in the potential minimum, but sees a field gradient of dB/dz . Different sections of the cloud experience different magnetic fields which cause different energy shifts. The energy difference between the top and bottom of a 10^5 atoms BEC is ≈ 18 kHz. Other source of broadening are to be expected from motional effects (sloshing), power broadening and magnetic field instabilities (e.g. stray fields).

3.4 Imaging

This section describes absorption imaging, the technique used in the experiment to obtain information on cold atoms cloud. The laser used for imaging is a Toptica DL100 locked to the transition $F = 2 \rightarrow F' = 3$ using polarization spectroscopy. The laser is controlled by MogLabs electronics and the detuning change by a double pass AOM. The optical setup is described and the resolution is measured.

3.4.1 Absorption imaging

When an atomic cloud interacts with a laser beam of near-resonant light, it scatters some of the light and creates a shadow in the beam that can be detected by a CCD camera. This fluorescence problem can be simplified by approximating the cloud as a two-level system and the laser beam as a monochromatic field. The approximation

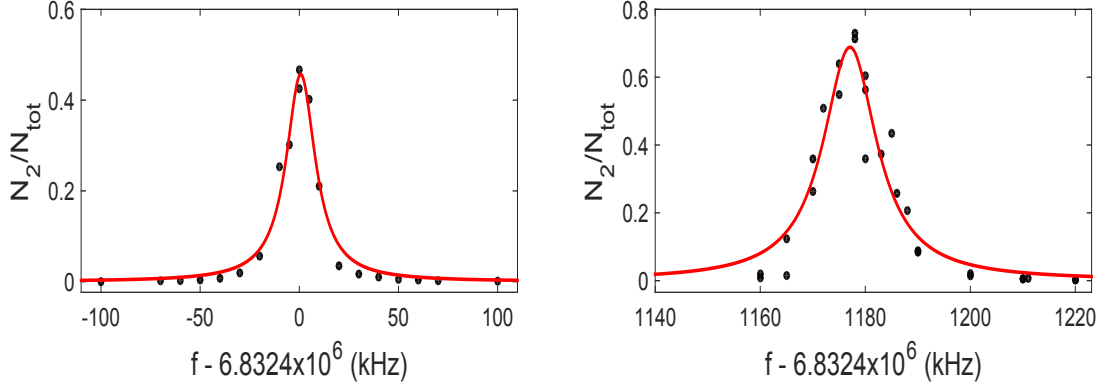


Figure 3.9: Microwave spectroscopy on the σ^+ transition $|F = 1, m_F = -1\rangle$ to $|F = 2, m_F = 0\rangle$. The number of atoms leaving the trap after being transferred in the untrapped state $F = 2, m_F = 0\rangle$ is measured and normalized over the total number of atoms. A Lorentzian function is fitted (red line) and, after the application of Breit-Rabi, equation(3.7), a magnetic field of 3.23 Gauss (left) and 1.5 Gauss (right) is calculated. The slight asymmetry in the Lorentzian that can be observed for the lower value of the magnetic field is due to gravity sag [85]. The width, taken as HWHM, is ≈ 15 kHz

allows us to derive a set of optical Bloch equations [69, 86]

$$\begin{aligned}
 \frac{d}{dt}\rho_{gg} &= i\frac{\Omega}{2}(\tilde{\rho}_{ge} - \tilde{\rho}_{eg}) + \Gamma\rho_{ee} \\
 \frac{d}{dt}\rho_{ee} &= -i\frac{\Omega}{2}(\tilde{\rho}_{ge} - \tilde{\rho}_{eg}) - \Gamma\rho_{ee} \\
 \frac{d}{dt}\rho_{ge} &= -\left(\frac{\Gamma}{2} + i\Delta\right)\tilde{\rho}_{ge} - i\frac{\Omega}{2}(\rho_{ee} - \rho_{gg})
 \end{aligned} \tag{3.39}$$

Where Ω is the resonant Rabi frequency, Δ is the detuning and Γ is the natural decay rate of the excited state. Equations (3.39) make use of a master equation approach to model spontaneous emission and are valid in the rotating wave approximation. In addition, there is no decay due to collisions and the motion of the atoms has been neglected. The steady state population of the excited state is [69]

$$\rho_{ee} = \frac{(\Omega/\Gamma)^2}{1 + 4(\Delta/\Gamma)^2 + 2(\Omega/\Gamma)^2} \tag{3.40}$$

and the steady state photon scattering rate is

$$R_{se} = \frac{\Gamma}{2} \frac{(I/I_{sat})}{1 + 4(\Delta/\Gamma)^2 + (I/I_{sat})} \quad (3.41)$$

with

$$\frac{I}{I_{sat}} = 2 \left(\frac{\Omega}{\Gamma} \right)^2 \quad I_{sat} = \frac{c\epsilon_0\Gamma^2\hbar^2}{4|\hat{\epsilon} \cdot \mathbf{d}|^2} \quad (3.42)$$

From equation (3.42) it is clear that the saturation intensity depends on the polarization of the light $\hat{\epsilon}$ through the corresponding dipole interaction matrix element. $I_{sat} = 1.67 \text{ mW/cm}^2$ [69] for pure σ^\pm light for the $^{87}\text{Rb } 5^2S_{1/2}(F_g = 2) \rightarrow 5^2P_{3/2}(F_e = 3)$ cycling transition, while $I_{sat} = 3.05 \text{ mW/cm}^2$ [69] for π polarization. Using equation (3.41) we can define the scattering cross section, which is equal to the power radiated by the atoms divided by the incident energy flux

$$\sigma = \frac{\sigma_0}{1 + 4(\Delta/\Gamma)^2 + (I/I_{sat})} \quad \sigma_0 = \frac{\hbar\omega\Gamma}{2I_{sat}} \quad (3.43)$$

The Beer-Lambert law for absorption

$$\frac{dI}{dz} = n(x, y, z)\sigma(I) \quad (3.44)$$

allow us to express the column density $n(z)$, in the resonant case ($\Delta = 0$) as [87]

$$n(x, y) = \frac{1}{\sigma_0} \ln \left(\frac{I_{abs}}{I_{bg}} \right) + \frac{I_{bg} - I_{abs}}{I_{sat}} \quad (3.45)$$

where I_{bg} is the intensity of the light collected on a frame without atoms, I_{abs} is the intensity from the absorption frame. To measure I_{sat} we rewrite equation eq. (3.45) as

$$\sum I_{bg}(1 - e^{\sigma_0 n_0}) = I_{sat}N - I_{sat} \sum n_0 \quad (3.46)$$

where the summation is done over the pixels of the frame. By varying the imaging laser intensity I_{bg} and since the total number of atoms effectively present is independent of I_{bg} and assumed to change only slightly from shot to shot, we obtain a linear relationship between the atoms detected $\sum n_0$ and I_{bg} whose slope is I_{sat} . The intensity is measured by the CCD as counts per pixel according to the following formula

$$I = \frac{\hbar\omega k}{qgA_{ps}\tau} \quad (3.47)$$

where q is the quantum efficiency of the camera, g is the gain of the camera amplifier, k is the counts per pixel and A_{ps} is the effective pixel area. We obtain a value of $I_{sat} = 8.4 \cdot 10^3 \pm 1.3 \cdot 10^3$ counts [85] for an effective pixel size of $4 \mu\text{m}$, with the uncertainty largely due to the instability in the atom number N ($\sim 10\%$ variation). In order to compensate for imperfect light polarization, Doppler shift due to photon recoil and the presence of additional sublevels that might be populated, all factors that influence the value of I_{sat} , it is possible to replace in the previous equations I_{sat} with $I_{eff} > I_{sat}$ and σ_0 with $\sigma_{eff} < \sigma_0$ and adjust them such that the detected atom number is independent of the imaging laser intensity. In order to reduce fringing and laser light fluctuations which also affect atom number measurement we use a Princeton ProEm 512 CCD camera that allows us to collect the absorption and reference frame with a delay as small as $400 \mu\text{s}$ by using a function called "kinetics mode" by the producer. Kinetics mode essentially consist of masking half of the sensitive area of the CCD chip, reducing it from 512×1040 active pixels to 512×520 and exploit the much faster transfer rate of the charge stored in the pixel compared to the slow A/D conversion process. This way only the top half of the camera is exposed to the laser beam, the signal then shifted to the masked region with a shifting time of $\sim 0.6 \mu\text{s}$ per row, adding up to $\sim 400 \mu\text{s}$ compared to the two second usually required for a full readout.

3.4.2 Imaging System

We use two different lenses arrangements in our imaging setup. The first is a pair of two back-to-back achromat lenses (Thorlabs AC508-150-B and AC508-500-B) with focal lengths $F_1 = 150 \text{ mm}$ and $F_2 = 500 \text{ mm}$ and a diameter of 50 mm . The lenses are positioned outside the vacuum chamber at a distance from the cloud which is approximately equal to the first lens focal length. The CCD camera is placed on a sliding support at the other lens focal point. The sliding support allows us to compensate for imperfection in the positioning of the lenses, even though optimal

focus is hard to achieve given the difficulty in positioning the first lens with respect to the actual cloud. The theoretical magnification is $M = F_2/F_1 = 3.3$ giving a theoretical effective pixel size of $16.3 = 4.8 \mu\text{m}$, where $16 \mu\text{m}$ is the physical size of a pixel for a ProEm 512 CCD camera. The measured value of the effective pixel size, obtained by dropping a cloud under gravity and fitting the position with a parabolic dependence, is $4 \mu\text{m}$, giving an effective magnification of $M_{eff} = 4$. The Rayleigh limited resolution of the system is given by

$$\sigma_{rayleigh} = 1.22 \frac{\lambda F_1}{D} \quad (3.48)$$

where λ is the wavelength and D is the lens diameter. The diffraction limited result for our case is $2\sigma_{rayleigh} = 5.72 \mu\text{m}$ but the real resolution is worse than $\sigma_{rayleigh}$ because part of the light is shadowed by the atom chip surface. The effective resolution is obtained by measuring the Gaussian beam waist at the focal point. The focal point is defined as the position of the CCD camera that minimizes the radial FWHM of an imaged condensate of $N \sim 10^5$ atoms. The minimum FWHM obtained is $27.2 \mu\text{m}$, 4.75 times worse than the ideal case. The typical Thomas-Fermi radius for $N \sim 10^5$ atoms trapped in our experimental conditions is $\sim 5 \mu\text{m}$ in the radial and $\sim 50 \mu\text{m}$ in the axial direction.

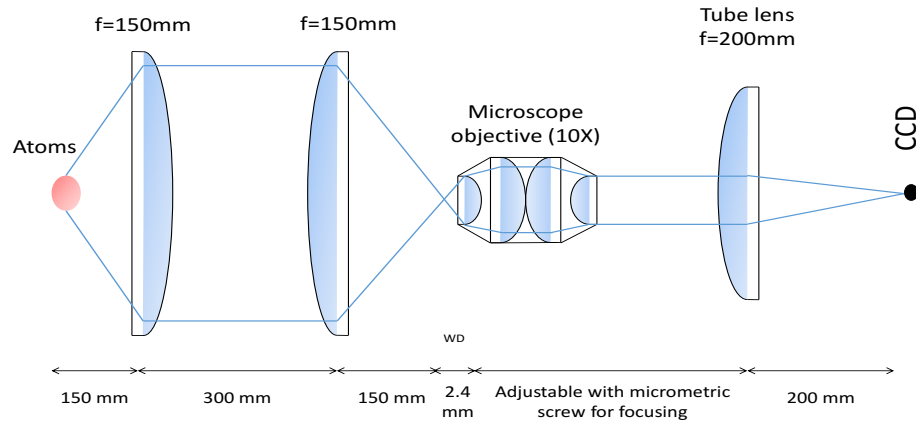


Figure 3.10: Imaging system setup. Two achromatic doublets with focal length 150 mm in a $4f$ configuration capture the image of the shadow created by an atomic cloud illuminated by laser light resonant with the transition $F = 2 \rightarrow F' = 3$ of ^{87}Rb . The image is then magnified by a microscope objective and focused on a CCD chip.

The second imaging setup, shown schematically in figure 3.10, uses two achromatic doublets (LAP-150.0-30.0) with focal length 150 mm in a $4f$ configuration. This configuration creates an image of the atom cloud with a 1:1 magnification. This image is subsequently magnified by a microscope objective ($\times 10$ Olympus Aplanat) and is focused on the CCD chip by a lens with focal length 200 mm. The nominal magnification for the system is 10, but the measurements, performed with the same technique described above, give a value 10.9, for an effective pixel size of $1.47 \mu\text{m}$. Typical images obtained with both configurations are shown in figure 3.11, along with an image of the grating used to measure resolution for the configuration involving the microscope objective. The resolution is measured first by imaging a transmission grating with a $10 \mu\text{m}$ period and then fitting an Airy function to the intensity distribution of a single slit giving a value $\sim 4 \mu\text{m}$. This is the best-case-scenario resolution, since everything is aligned correctly and focused optimally. The effective value obtained from the waist at the focal point of a Gaussian profile fitted to the minimum radial width of the condensate gives a value of $\sim 10 \mu\text{m}$.

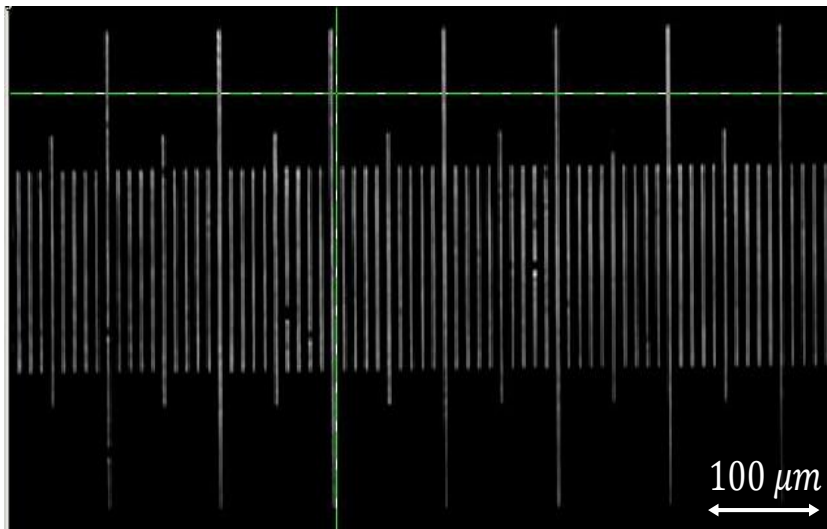
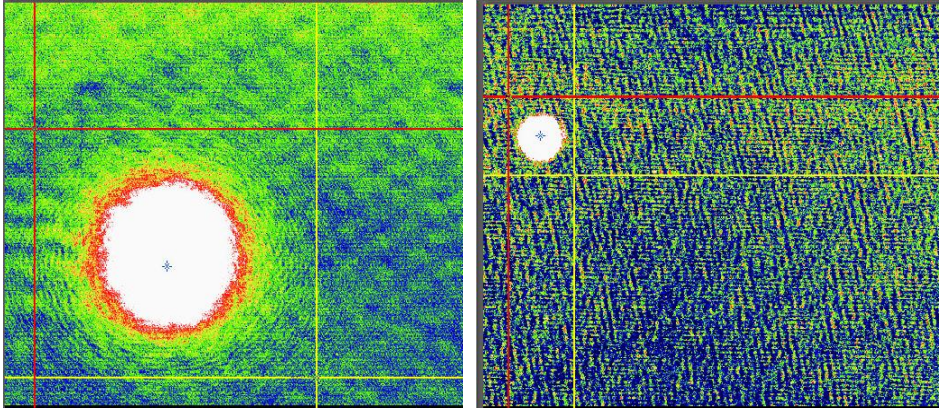


Figure 3.11: BEC imaged with $10.9\times$ magnification (left) and $3.3\times$ (right). The resolution is measured for the $10.9\times$ system by fitting an Airy function to the intensity distribution collected after imaging a transmission grating (bottom). The result is $\approx 4\mu\text{m}$.

3.4.3 Dual state imaging, adiabatic passage

The imaging laser uses the cycling transition $5^2S_{1/2}(F_g = 2) \rightarrow 5^2P_{3/2}(F_e = 3)$, but we produce the condensate in $|F = 1, m_F = -1\rangle$. To be imaged, the atoms need to be transferred to the $F = 2$ manifold. This can be done by applying the repumper laser just before imaging the cloud. However the atoms will be scattered across all the $F = 2$ sub-levels and the recoil and heating associated with the absorption of photons from the repumper beam will affect the image. Additionally, when imaging 2CBEC, since both components have almost the same magnetic moment, they cannot be spatially separated using a Stern-Gerlach technique. Another way of achieving the transfer relies on adiabatic passage [88]. This technique makes use of the adiabatic theorem and the two-level crossing problem [89, 90]. The two-level crossing problem deals with the transition probability between two dressed states $|+\rangle, |-\rangle$ in the presence of a time dependent detuning that passes through zero. Far away from resonance the dressed states coincide with the bare states and the energy difference is big (see figure 3.12). Approaching the resonance the energy difference decreases and if the detuning is swept too quickly it is possible to end up with a superposition of states. The key result is the Landau-Zener probability

$$P_{LZ} = e^{-2\pi\Gamma_{LZ}} \quad \Gamma_{LZ} = \frac{\Omega^2}{4\lambda} \quad \lambda = \left| \frac{d\Delta}{dt} \right| \quad (3.49)$$

that directly links the transition probability P_{LZ} with the rate of change in the detuning λ . In the experiment the detuning is controlled by the magnetic field variation caused by the decay of current in the coils after switching off the current. The MW frequency is kept constant and chosen to be resonant with one of the three sub-levels $|F = 2, m_F = -2, m_F = -1, m_F = 0\rangle$ allowed by single photon transition selection rules. It is applied for 2 ms, 5.7 ms after the current has been switched off. The duration and the time of application has been experimentally found to optimize the transfer efficiency. We can transfer atoms from $|F = 1, m = -1\rangle$ to the desired final state with an efficiency up to 99% (the efficiency differs slightly between transitions due to the different amplitude of the three polarization).

Atoms adiabatically transferred from $|F = 1, m_F = -1\rangle$ receive a kick in the opposite direction (or no kick at all) when subjected to a Stern-Gerlach sequence when compared to atoms in $|F = 2, m_F = +1\rangle$ allowing for spatial separation of the two components and simultaneous dual-state imaging of 2CBEC. Furthermore there is no heating of the cloud and no blur associated with photon emission and recoil. Experimental data showing the efficiency of the transfer for different durations of a π polarized microwave pulse and the width of the resonance are shown in figure 3.13. The resonant frequency can be shifted by delaying the application of the microwave pulse, which is equivalent, given the fact that the magnetic field is sweeping, to a change in the relative energy of the two states coupled by the pulse (see figure 3.13). This was particularly relevant for the experiments where the FSW-0010 microwave synthesizer was used; in fact we had trouble setting a reliable frequency jump between the optimal microwave frequency used during the experiment and the optimal frequency for the adiabatic passage, forcing use to find the condition when both frequency are equal.

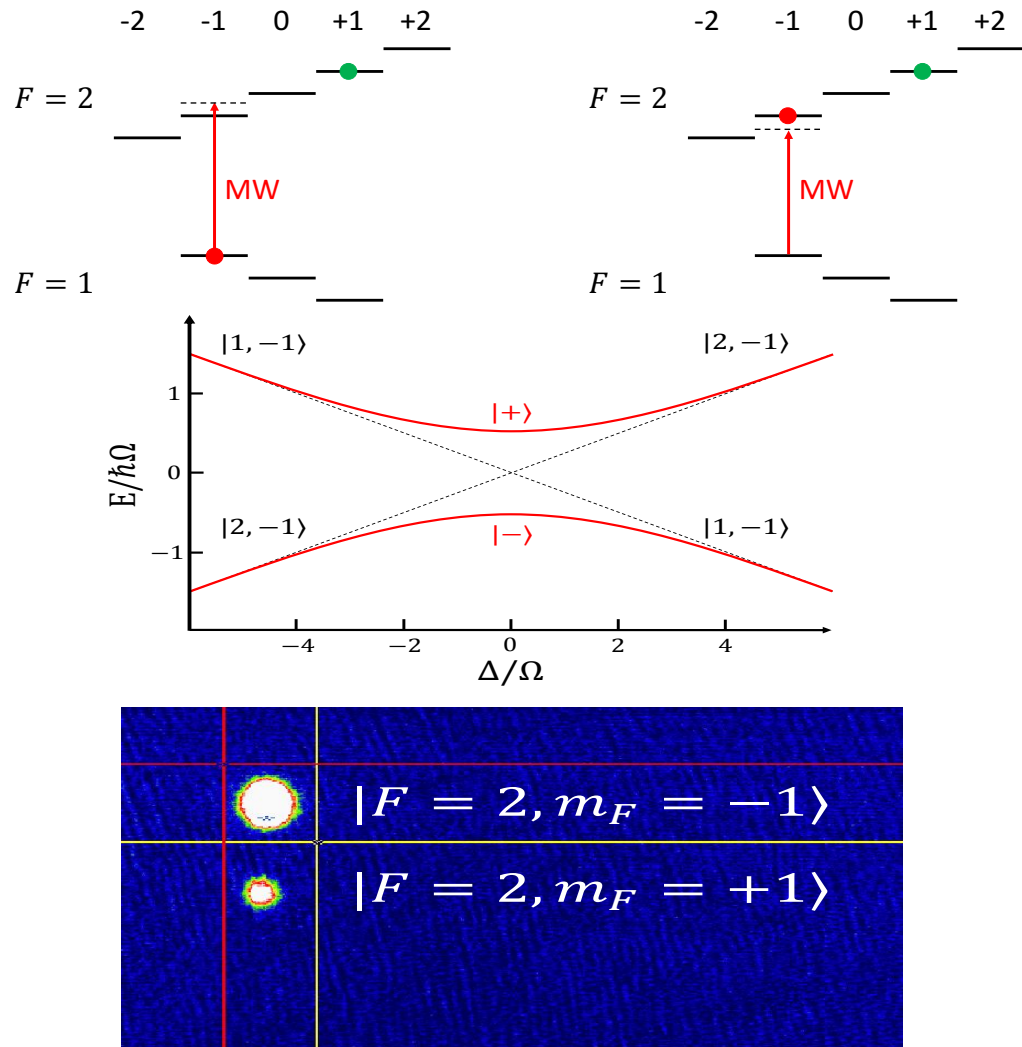


Figure 3.12: Adiabatic passage technique. The MW frequency is kept constant while the magnetic field is swept through the resonance connecting $|F = 1, m_F = -1\rangle$ to $|F = 2, m_F = -1\rangle$, from a positive to a negative detuning (**top**). Satisfying the condition for adiabatic transfer, equation (3.49), guarantees that the population is transferred almost completely (**center**). Each state is then separated using a Stern-Gerlach kick and imaged simultaneously (**bottom**).

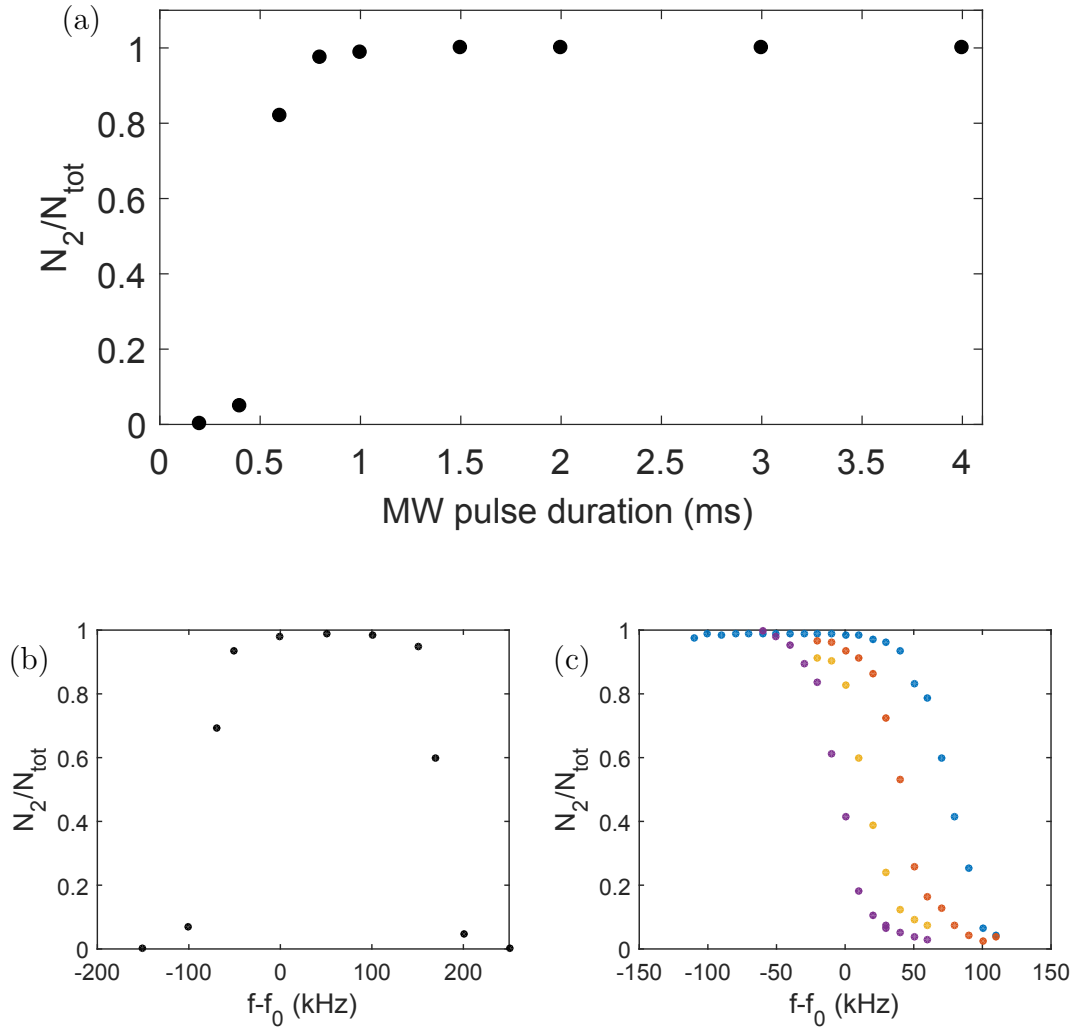


Figure 3.13: **(a)** Adiabatic population transfer from $|F = 1, m_F = -1\rangle$ to $|F = 2, m_F = -1\rangle$ as a function of the duration of the MW pulse. After ≈ 1 ms the transfer efficiency is around 99%. **(b)** Transfer efficiency as a function of MW detuning, with $f_0 = 6.8302$ GHz. The transfer is robust against detuning, having a width of about 200 kHz. **(c)** The frequency of the magnetic field resonant with the transition can be changed by changing the waiting time between the beginning of the magnetic field ramp and the microwave pulse. Blue points are measured after 1.2 ms waiting, red points after 1.3 ms, yellow points after 1.4 ms and purple points after 1.5 ms.

CHAPTER 4

Quantum Noise

In this chapter we introduce the Bloch sphere, a useful tool for visualizing the dynamics of a 2 level system. A description of Ramsey interferometry, a central technique in most of our experiments, is provided in terms of Bloch vector evolution. The final part of the chapter is devoted to an analysis of the major contribution of phase noise, whose understanding is central to our experiments. A distinction is made between quantum, mean field and technical factors affecting phase noise and a description is provided for some relevant cases.

4.1 The Bloch sphere

The Bloch sphere formalism is a very convenient way of visualizing the dynamics of a two level system. It is particularly powerful when used to describe Ramsey interferometry, a technique often used in our BEC interferometry experiments. The Bloch vector formalism is most easily derived for the case of a spin 1/2 system in a magnetic field, but can be easily extended to include any two level system, most notably a spinor condensate, coupled by electromagnetic radiation. The Hamiltonian describing the interaction of a spin 1/2 particle with magnetic moment $\hat{\boldsymbol{\mu}} = -\gamma\hat{\boldsymbol{S}}$,

where γ is the gyromagnetic ratio and $\hat{\mathbf{S}}$ is the spin operator, with a magnetic field \mathbf{B} is

$$\hat{H}_B = -\hat{\boldsymbol{\mu}} \cdot \mathbf{B} \quad (4.1)$$

By choosing as basis the states that have a well defined spin projection along the z-axis, we can write [91] the spin operator $\hat{\mathbf{S}} = \hbar/2\boldsymbol{\sigma}$, where $\boldsymbol{\sigma} = [\sigma_x, \sigma_y, \sigma_z]$ is the vector of Pauli-spin matrices. The density matrix for such a spin 1/2 system is a 2×2 matrix that can be written as

$$\rho = \frac{1}{2}(\mathbb{1} + \mathbf{P} \cdot \boldsymbol{\sigma}) = \frac{1}{2} \begin{pmatrix} 1 + P_z & P_x - iP_y \\ P_x + iP_y & 1 - P_z \end{pmatrix} \quad (4.2)$$

where $\mathbf{P} = (P_x, P_y, P_z)$ is the Bloch vector with component defined by the expectation values of the spin operator through [92]

$$\langle \hat{S}_i \rangle = \frac{\hbar}{2} P_i \quad (4.3)$$

as can be readily seen by remembering that the Pauli spin-matrices are traceless. The length of the transverse component of the Bloch vector is a measure of the coherence

$$\sqrt{S_x^2 + S_y^2} = \frac{\hbar}{2} \sqrt{P_x^2 + P_y^2} = \hbar |\rho_{12}| \quad (4.4)$$

while the length of the longitudinal component represents the difference of the populations in the two spin states

$$S_z = \frac{\hbar}{2} P_z = \frac{\hbar}{2} (\rho_{11} - \rho_{22}) \quad (4.5)$$

The Bloch vector lies on the Bloch sphere (figure 4.1) only for pure states, since $|\mathbf{P}| = 1$, while for maximally mixed states the Bloch vector magnitude is equal to zero. The equation of motion for the density matrix is given by the von Neumann equation [93]

$$i\hbar \frac{\partial}{\partial t} \rho = [H, \rho] + \mathcal{L}\rho \quad (4.6)$$

where \mathcal{L} is the Liouvillian operator taking into account decay. The decay of P_z represents the relaxation of the system to the lowest energy configuration while the decay of P_x and P_y represents decoherence. The most common source of decoherence is entanglement with an inaccessible state, such as a heat bath. Decoherence shortens the magnitude of the Bloch vector. It is worth noting that both these processes are negligible in our experiment. The superposition of states we create remains coherent throughout the experiment since interaction with an external reservoir is minimal and relaxation happens on much longer time scale than the one used in the experiments due to the long lifetime of the state used. What we mean by decoherence in this chapter is the spreading of the Bloch vector representing a many particle system, not its reduction in magnitude. This spread reduces the averaged magnitude of the total Bloch vector in a given direction, while keeping the magnitude of each individual vector constant. As already mentioned the Bloch sphere can be used to represent any state of a two-level system. Starting from a general two level state

$$|\psi\rangle = \alpha|1\rangle + \beta|2\rangle \quad (4.7)$$

where α and β are complex numbers and remembering the normalization condition

$$|\alpha|^2 + |\beta|^2 = 1 \quad (4.8)$$

we arrive, after switching to polar coordinates and considering symmetries, at the form

$$|\psi\rangle = \cos\left(\frac{\theta}{2}\right)|1\rangle + e^{i\phi}\sin\left(\frac{\theta}{2}\right)|2\rangle \quad (4.9)$$

Any two-component superposition can be written by choosing $\theta \in [0, \pi)$, $\phi \in [0, 2\pi)$, representing coordinates on the Bloch sphere with Bloch vector

$$\mathbf{P} = \begin{pmatrix} \cos(\phi)\sin(\theta) \\ \sin(\phi)\sin(\theta) \\ \cos(\theta) \end{pmatrix} \quad (4.10)$$

However there is some ambiguity in the representation of two-level states with Bloch vectors, which has the mathematical justification that rotations in a 2D complex vector space contain a double representation of rotation in 3D real space. As a consequence state $|\psi\rangle$ and state $-|\psi\rangle$ have the same Bloch vector. The polar angle θ describes the population imbalance between the two states, while ϕ represents the relative phase. If we consider the specific case of a two level system coupled by electromagnetic radiation we have the Hamiltonian

$$H = \frac{\hbar}{2} \begin{pmatrix} \Delta & \Omega e^{-i\phi} \\ \Omega e^{i\phi} & -\Delta \end{pmatrix} \quad (4.11)$$

and we can see that, in the case of strong coupling ($\Omega \gg \Delta$), $\theta = \Omega t$, where Ω is the Rabi frequency, ϕ is the phase of the pulse and $d\phi/dt = \Delta$.

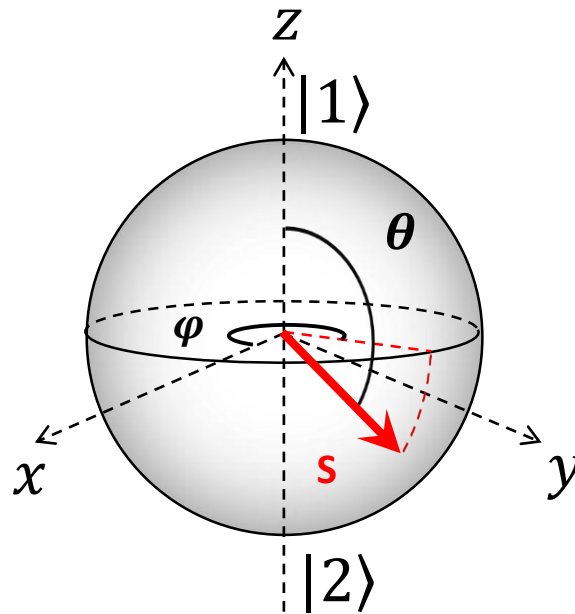


Figure 4.1: Bloch sphere and Bloch vector S representing a superposition of state $|1\rangle$ and $|2\rangle$ characterized by the angles θ and ϕ .

4.1.1 Ramsey interferometry

Ramsey interferometry [94] is the technique we use in experiments to study the evolution of the relative phase of a thermal cloud or two-component BEC. The Ramsey sequence starts with a $\theta = \pi/2$ MW+RF pulse that creates a 50:50 superposition of atoms in the two hyperfine states $|F = 1, m = -1\rangle$, $|F = 2, m = +1\rangle$ and rotates the Bloch vector from the north pole to the equatorial plane (figure 4.2). After an evolution time t a second $\pi/2$ pulse is applied with a phase $\delta\phi$ with respect to the first and the relative atom number difference $P_z = (N_2 - N_1)/(N_2 + N_1)$ is measured. N_1 and N_2 are the numbers of atoms in state $|F = 1, m = -1\rangle$ and $|F = 2, m = +1\rangle$, respectively. For a BEC we can express P_z as

$$P_z = \text{Im} \left(\frac{\int 2e^{i\delta\phi} \Psi_2^* \Psi_1 d^3\mathbf{r}}{\int \Psi_2^* \Psi_2 + \Psi_1^* \Psi_1 d^3\mathbf{r}} \right) \quad (4.12)$$

and we can obtain Ψ_i with GPE simulations. In the frame rotating with the atomic transition frequency, the evolution operator is

$$U(\theta) = \frac{1}{\sqrt{2}} \begin{pmatrix} \cos\left(\frac{\theta}{2}\right) - i\frac{\Delta}{\Omega_R} \sin\left(\frac{\theta}{2}\right) & -ie^{-i\phi} \frac{\Omega}{\Omega_R} \sin\left(\frac{\theta}{2}\right) \\ -ie^{i\phi} \frac{\Omega}{\Omega_R} \sin\left(\frac{\theta}{2}\right) & \cos\left(\frac{\theta}{2}\right) + i\frac{\Delta}{\Omega_R} \sin\left(\frac{\theta}{2}\right) \end{pmatrix} \quad (4.13)$$

where $\theta = \Omega_R \cdot t$ and $\Omega_R = \sqrt{\Omega^2 + \Delta^2}$. This operator, applied to $|\psi\rangle$, tells us how our state changes with time under the influence of the radiation field. For a $\theta = \pi/2$ pulse we have a 50:50 superposition as mentioned above, while for a $\theta = \pi$ pulse we have an inversion of the populations. Free evolution happens when $\Omega = 0$, leaving only the terms on the main diagonal and causing the state to pick up a phase proportional to the detuning. The Bloch vector representing a Ramsey sequence is

given by

$$P_{\text{Ramsey}} = \begin{pmatrix} \cos(\delta\phi) \cos(\phi - \delta\phi) + \sin(\delta\phi) \\ \sin(\delta\phi) \cos(\phi - \delta\phi) - \cos(\delta\phi) \\ \sin(\phi - \delta\phi) \end{pmatrix} \quad (4.14)$$

where $\phi = \Delta t - \pi/2$ is the phase acquired during free evolution and $\delta\phi$ is the relative phase between the Ramsey pulses. The P_z component of the Bloch vector is proportional to the sine of the relative phase and an interference fringe can be acquired by changing either the evolution time t or the relative phase $\delta\phi$ between the pulses. Throughout this thesis, fringes acquired by changing the evolution time are referred to as "Ramsey interference in time domain", while fringes acquired by changing the relative phase are called "Ramsey interference in phase domain". The amplitude of these fringes is the *visibility* and provides a measure of the coherence of the system. Decoherence leads to a decrease of visibility over time, limiting the duration of a Ramsey interference experiment.

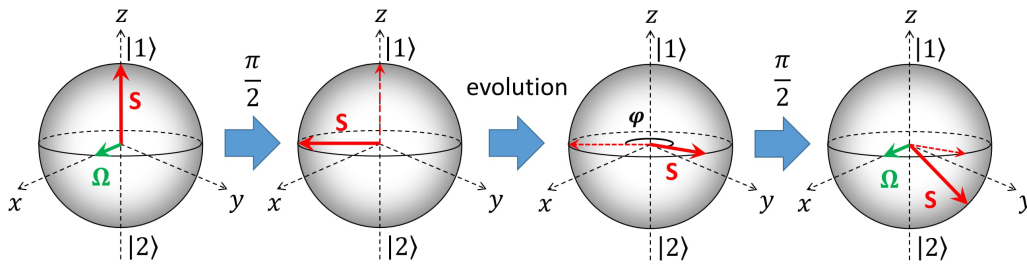


Figure 4.2: Ramsey evolution illustrated on the Bloch sphere. Initially the atoms are all in state $|1\rangle$ and a $\pi/2$ pulse (green arrow) brings the Bloch vector to the equatorial plane. The system will then evolve for a time t , picking up a phase that is read by the second $\pi/2$ pulse. "Reading" has to be interpreted as transforming relative phase into relative population.

4.2 Decoherence factors in a Ramsey sequence

Different factors influence the interferometric contrast of a Ramsey interferometry. These effects can be grouped into four categories:

Quantum effects arise from the full quantum treatment of the condensate and are referred to as *quantum noise*. The most relevant for our experiment are:

- ***The standard quantum limit***, related to the basic quantum principle that a measurement can only provide a probability distribution. It is also called *quantum projection noise*, or shot noise, due to the similarity of the fundamental noise found in lasers.
- ***Quantum phase diffusion*** reduces the visibility over time due to the different evolution of the linear combination of Fock states that form a BEC's coherent state.
- ***Losses***, through the fluctuation-dissipation theorem, force the phase to diffuse over time.

Mean field effects are predicted by the semiclassical CGPE equations. Major mean field effects are:

- ***Collisional shift*** generates a density dependent frequency shift that translates into phase noise.
- ***Collective Oscillations***, caused by the non-stationarity of the superposition of states generated by the first Ramsey pulse. Therefore the wave-function of each component starts to oscillate, trying to minimize the energy, decreasing the overlapping and the visibility.
- ***Inhomogeneous phase growth***. In a superfluid the gradient of the relative phase is related to the relative velocity through

$$\mathbf{v}_i(\mathbf{r}) = \frac{\hbar}{m} \nabla \phi_i(\mathbf{r}). \quad (4.15)$$

the non stationarity of the superposition leads to inhomogeneous phase growth reflecting the different velocities experienced by the components during the evolution

Technical noise from equipment used in the experiment. The most relevant sources are:

- **Local oscillator instability** of the clock synchronizing the MW and RF generators
- **Imaging laser instability** affecting the total number of atom measured
- **MW and RF power fluctuations** modifying the Rabi frequency and creating an imperfect initial split
- **Magnetic noise fluctuation** changing to first order the detuning of the intermediate state in the two photon transition and to second order the detuning between the states, since the experiment is performed in the magic field $B = 3.23$ G. Magnetic noise can also displace the trap.
- **Fluctuation in the current creating the trap** which causes a shift in the position of the trap and consequently influence the effective MW and RF intensity experienced by the atoms.

Finite temperature effects from the interactions with non-condensed atoms.

4.2.1 Standard Quantum Limit

Applying a coherent coupling to a BEC of atoms initially all in the same state $|\Psi_0\rangle = |1, N\rangle$ creates the coherent spin state [95] (figure 4.3)

$$|\alpha\rangle = \sum_{N_1=0}^N \sqrt{\frac{N!}{N_1!N_2!}} c_1^{N_1} c_2^{N_2} |N_1, N_2\rangle \quad (4.16)$$

$$|N_1, N_2\rangle = \frac{(\hat{a}_1^\dagger)^{N_1}}{\sqrt{N_1!}} \frac{(\hat{a}_2^\dagger)^{N_2}}{\sqrt{N_2!}} |0\rangle \quad (4.17)$$

where a_1^\dagger and a_2^\dagger are the creation operators for state 1 and 2 respectively, c_1 and c_2 are complex coefficients and N_1 and $N_2 = N - N_1$ are the expectation values for the atom number in each state. Such a state is akin to the coherent state originally introduced by Glauber [96] in the context of quantum optics and used in laser theory. Coherent states are minimum uncertainty states [97] for which the Heisenberg uncertainty principle reads

$$\Delta\hat{x}^2\Delta\hat{y}^2 = 1 \quad (4.18)$$

$\Delta\hat{x}^2$ and $\Delta\hat{y}^2$ are the variances of two conjugate operators (position and momentum or, as in our case, atom number and phase). The quantum limited uncertainty for a phase measurement is obtained from the Heisenberg uncertainty principle and from the Poissonian variance of the atom number in a coherent state, $\Delta\hat{N}^2 = \langle N \rangle$ and is equal to

$$\Delta\hat{\phi} = \frac{1}{\sqrt{\langle N \rangle}} \quad (4.19)$$

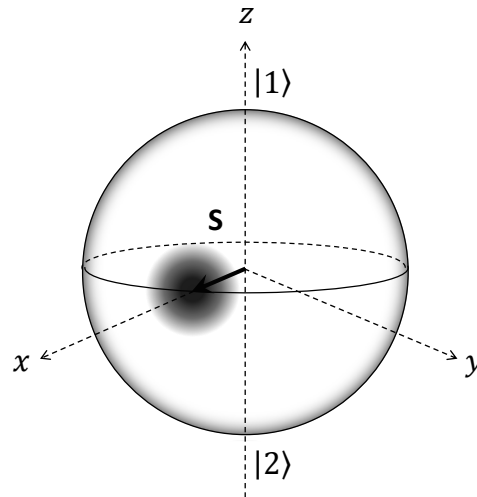


Figure 4.3: Coherent spin state representation on a Bloch sphere. The fuzzy black circle represents the isotropic quantum noise in the $x - y$ plane around the mean spin S , oriented along the x -axis.

4.2.2 Quantum phase diffusion

The initial state for our interferometry experiments is a coherent state that can be written as a superposition of Fock states, equation (4.16). Each Fock state $|N_i, N_j\rangle$ is an eigenstate of the Hamiltonian describing the dynamics of the system. The Hamiltonian is determined by the interactions between the atoms, which in turn depend on the operator $\hat{n}_{i,j}$ that counts the atoms in each number state. From this we can see that each Fock state forming our coherent state evolves in time by picking up a phase proportional to its eigenvalue E_{Fock} which differs from state to state. This leads to a diffusion of the phase in time [98, 99], with consequent reduction of the visibility. This process is called "phase collapse" and happens on a characteristic time scale τ_c , after which the interference contrast is completely lost [29]. However, after some additional time τ_{rev} the individual components re-phase and the interference contrast can be (almost) completely recovered [16]. This effect is called "revival". Quantum phase diffusion can easily be visualized on the Bloch sphere, figure 4.4, where the circularly distributed quantum noise typical of a coherent state is distorted by nonlinear interactions proportional to χS_z^2 into an ellipse of increased phase noise ΔS_y^2 [31].

4.2.3 Losses

The fluctuation-dissipation theorem establishes a link between quantum noise and losses which can be described using a Markovian master equation of the form [99, 100]

$$\frac{d\hat{\rho}}{dt} = -\frac{i}{\hbar}[\hat{H}, \hat{\rho}] + \sum_s \kappa_s \int d\mathbf{r} \mathcal{L}_s[\hat{\rho}] \quad (4.20)$$

where κ_s is a coefficient characterizing the particular loss channel, the summation is performed over the relevant loss channels and $\mathcal{L}_s[\hat{\rho}]$ is a Lindblad operator describing local n-body collisional losses given by

$$\mathcal{L}_s[\hat{\rho}] = 2\hat{O}_s\hat{\rho}\hat{O}_s^\dagger - \hat{O}_s^\dagger\hat{O}_s\hat{\rho} - \hat{\rho}\hat{O}_s^\dagger\hat{O}_s \quad (4.21)$$

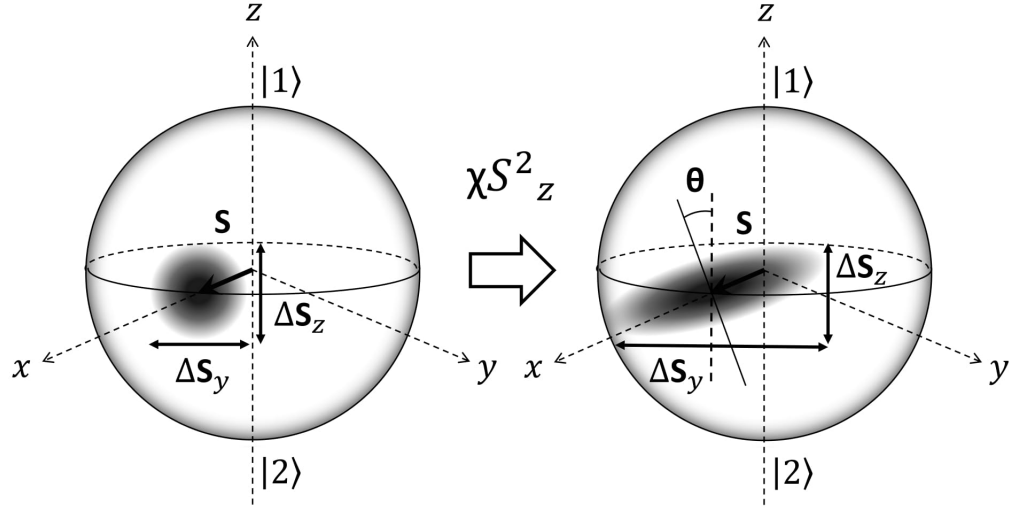


Figure 4.4: Quantum phase diffusion illustrated using the Bloch sphere. A coherent state, with minimum and isotropic uncertainty, gets deformed into an ellipse by interactions. The state is effectively squeezed in the direction θ , but if the squeezed part is not turned to align it with the z -axis, there will be no reduction ΔS_z , only an increase in ΔS_y

with \hat{O}_s reservoir coupling operators given by

$$\hat{O}_s(\hat{\Psi}) = \prod_j \hat{\Psi}_j^s(\mathbf{r}) \quad (4.22)$$

and the product is performed over the quantum state involved in the corresponding loss channel. For the two-component BEC case relevant to our experiment the loss operators are therefore

$$\hat{O}_{111} = \hat{\Psi}_1^3 \quad (\text{three-body losses}) \quad \hat{O}_{22} = \hat{\Psi}_2^2 \quad (\text{two-body losses}) \quad (4.23)$$

$$\hat{O}_{12} = \hat{\Psi}^2 \quad (\text{two-body interspecies losses}) \quad (4.24)$$

In this derivation lost particles don't interact with the BEC. Since particle number must be conserved for massive particles at low energies, lost particles are transferred

to different quantum states which are either expelled from the magnetic trap because they are untrappable or because they have acquired enough kinetic energy in the loss process to escape. The master equation is handled by the theory group at Swinburne by using the Wigner distribution to get a Fokker-Planck equation which in turn is transformed in a system of stochastic differential equations in either Ito or Stratonovich form and solved numerically [101]. Another way of modeling losses is by treating them as quantum jump operators in the interaction picture, with a full mathematical treatment provided in Ref. [43]. Each loss event therefore corresponds to a sudden shift of a coherent state into another coherent state with reduced mean atom number and phase proportional to both the time t_j at which the loss event took place and the mean field interaction experienced by the atoms at t_j . This is because the mean field interaction is equivalent to a detuning that causes the spin vector to precess around the z-axis. Losses randomly remove particles from state $|1\rangle$ or state $|2\rangle$ changing this detuning and causing the states to either lag behind or be boosted forward in their rotation, introducing phase noise, Fig.4.5.

4.2.4 Collisional Shift

For ultracold gas the thermal de Broglie wavelength is greater than the scattering length and interactions between atoms cause an energy shift. This phenomenon is well known in atomic clocks and one of the fundamental reasons limiting their performance. The frequency shift can be written as [28]

$$\Delta\nu_{12} = \frac{2\hbar}{m}(\alpha_{22}a_{22}n_2 + \alpha_{12}a_{12}n_1 - \alpha_{11}a_{11}n_1 - \alpha_{12}a_{12}n_2) \quad (4.25)$$

where α_{ij} is a coefficient which is 2 for non condensed atoms and 1 for a coherently prepared two component BEC, a_{ij} is the scattering length and n_i is the density. From the section on Ramsey interferometry we have seen that the frequency of Ramsey fringes depends on the detuning. The collisional shift is density dependent and for a cloud in an harmonic trap the density distribution can be considered Gaussian in

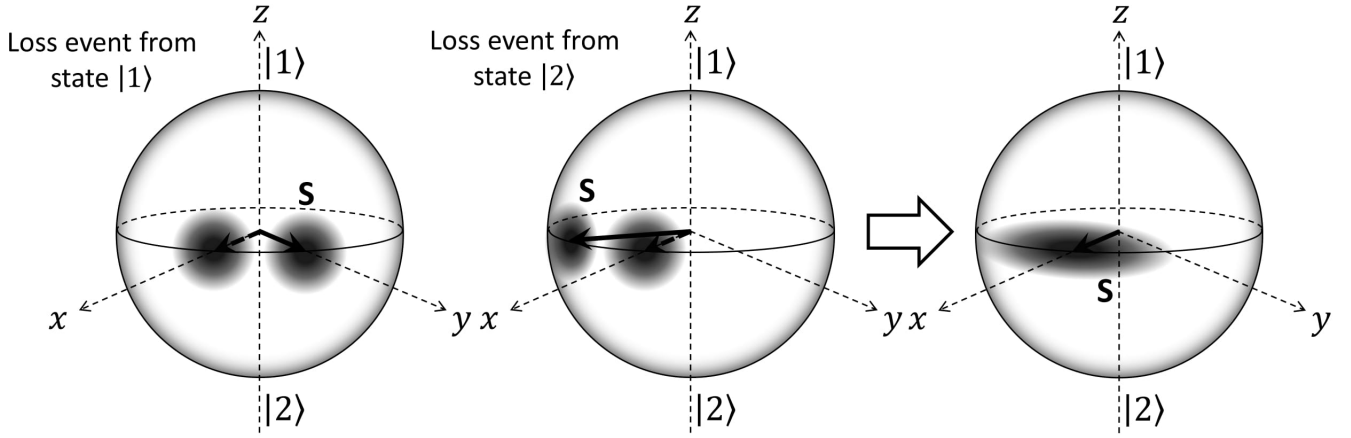


Figure 4.5: Loss induced dephasing. A loss event associated with the removal of particle from state $|1\rangle$ cause the phase to shift clockwise, while losses from state $|2\rangle$ cause a counterclockwise phase shift. Averaging over all stochastic processes leads to dephasing. The loss event are assumed symmetric for the purpose of this representation. The z -projection is thus unaffected by losses.

the case of a thermal cloud or Thomas-Fermi for a BEC. Different part of the cloud will therefore evolve with different frequencies causing decoherence.

4.2.5 Inhomogeneous phase growth

In a superfluid the gradient of the phase is related to the velocity via

$$\mathbf{v}(\mathbf{r}) = \frac{\hbar}{m} \nabla \phi(\mathbf{r}) \quad (4.26)$$

After evaporation a condensate lies in its ground state, which is a stationary state with $\mathbf{v}(\mathbf{r}) = 0$. Hence the phase across the condensate is uniform. The application of the coupling two-photon pulse and the creation of a two-component BEC leaves the system in an excited state with a non-zero relative velocity and consequently a nonuniform relative phase. The components, due to the effect of repulsive interaction, start to oscillate in the trap with a characteristic frequency (for our conditions

$f_c = 3 \text{ Hz}$) with state $|2\rangle$ compressed in the center of the trap and state $|1\rangle$ squeezed to the sides. After a time $\tau_c/2$ the motion is reversed. The superfluidity of the system should imply that this oscillatory motion will develop undamped, but the presence of atomic loss actually dampens the oscillation. These dynamics predominantly take place in the axial direction, due to the high energy required to create an excitation in the radial direction. The motion in the radial direction can thus be considered suppressed and the phase uniform. The relative velocity itself is not constant, but has a complex spatial and time dependence that depends on the details of the motion of each component in the harmonic potential. This time and space dependence of the phase greatly contributes to the decrease in visibility [88]. The oscillatory nature of the motion means that after a full period, and in the absence of other decoherence mechanism (i.e. losses), the interference contrast can be completely recovered (see figure 4.6), giving rise to "revival" of coherence similar to those described in the quantum phase diffusion section, but with a completely different physical justification [102]. Furthermore, the visibility is influenced by the spatial overlap of the wave functions of each component and as we have seen, this imperfect overlap changes with time due to the collective oscillation.

4.2.6 Interaction with a thermal cloud

The interaction of the condensed part of a cloud with the non-condensed (thermal) part has been shown to cause decoherence. Sinatra and Castin have calculated the effect due to finite temperature [103] and have shown that the variance of the relative phase grows in time according to

$$\Delta\phi^2(t) = \Delta\phi_0^2 + A_T t^2 \quad (4.27)$$

where $\Delta\phi_0^2$ is the variance associated with the initial state. A_T is a coefficient that depends on temperature, interaction strength and number of atoms and, in the thermodynamic limit, can be approximated at low temperature ($k_B T \ll ng$)

with [30]

$$A_T \approx \frac{8\pi^4}{15} \frac{a^2 \xi}{V} \left(\frac{k_B T}{\hbar} \right)^2 \left(\frac{k_B T}{ng} \right)^3 \quad (4.28)$$

where $g = 4\pi\hbar^2 a/m$ is the interaction coefficient, n is the BEC density, ξ is the healing length and V is the volume occupied by the condensate. Usually the condensate we create are very pure with negligible thermal fraction for the first 200 ms of evolution. We might therefore neglect finite temperature effects for short evolution times, but the contribution should be taken into account on longer time scales.

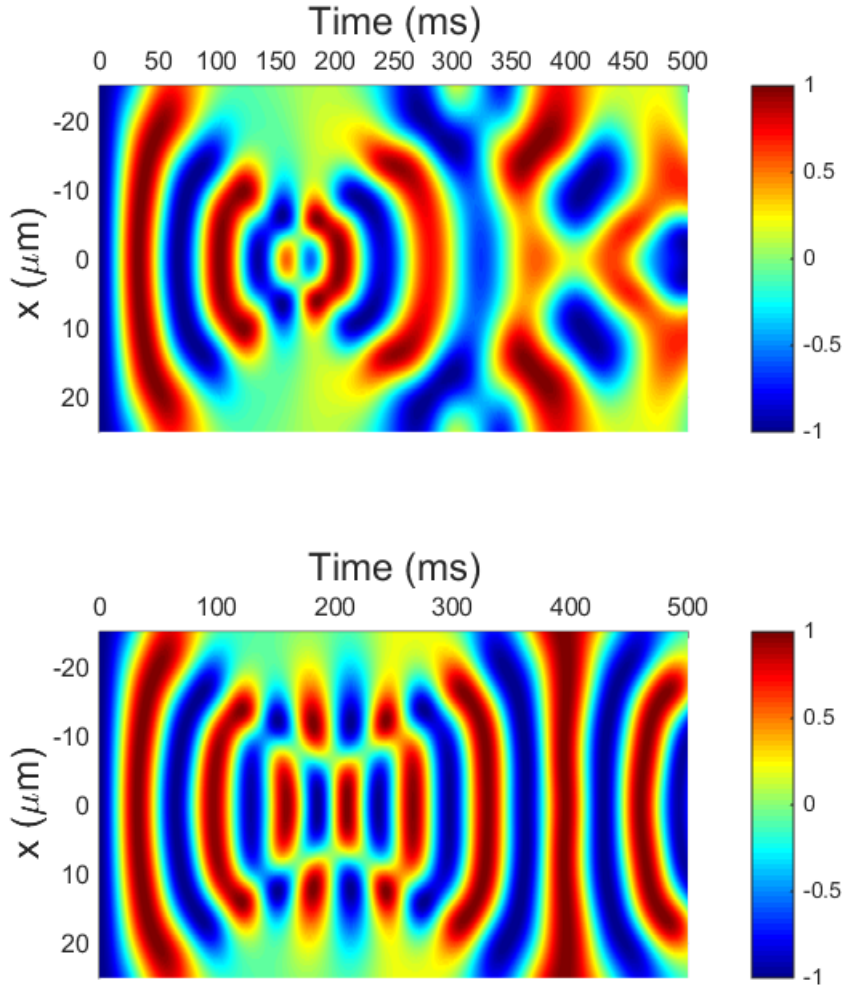


Figure 4.6: Simulated local spin projection $p_z = (n_2 - n_1)/(n_2 + n_1)$ along the axial direction obtained for $N = 5 \cdot 10^4$ atoms and a detuning $\Delta = 2\pi \cdot 15$ Hz in the presence (**top**) and absence (**bottom**) of losses. Equal values of p_z represent identical values of relative phase across the condensate. For the lossy case the visibility is at its peak at the beginning of the evolution, decreases to a minimum after 170 ms, corresponding to the maximum separation between the two components and then increases without ever reaching the original peak value. In the absence of losses visibility is fully recovered after ≈ 350 ms, exhibiting an undamped periodic behavior.

CHAPTER 5

Coherence of thermal clouds and BEC, Experimental results

The macroscopic quantum properties of BECs have been extensively studied in the field of atom interferometry. Interference between condensates, either spatially separated or in different quantum states have been used to perform very accurate measurements and has the potential to be used to create a new generation of high precision sensors. To improve the sensitivity of an interferometric measurement, high particle numbers and long evolution times are important. Atoms, unlike photons, can have strong interactions, leading to decoherence and limiting the timescale of the measurements. Experiments in Swinburne [73,82,102] have achieved coherence time, defined as the time at which the visibility maximum drops by $1/e$, of 1.3 seconds for a Ramsey sequence interferometry and 2.8 seconds for a spin-echo interferometry. Simulation of the phase growth uncertainty [1], figure 5.1, obtained with a truncated Wigner method, allows us to extrapolate a coherence time of 11 seconds when only quantum noise is present. The dominant source of decoherence is thus technical noise, mainly from local oscillator instability. For this reason we have upgraded our system with a new, more stable, MW generator and a state of the art quartz oscillator to synchronize the RF and MW generators used to produce the Ramsey

pulses. In this chapter we provide evidence of the reduction of technical noise to level below the quantum noise and we attempt to measure the coherence time of a BEC of $3 \cdot 10^4$ atoms.

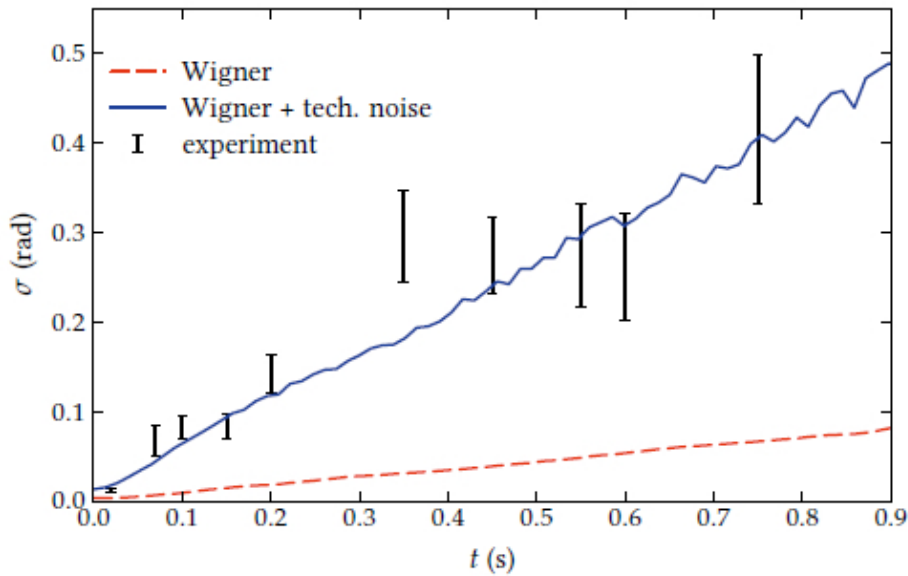


Figure 5.1: Phase uncertainty evolution in a Ramsey interferometry. The black bars represent experimental points. The red dashed line shows the growth of phase uncertainty due to quantum noise simulated using truncated Wigner method. The solid blue line represents the sum of technical and quantum noise. The technical noise clearly dominates over the quantum part. Adapted from Ref. [1]

5.1 Experimental sequence and fringe analysis

In this chapter we will be performing two types of experiments; the first is a phase diffusion experiment using thermal atoms, designed to measure the classical noise from our equipment and the second uses low atom number BEC and a much stabilized setup to try to detect and quantify quantum contribution to the decoherence of the condensate's phase. Honours student Cambell Biggs participated in collecting

measurements on the coherence of thermal clouds.

5.1.1 Phase diffusion experiments

To characterize the level of technical noise in our system we prepare noncondensed, thermal atoms in the state $|1\rangle = |F = 1, m_F = -1\rangle$. We first trap $\sim 5 \cdot 10^8$ atoms in a mirror MOT in 12 s. After the MOT stage, atoms are transferred to a CMOT created by passing a current in U-wire on the atom chip and by applying a bias field. At this point the temperature of the cloud is Doppler limited at about $150 \mu\text{K}$ as measured from time of flight expansion. The cloud is further cooled using polarization gradient cooling. To increase the efficiency of the polarization gradient cooling we decrease the magnetic field to the point it only prevents atoms from falling under gravity and we increase the trapping laser detuning. The result is a cloud with a temperature of $\approx 40 \mu\text{K}$. The atoms are then optically pumped in the selected state $|1\rangle = |F = 1, m_F = -1\rangle$. Approximately $1 \cdot 10^8$ atoms are then transferred to the magnetic trap. We use a magnetic trap with axial frequency $f_{ax} \approx 97.0 \text{ Hz}$ and radial frequency $f_r \approx 11.7 \text{ Hz}$. The trapping frequencies have been measured by applying a small current to one of the end wire on the atom chip, thus slightly displacing the cloud, and then monitoring the dynamics (figure 5.2). To reduce the number of particle from $1 \cdot 10^8$ to a value which varies between 10^5 to $2 \cdot 10^5$ we use an inefficient evaporation process that removes the atoms from the trap without letting them rethermalize, thus preventing condensation. The trap bottom is set to $\approx 3.23 \text{ G}$ to eliminate first order the Zeeman shift and provides first order insensitivity to magnetic field fluctuations. A two-photon MW+RF pulse creates an equal superposition of states $|1\rangle = |F = 1, m_f = -1\rangle$ and $|2\rangle = |F = 2, m_f = +1\rangle$. The length of the $\pi/2$ pulse is 0.7 ms, giving a Rabi frequency $\Omega = 2\pi \cdot 360 \text{ Hz}$. The MW field is detuned by $\approx 2\pi \cdot 1 \text{ MHz}$ from the intermediate, untrappable state $|F = 2, m_f = 0\rangle$ to avoid leakage. The RF is provided to the atoms through one of the end-wires on the chip while the MW is radiated by a dipole antenna

placed outside the vacuum chamber, approximately 12 cm away from the atoms. The second Ramsey interrogation pulse is applied after an evolution time which can be variable when performing time-domain Ramsey interferometry or fixed when the interferometry is in the phase domain. In the phase domain it is the different phase relationship between the pulses, created using a built in function of the MW synthesizer, that generates the Ramsey fringe. After the second pulse the cloud is released and imaged using the adiabatic passage technique described in chapter 3.

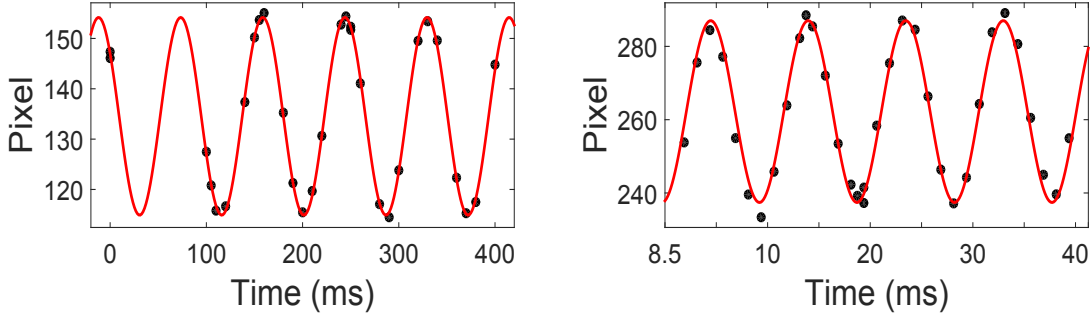


Figure 5.2: Measurements of axial (**left**) and radial (**right**) oscillation frequencies in a magnetic trap with 3.23 G trap bottom. We imparted momentum to the cloud by moving it away from the minimum through the application of a short current pulse in one of the unused end-wires on the surface of the atom chip, displacing it in the axial and radial direction at the same time. The measured values are ≈ 97.0 Hz in the radial direction and ≈ 11.7 Hz in the axial.

The relevant quantity measured in every iteration is the atom number difference $P_z = (N_2 - N_1)/(N_1 + N_2)$. For analyzing the data we use the simplified fitting function

$$P_z(N, t, \Delta, \phi) = \mathcal{V}(N, t) \sin(\Delta t + \phi_{mf} + \phi_{mw}) \quad (5.1)$$

where \mathcal{V} is the visibility, Δ is the effective detuning of the two-photon drive, ϕ_{mf} is the mean field driven relative phase, and ϕ_{mw} is the MW phase shift between Ramsey pulses. For thermal atoms the mean field contribution is approximately linear in the total particle number N and we rely solely on measurements to estimate it.

Fluctuations in the atom number cause corresponding fluctuations in the value of ϕ_{mf} which appear as phase noise and can lead to apparent phase collapse. The knowledge of the relation between atom number and accumulated phase allows us to correct for fluctuations and achieve good interferometric contrast on timescales otherwise inaccessible. The time dependence of the mean field driven relative phase ϕ_{mf} implies that corrections are more precise for Ramsey interferometry in phase domain, where the evolution time is kept constant. In the time domain we could acquire the atom number dependence for each point of a Ramsey fringe, but such a procedure is time consuming.

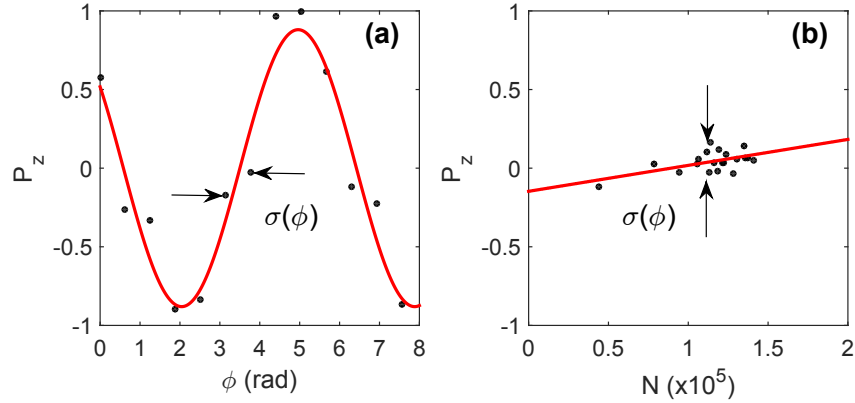


Figure 5.3: Ramsey interferometry of a thermal cloud in phase domain after 500 ms of evolution **(a)** and zero-crossing experiment at 500 ms **(b)**. The fitted function of the zero-crossing experiment is used to correct the points on the Ramsey fringe for atom number fluctuations. The fringe fit error gives the phase STD $\sigma(\phi)$. The phase standard deviation can also be extracted from the zero-crossing data after correction. Both measurements are significant for the correct recovery of the uncertainty of the phase .

The correction for atom number variations is performed in a "zero-crossing" experiment. We first determine the value of the phase or the evolution time for which $P_z \approx 0$ and then we collect 10 to 20 points in this conditions. The zero-crossing is chosen because the sensitivity of the phase to the variations in the atom number is

maximal. The experimental points collected in zero-crossing experiments are fitted with a linear function, the slope is extracted from the fit and the value obtained by multiplying the slope by the total number of atoms measured for each point is subtracted to the measured value of P_z , thus correcting for atom number fluctuations. The visibility \mathcal{V} is defined as the amplitude of the sinusoidal fit, equation (5.5). The fitting function takes into account phase noise by introducing an exponentially decreasing visibility \mathcal{V} . If we assume the noise from all technical sources to be Gaussian distributed, which is acceptable for the central limit theorem, then the visibility decreases according to

$$\mathcal{V} = \int_{-\infty}^{+\infty} \sin \phi \frac{1}{\sqrt{2\pi\sigma^2}} e^{-\frac{\phi^2}{2\sigma^2}} = e^{-\frac{\sigma^2}{2}} \quad (5.2)$$

where σ is the standard deviation obtained from the fit standard error. The phase standard deviation can be obtained from a "zero-crossing" experiment as well, using the equation

$$\phi(P_z) = \arcsin \left(\frac{P_z}{\mathcal{V}} \right) \quad (5.3)$$

and defining $\sigma = \text{STD}(\phi(P_z))$. However, knowledge of the visibility is required and a phase or time domain Ramsey sequence must be performed. From an operational point of view, the extraction of phase uncertainty from a zero-crossing experiment follows the idea that in the absence of all sources of noise the points acquired must have the same value of $P_z = 0$. Noise of all kinds displaces the points around $P_z = 0$. Atom number fluctuations can be corrected as mentioned above either through simulations or through fit in the case of thermal atoms. The remaining phase spread is defined as phase standard deviation σ .

5.1.2 Quantum Decoherence of BEC experiments

For quantum decoherence experiments, the sequence is similar to the one described in section 5.1.1 with the main difference that, to produce BEC, the evaporation trajectory is optimized. The result is a pure condensate with the total atom number

controllable from a minimum of $1.5 \cdot 10^4$ to a maximum of 10^5 . The observable measured is again the normalized atom number difference $P_z = (N_2 - N_1)/(N_1 + N_2)$. In a Ramsey sequence for a 2CBEC the atom number difference evolves as [82]

$$P_z(N, t, \Delta, \phi) = \frac{2}{N} \text{Im} \left[e^{i(\phi + \Delta t)} \int \Psi_2^* \Psi_1 d^3 \mathbf{r} \right] \quad (5.4)$$

depending on atom number N , time t , detuning Δ and MW phase ϕ of the second Ramsey pulse and overlap between the two wavefunction Ψ_1 and Ψ_2 . Such a dependence is complex and requires the solution of coupled Gross-Pitaevskii equations. We can again use a simplified fitting function of the form

$$P_z(N, t, \Delta, \phi) = \mathcal{V}(N, t) \sin(\Delta t + \phi_{mf} + \phi) \quad (5.5)$$

and the agreement is good in phase domain for any evolution time, while in time domain the agreement is good below 200ms (see figure 5.4).

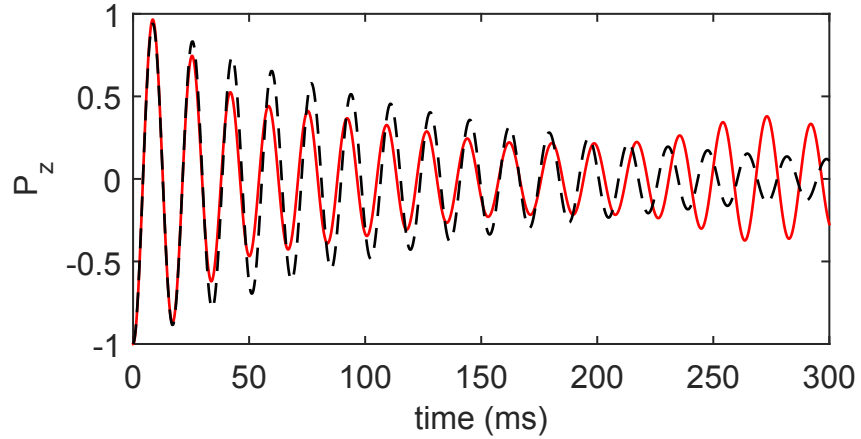


Figure 5.4: Comparison between CGPE simulation including particle loss of a Ramsey experiment with $N = 1.5 \cdot 10^5$ atoms, detuning $\Delta = 2\pi \cdot 40$ Hz (red solid line) and the fitting function equation (5.5) (black dashed line). The analytical function agrees well with the numerically calculated values within 200 ms. Notice the revival starting at 240 ms which the simplified fitting model is unable to predict.

For a condensate the mean field phase ϕ_{mf} is not linear anymore in N , but follows

the relationship given by [102]

$$\phi_{mf} = \alpha(t)N^{2/5}t \quad (5.6)$$

where N is the number of atoms and $\alpha(t)$ is a time dependent coefficient which can be measured or derived from simulations. The coefficient $\alpha(t)$ changes slowly with time, allowing us to correct data in a 20 ms range using the same phase dependence and introducing only a negligible error.

5.2 Phase diffusion, results

The results of previous experiments performed in Swinburne [73, 82, 102] (see figure 5.1) have shown that the dominant source of phase diffusion comes from technical noise, most prominently phase instabilities in the MW generator and in the local oscillator used to synchronize the MW and RF. We have switched from the Agilent E8527D MW synthesizer originally used in the experiment performed by Egorov [102] in 2011 to a more stable QuickSyn MW synthesizer FSW-0010 (Fig. 3.8, chapter 3). The local oscillator used in previous experiments was the internal clock of the Agilent E8257D. We have replaced it with an oven controlled crystal oscillator OCXO 8607 made by Oscilloquartz. The experiments are performed using thermal atoms to reduce the density dependent mean-field effects and achieve longer coherence time. This in turn allows us to better isolate the contribution to phase noise introduced by the different pieces of equipment used. Due to the absence of collective oscillations and inhomogeneous phase growth [88], typical of superfluid systems, the dephasing is slower and quantum dephasing [43] effects have negligible effects due to the high particle numbers. Furthermore losses, a major source of dephasing, are greatly suppressed by the reduced density.

5.2.1 Phase diffusion with Agilent E8257D

As a starting point we decided to characterize the old setup used by Egorov [82]. This will serve as a benchmark for comparison with the new configuration. The Ramsey interferometry is performed in the phase domain, with the MW phase ϕ of the second $\pi/2$ pulse chosen to vary in a range from 0 to 2π .

The Rabi frequency of the two-photon coupling is set to $\Omega = 2\pi \cdot 700$ Hz, the same value as used in the original experiment [82]. The detuning is different, being $\Delta = 2\pi \cdot 20$ Hz, compared to $\Delta = 2\pi \cdot 37$ Hz previously used. The particle number is markedly higher, ranging from $2 \cdot 10^5$ to $4 \cdot 10^5$ compared to the $4 \cdot 10^4$ to $7 \cdot 10^4$ obtained in 2011. Trap bottom is set to 3.23 G, giving a Zeeman splitting of ≈ 2.26 MHz. The MW frequency is 6.8314 GHz, while the RF frequency is 3.248 MHz, making the intermediate state $|F = 2, m_F = 0\rangle$ detuned by about 1 MHz. Data are collected after $t_1 = 100$ ms and $t_2 = 500$ ms.

Figure 5.5 shows the results obtained from the experiments. The fitted visibility at 100 ms is $\mathcal{V} = 0.95$ and decreases to $\mathcal{V} = 0.8$ at 500 ms. The phase diffusion is estimated in two ways: the first estimation is obtained by calculating the standard deviation of the experimental points (corrected for atom number fluctuations) from the sinusoidal fit, equation (5.5). The second estimation is based on the standard deviation of the linear fit from the zero-crossing experiment, as shown in figure 5.3. At 100 ms the value obtained from the fringe fitting STD is 0.0573 rad, very close to 0.0576 rad obtained from the zero-crossing. At 500 ms the uncertainty on the phase is 0.2739 rad from the fitting STD and 0.2749 rad from the zero-crossing. The phase uncertainty growth rate is 0.51 rad/s, a value remarkably similar to the 0.50(8) rad/s previously measured. Furthermore, we recovered the linear time dependence of the phase diffusion of noncondensed atoms already observed by Ivannikov in his work on atom clock stability [73].

We then installed the OCXO 8607 oven controlled crystal oscillator by directly connecting it to the reference input of the Agilent MW synthesizer, causing the

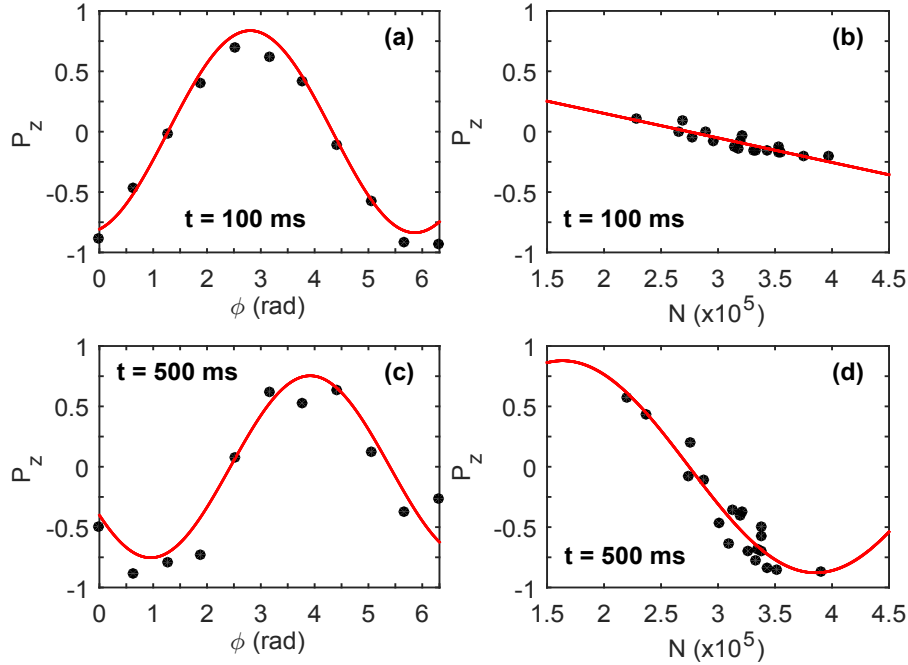


Figure 5.5: Ramsey interferometry in phase domain **(a,c)** and zero-crossing experiment **(b,d)** performed with Agilent E8257D and internal clock synchronization. Black dots are experimental data points, the red solid line in **(a,c)** is a sinusoidal fit using equation (5.5), **(b)** is a linear fit while **(d)** is a sinusoidal fit due to the fact that the experiment has not been performed exactly at the zero-crossing.)

generator to lock to the clock signal. We acquired an additional set of points at evolution time $t_1 = 100$ ms, $t_2 = 300$ ms and $t_1 = 500$ ms, displayed in figure 5.6. The measurements shows a reduction of the phase growth rate from 0.51 rad/sec to 0.4 rad/sec, a 20% decrease that we attribute to the higher stability of the local oscillator. Table 5.1 provides the experimental findings for the two different configurations.

Agilent E8257D synchronized by internal clock			
Time (ms)	Visibility \mathcal{V}	$\sigma(\phi)$ from fit (rad)	$\sigma(\phi)$ zero-crossing (rad)
100	0.95	0.057	0.058
500	0.8	0.274	0.275
Phase uncertainty growth rate = 0.51 rad/sec			
Agilent E8257D synchronized by OCXO			
Time (ms)	Visibility \mathcal{V}	$\sigma(\phi)$ from fit (rad)	$\sigma(\phi)$ zero-crossing (rad)
100	0.95	0.03	0.043
300	0.82	0.114	0.115
500	0.78	0.198	0.201
Phase uncertainty growth rate = 0.4 rad/sec			

Table 5.1: Summary of the visibility and phase standard deviation measured in the phase diffusion experiment with Agilent E8257D MW synthesizer.

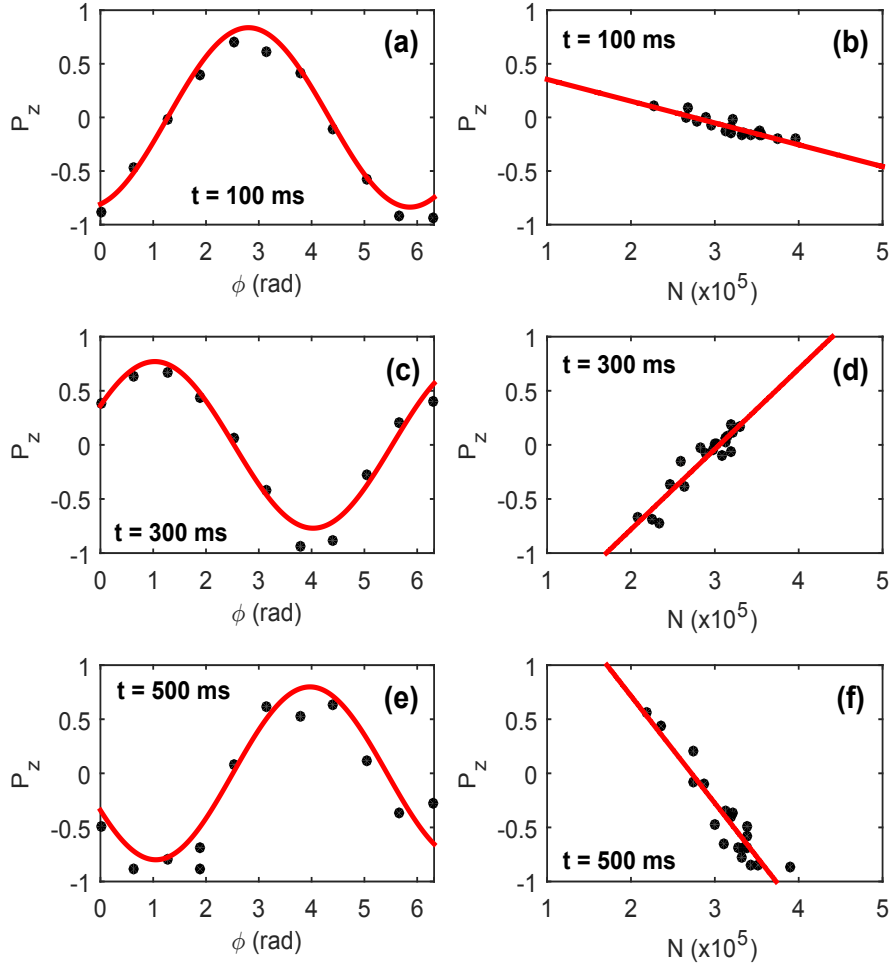


Figure 5.6: Ramsey interferometry in the phase domain **(a,c,e)** and zero-crossing experiment **(b,d,f)** performed with Agilent E8257D and OCXO 8607 crystal oscillator. Black dots are experimental data points, the red solid line in **(a,c,e)** is a sinusoidal fit using equation (5.5) and in **(b,d,f)** is a linear fit.

5.2.2 Phase diffusion with QuickSyn MW synthesizer

To test the QuickSyn MW generator we performed a series of Ramsey interferometry experiments in time domain. The time domain was somehow forced upon us by the fact that the synthesizer could not be triggered to change the phase of the second

$\pi/2$ pulse. Time domain is inherently easier to implement experimentally, since the MW generator continuously produces a signal that is fed to the atoms when the MW switch is triggered. No trigger is required for the MW generator. The results of the experiment are presented in Figure 5.7 while the relevant quantity measured can be found in Table 5.2.

QuickSyn synchronized by OCXO			
Time (ms)	Visibility \mathcal{V}	$\sigma(\phi)$ from fit (rad)	$\sigma(\phi)$ zero-crossing (rad)
100	0.91	0.003	0.01
500	0.72	0.08	0.07
700	0.72	0.058	0.06
1000	0.6	0.09	0.11
Phase uncertainty growth rate = 0.11 rad/sec			

Table 5.2: Summary of the visibility and phase standard deviation measured in the phase diffusion experiment with QuickSyn MW synthesizer and OCXO local oscillator.

It is immediately evident there is a drop by $\approx 80\%$ in the phase diffusion growth rate when compared with the previously used setup, from 0.51 rad/sec to 0.11 rad/sec. Figure 5.8 offers a summary of the phase noise measured for all the experiments performed and a comparison to the quantum phase noise simulated with a truncated Wigner approach for a BEC of $5 \cdot 10^4$ atoms [102]. Such quantum noise shouldn't

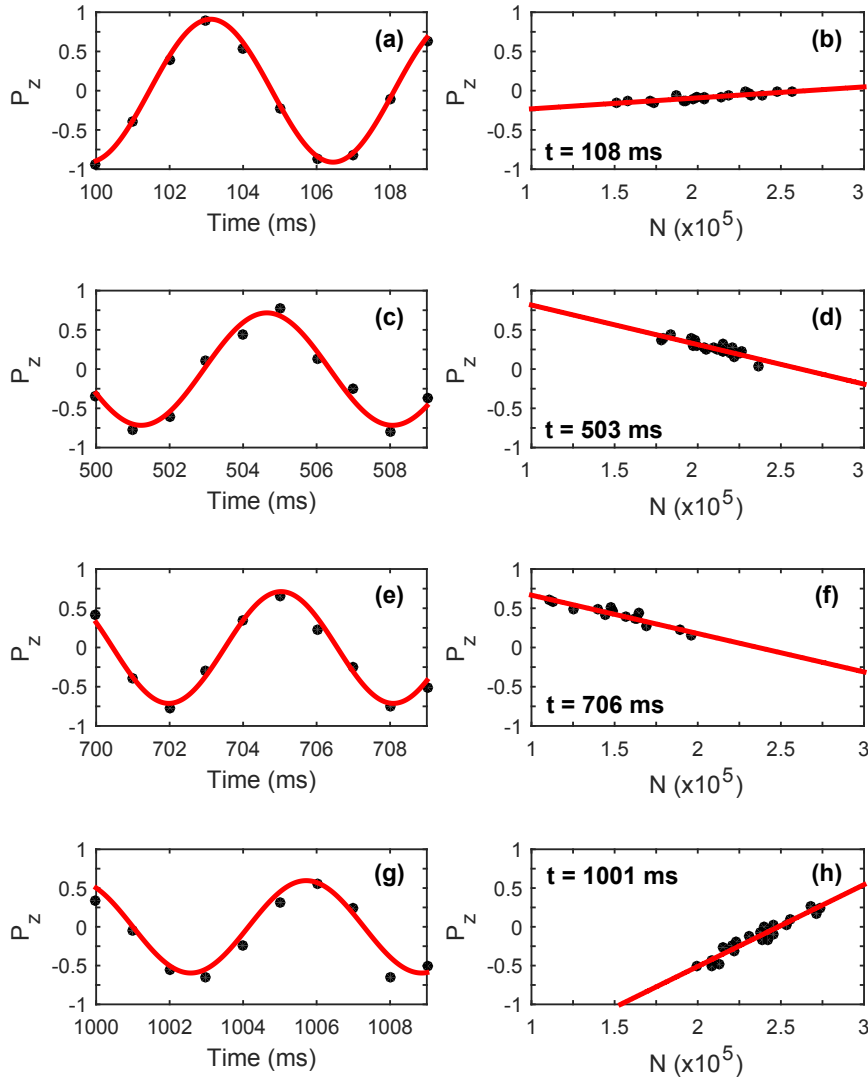


Figure 5.7: Ramsey interferometry fringes in time domain **(a,c,e,g)** and zero-crossing experiment performed at $t = 108$ ms **(b)**, $t = 503$ ms **(d)**, $t = 706$ ms **(f)**, $t = 1001$ ms **(h)** with QuickSyn MW generator and OCXO local oscillator. The evolution time is chosen to match the $P_z = 0$ condition. The points in the zero-crossing experiments follows an almost ideal linear dependence over a broad range of atom number, while the sinusoidal fit is excellent for all times considered, indication of very low phase instability.

be considered indicative of the actual quantum noise present in the current set of experiments. Since we are dealing with thermal atoms and with atom numbers between $2 \cdot 10^5$ and $4 \cdot 10^5$ the real quantum noise in the experiment would necessarily be smaller. Nevertheless it is possible to see how the improvement in the setup has reduced the technical contribution to the phase growth to a level comparable, if not smaller than the quantum noise in a BEC (Cf. with figure 5.1) . This will be relevant in the other set of experiments performed in this chapter, for the estimation of the coherence time of a BEC and the quantum phase noise measurements.

The linear dependence of the phase uncertainty on time, previously reported in other Ramsey interferometry experiments for both thermal clouds and BEC [73,82], is confirmed by the current observations. The error bars represents the statistical uncertainty on $\sigma(\phi)$ and are calculated as $\Delta\sigma(\phi) = \sigma(\phi)/\sqrt{M}$, where M is the number of experimental realizations for each data point, ranging from M=20 to M=30.

We can define an amplitude coherence time τ_{amp} at which the visibility drops by $1/e$. The value, obtained from the exponential fit of the visibility decrease in figure 5.9 is

$$\tau_{amp} = 11.5 \text{ s} \quad (5.7)$$

The phase coherence time τ_{coh} , defined as the time at which the phase becomes random, can be obtained from equation (5.2) by defining $\sigma(\phi) = \beta \cdot t$, where β is the phase diffusion growth rate, observed to be linear in time. In other words, we define the coherence time τ_{coh} as the time at which $\sigma(\phi) = \sqrt{2}$. The calculated value for a Ramsey sequence with QuickSyn synthesizer is

$$\tau_{coh} = 12.9 \text{ s} \quad (5.8)$$

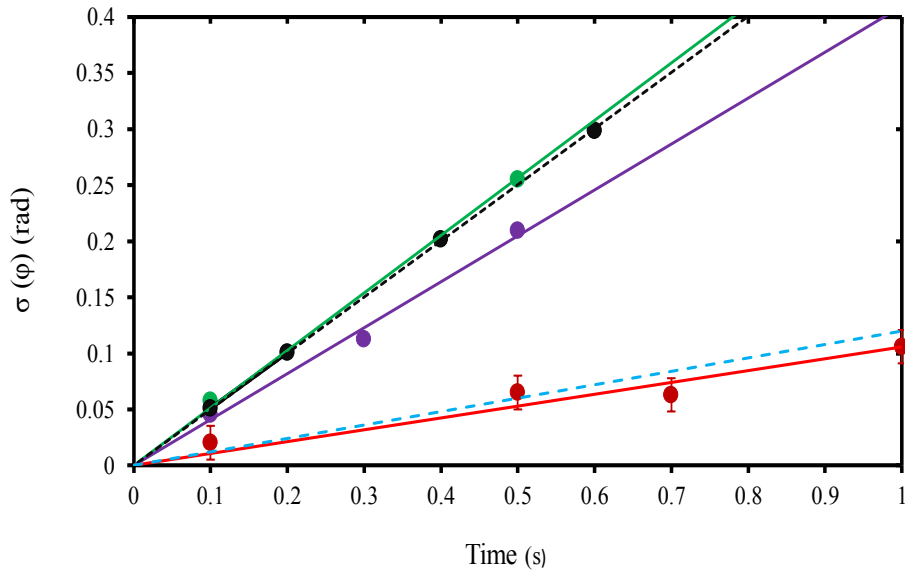


Figure 5.8: Phase diffusion growth rate for a Ramsey interferometry with thermal atoms. The experimental points obtained using QuickSyn MW generator and OCXO local oscillator (**red dots**), Agilent E8257D and OCXO (**purple dots**), Agilent E8257D and internal clock 2015 (**green dots**) and Agilent E8257D and internal clock [102] (**black dots**) are displayed. The lines are linear fits for these points, except the blue dashed line that represents quantum noise simulated with truncated Wigner method for a BEC of $5 \cdot 10^4$ atoms. The phase noise measured with QuickSyn MW generator and OCXO lies below quantum noise.

5.2.3 Inhomogeneous dephasing and identical spin rotation effect

In this section we will calculate the contribution to the decoherence due to inhomogeneous dephasing. Inhomogeneous dephasing occurs because trapped atoms experience an inhomogeneous shift $\Delta(r)$ of the transition frequency due to combined contributions of the trapping potential and atomic interactions. Since different atoms explore different regions, they experience different frequency shifts and therefore their spins precess at different speeds, therefore causing dephasing at a

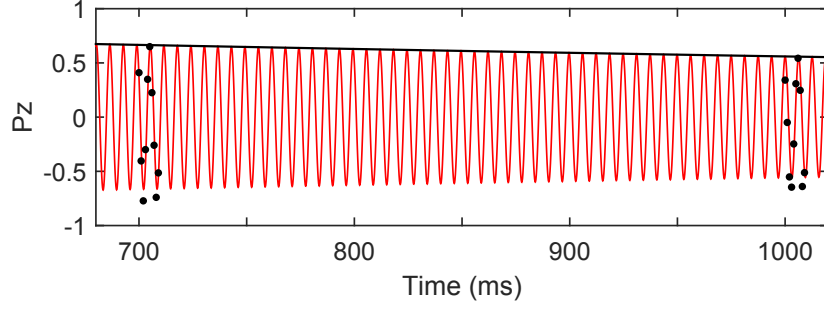


Figure 5.9: Ramsey interferometry for long evolution times. The black line is an exponential envelope modeling the visibility decay, the red line is a sinusoidal fit almost perfectly following the experimental points (**black dots**). The frequency of a Ramsey fringe is $f_{\text{ramsey}} = 100.2$ Hz. From the exponential envelope an amplitude coherence time of 11.53 s is extracted.

rate characterized by an average inhomogeneity Δ_0 give by [33, 84, 104]

$$\Delta_0/2\pi = \frac{2\sqrt{2}\hbar}{m}(a_{11} - a_{22})\bar{n} \quad (5.9)$$

where \bar{n} is the average density. The average density can be estimated, assuming normal distribution of n , from the peak density using $\bar{n} = n_{\text{peak}}/8$, and the peak density can be estimated from the total atom number, the trap frequencies and the temperature with [49]

$$n_{\text{peak}} = \frac{N}{(2\pi)^{3/2}\sigma_r^2\sigma_z} \quad \sigma_i^2 = \frac{k_B T}{m\omega_i^2} \quad (5.10)$$

Typical values of the temperature T in our experiment range from 250 to 350 nK, while $N \approx 10^5$, $\omega_z = 2\pi \cdot 11.7$ Hz and $\omega_r = 2\pi \cdot 97$ Hz. These values give a $n_{\text{peak}} \approx 1.5 \cdot 10^{12}$ atom/cm³ and consequently a $\bar{n} \approx 0.5 \cdot 10^{12}$ atom/cm³. From this we get $\Delta_0 \approx 2\pi \cdot 0.2$ Hz and we can extract the coherence time, in a way similar to equation 5.2, by setting $\sigma = \Delta_0 t$

$$\mathcal{V} = e^{-\Delta_0^2 t^2/2} = e^{-t^2/\tau_0^2} \quad (5.11)$$

leading to

$$\tau_0 = \frac{\sqrt{2}}{\Delta_0} \approx 1.1 \text{ s} \quad (5.12)$$

Such a short coherence time comes as a surprise, but it is important to note that we are in a regime where the identical spin rotation effect (ISRE) [33, 105, 106] occurs. The identical spin rotation effect can be explained by dividing the atoms in two classes having different spin precession rates around the z-axis: the fast and the slow class. An atom is placed in the fast or slow class based on the average detuning experienced. Due to the different precession rates the two classes start to dephase. The ISRE cause the two spin polarizations to rotate around their sum, allowing the slow class to switch place with the fast class. The two polarizations, now swapped, continue to precess at the same speed, thus leading to rephasing. It is important to note that the ISRE does not change the sum of the polarization which will stay on the equatorial plane for an equal superposition. The ISRE will occur with the frequency

$$\omega_{ISRE}/2\pi = 2\hbar|a_{12}|\bar{n}/m \approx 4 \text{ Hz} \quad (5.13)$$

which is larger than Δ_0 and the lateral elastic collision rate

$$\gamma_c = \frac{32\sqrt{\pi}}{3}a_{12}^2\bar{n}v_T \quad (5.14)$$

where $v_T = \sqrt{k_B T/m}$, is much smaller than ω_{ISRE} and the trap frequencies. The ISRE effect is responsible for a dramatic increase in coherence time. A remark should be made on the fact that an additional source of loss of contrast is due to asymmetric losses that remove atoms predominantly from state $|2\rangle$. For this reason estimates of the coherence time solely based on the contrast drop do not completely describe the coherence property of the ensemble, and zero-crossing measurements based on the spread are a nice complement.

5.2.4 Other sources of technical noise

Instability of the local oscillator and shot to shot fluctuations of the microwave and radio frequency generator's phase are not the only sources of technical noise. For this reason we will briefly describe other effects that affect phase uncertainty.

Imperfect preparation pulse

Fluctuations in the MW or RF power cause corresponding fluctuations in the AC Stark shift, with slightly different Rabi frequencies Ω . This in turn will not lead to a perfect $\pi/2$ pulse and the Bloch vector will not lie on the equatorial plane. Fluctuations in the magnetic fields change the detuning of the MW field from the intermediate level of the two-photon transition to first order, causing the similar effects. The variance of P_z can be calculated using [107]

$$\sigma(P_z)^2 = \left(\frac{\Omega}{2} \frac{dP_z}{d\Omega}\right)^2 \left(\frac{\delta P}{P}\right)^2 + \left(\frac{dP_z}{d\Delta}\right)^2 (\delta\Delta)^2 \quad (5.15)$$

where Ω is the two-photon Rabi frequency, δP are the fluctuations in MW power, $\delta\Delta$ are the fluctuations in detuning Δ and P_z can be expressed in terms of Δ and Ω as

$$P_z = \alpha^2 + (1 - \alpha^2) \sin(|\Delta|T + \epsilon) \quad (5.16)$$

with

$$\alpha = \frac{(|\Delta|/\Omega)^2 + \cos(\Omega\sqrt{1 + (|\Delta|/\Omega)^2})}{(|\Delta|/\Omega)^2 + 1} \quad (5.17)$$

$$\epsilon = \tan^{-1} \left(\frac{[1 + 2(|\Delta|/\Omega)^2] \cos(\Omega\sqrt{1 + (|\Delta|/\Omega)^2} \cdot t) + 1}{2|\Delta|/\Omega \sqrt{1 + (|\Delta|/\Omega)^2} \sin(\Omega\sqrt{1 + (|\Delta|/\Omega)^2} \cdot t)} \right) \quad (5.18)$$

In Figure 5.10 we can see a set of points showing the stability of a preparation pulse of length 0.7 ms, Rabi frequency $\Omega = 2\pi \cdot 360$ Hz, intermediate detuning $\Delta \approx 2\pi \cdot 1$ MHz. The preparation pulse is stable within 1.6%. Measurements on the magnetic field performed with a FluxGate magnetometer show fluctuation of the magnetic field in the 15 mG range. This accounts for $\approx 1\%$ of the uncertainty in P_z , with the remaining 0.6% due to power fluctuations. The uncertainty in relative population translates into frequency uncertainty through the collisional shift

$$\Delta\nu_{12} = \frac{2\hbar}{m} n(2a_{12} - a_{11} - a_{22})\sigma(P_z) \quad (5.19)$$

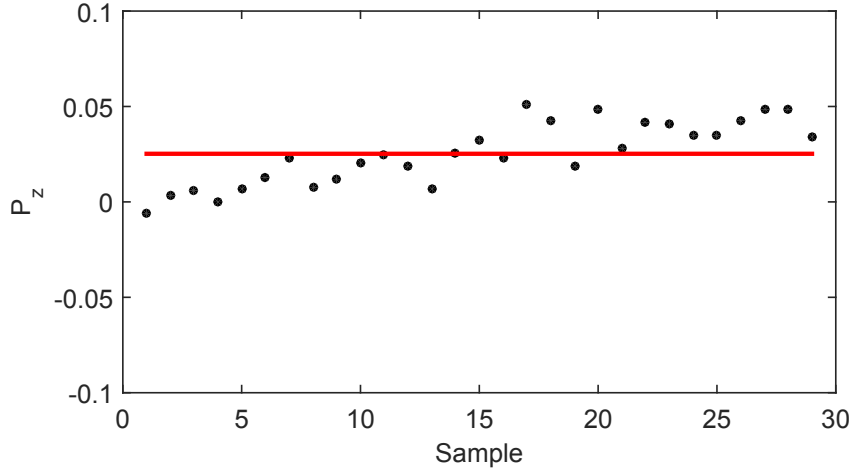


Figure 5.10: Preparation pulse uncertainty for a two-photon transition at 3.23 G with QuickSyn MW synthesizer. The standard deviation is $\sigma(P_z) = 0.016$. The red line represents the average, $\langle P_z \rangle = 0.025$. The upward trend has already been observed in Allan deviation measurements performed at Swinburne by Ivannikov et al. The source has been identified in random walk frequency noise [73]

where n is the peak atomic density, typically $\approx 2 \cdot 10^{12} \text{ cm}^{-3}$ and $\sigma(P_z) = 0.016$ from previous considerations. After substitution in equation (5.19) we obtain $\Delta\nu_{12} = -0.34 \text{ mHz}$ and a contribution to the phase uncertainty growth of 0.002 rad/s .

Imaging noise

The relevant informations extracted in the experiment are obtained from absorption imaging. In the experiment we collect two consecutive images on a CCD camera, one containing the shadow cast by the atoms and the other in the absence of them. The two images are then subtracted and the atom number per pixel follows the formula [107]

$$N_{px} = c_0 \left(L \ln \frac{e_i}{e_f} + \frac{e_i - e_f}{e_{sat}} \right) \quad (5.20)$$

where $c_0 = 2\pi P^2/(3\lambda^2 M^2)$, P is the pixel area, M is the magnification, e_{sat} is the electron count corresponding to $I_{sat} = 1.67 \text{ mW cm}^{-2}$, $L = (4\Delta^2 + \Gamma^2)/\Gamma^2$ which depends on the detuning and the natural linewidth of the transition used for imaging and $e_{i,f}$ are the electron counts per pixel for the first and second image, respectively. The electron counts per pixel depends on the intensity of the incident laser light through

$$e_{i,f} = \frac{\eta P \tau I_{i,f}}{\hbar \omega} \quad (5.21)$$

where η is the quantum efficiency of the CCD camera, τ is the exposure time and $\hbar \omega$ is the energy per photon. The intensity of a laser is not constant, but follows a Poissonian distribution. Consequently the detected atom number will fluctuate with an uncertainty [107]

$$\sigma(N) = c_0 \sqrt{\sum_{px} \left[e_f \left(\frac{1}{e_{sat}} + \frac{L}{e_f} \right)^2 + e_i \left(\frac{1}{e_{sat}} + \frac{L}{e_i} \right)^2 \right]} \quad (5.22)$$

and the summation is performed over all the pixels. Egorov has characterized this uncertainty [82] and found that it accounts for 2% of the measured atom number. The corresponding frequency shift is

$$\Delta\nu_{12} = \frac{2\hbar}{m} n(a_{22} - a_{11})\sigma(N) \quad (5.23)$$

which gives a contribution of -15 mHz and leads to a phase growth of 0.09 rad/sec. From this consideration it seems that with the new MW synthesizer the phase diffusion is mostly due to imaging laser shot noise.

5.3 Quantum decoherence of a BEC

In the previous section we have demonstrated the reduction of the phase diffusion from 0.51 rad/s to 0.11 rad/s. Using the new MW generator this value is below the quantum phase growth for a BEC of $\approx 5.5 \cdot 10^4$ atoms. We perform Ramsey interferometry experiments with pure condensates with a nearly absent thermal fraction. This makes decoherence through interaction with a thermal cloud a negligible

process. The particle number is kept low, below $\approx 3 \cdot 10^4$ atoms, half of the value used in previous experiments in Swinburne [102], further increasing the contribution of quantum noise to phase diffusion when compared with the simulations in figure 5.1 (quantum contributions to the phase uncertainty scale as $1/\sqrt{N}$). Reduction of the number of atoms has the additional benefit of minimizing the density dependent mean field contributions, making data correction easier. The aim is to observe an increased coherence time when compared to 1.3 seconds previously obtained and to characterize the effect of quantum noise sources on phase diffusion.

5.3.1 Ramsey interferometry with BEC

This set of experiments follows the same procedure and is performed in the same conditions as those with thermal atoms. The only difference lies in the fact that we are preparing between $1 \cdot 10^4$ and $4 \cdot 10^4$ condensed atoms, with negligible thermal fraction. Information on visibility and phase diffusion are obtained by directly comparing the results of GPE equations to our data points or through fitting with the simplified function

$$P_z(N, t, \Delta, \phi) = \mathcal{V}(N, t) \sin(\Delta t + \alpha(t)N^{2/5}t + \phi) \quad (5.24)$$

where $\alpha(t)N^{2/5}t$ is the mean field contribution to the phase. The coefficient $\alpha(t)$ is estimated by fitting equation (5.24) to points obtained with GPE simulation of a 50/50 Ramsey sequence at different times and for different total atom number N , keeping only α as a free parameter. Figure 5.11 shows such a fit and we can see that the fitting function, equation 5.24, closely follows the simulations, with some discrepancy for $8 \cdot 10^4$ at 100 ms, but we do not have that many particles in the experiment. In the range $1 \cdot 10^4$ to $4 \cdot 10^4$ the matching is almost perfect. The detuning in the simulation is set at $\Delta = 0$. $\alpha(t)$ is slowly varying with time and for $t = 20$ ms we have $\alpha = 0.75$, at $t = 100$ ms α increases to 0.91 and then grows very slowly with $\alpha = 1.04$ at 400 ms. The knowledge of $\alpha(t)$ allows us to correct for atom number fluctuations in the same way we did for thermal atoms.

While running experiments with BEC we were plagued by technical problems whose origin is not completely understood. As can be seen from figure 5.12 and 5.13 the experimental points follow the simulations very well for the first 50 ms, but after that the points start to depart from the expected behavior and become highly randomized around 100 ms. The experimental data only get worst at longer evolution times, where the data points have a random distribution in atom number in zero-crossing experiments (figure 5.14) and at 400 ms the visibility is only 0.2, while from GPE simulations it should be 0.7, since it is very close to the maximum of the revival, which happens after a full period of collective oscillations, 0.39 s for the present experiment.

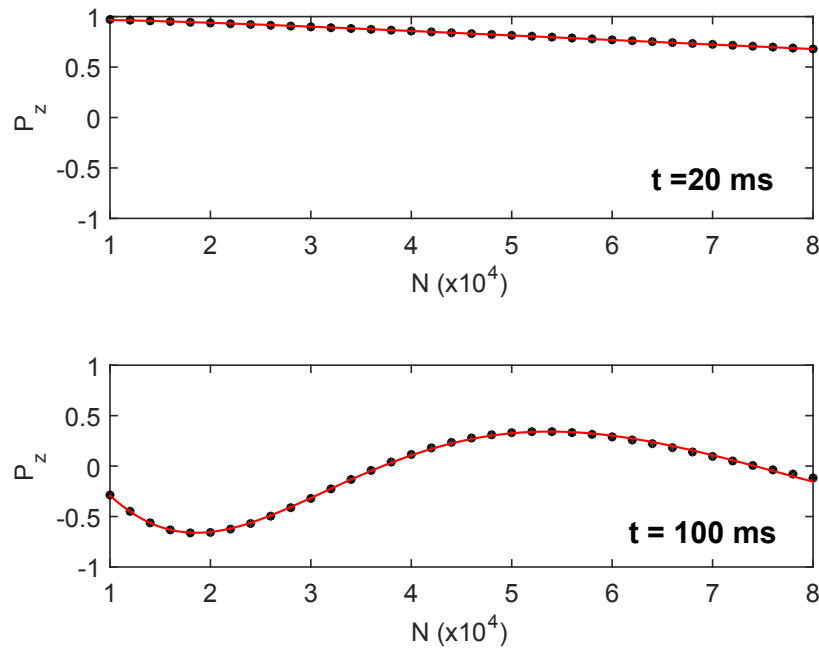


Figure 5.11: GPE simulations including losses of Ramsey sequences with variable atom number for (**top**) 20 ms and (**bottom**) 100 ms evolution time. The red line is a fit to the simulated points using equation (5.24).

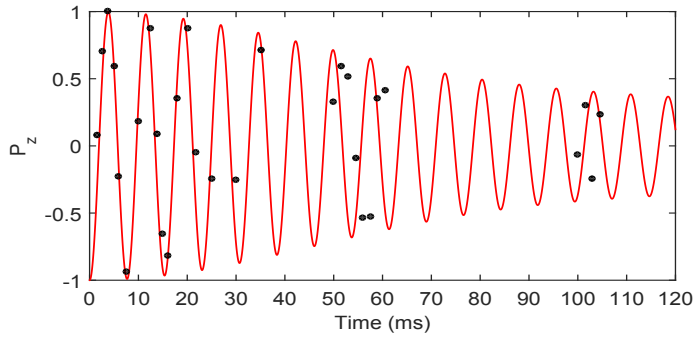


Figure 5.12: Ramsey evolution in time domain for a BEC. The black dots are experimental points corrected for atom number fluctuations and the red line is a GPE simulation for $\Delta = 120$ Hz and $N = 3 \cdot 10^4$ atoms. The points follow the simulation almost perfectly until 50 ms, where they start to deviate.

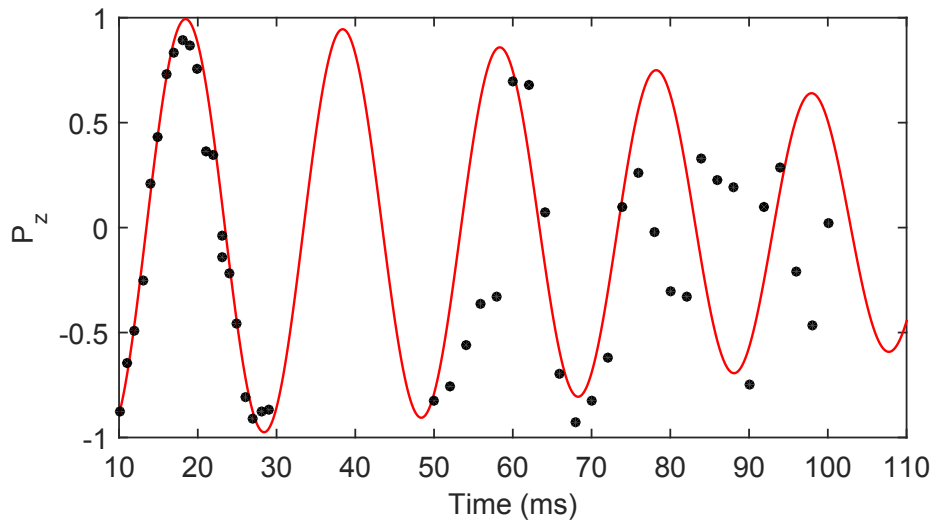


Figure 5.13: Ramsey interferometry in time domain fitted with the simplified fitting function, equation (5.24) (red line). The detuning is $\Delta = 46$ Hz and points are corrected for fluctuations in atom number. The same trend as in figure 5.12 is visible, with the points deviating around $t = 50$ ms and becoming randomized around $t = 100$ ms.

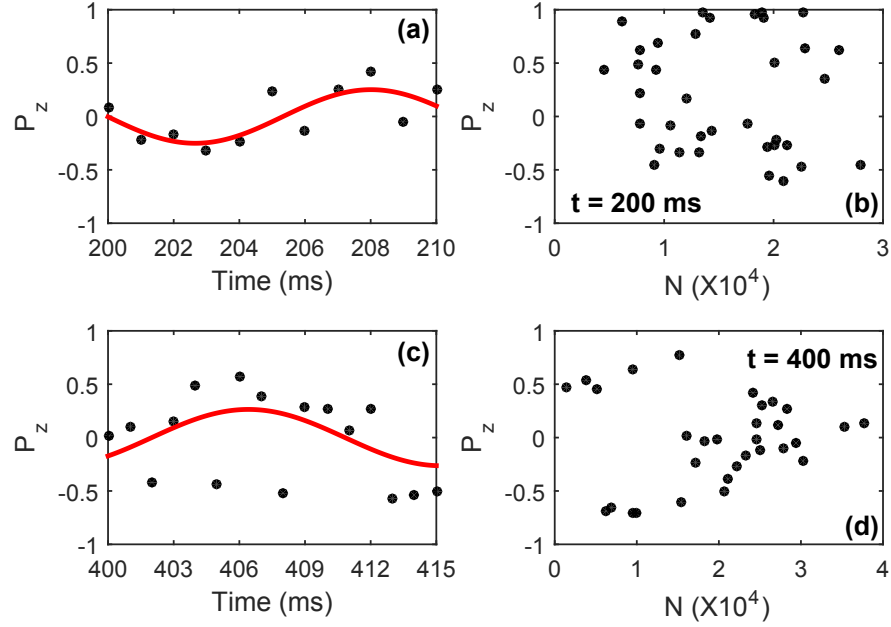


Figure 5.14: Ramsey interferometry in time domain (**a,c**) and zero crossing experiments in the atom number domain (**b,d**) with condensed atoms. The visibility in (**a**) is 0.3, matching the predicted visibility in GPE simulation since 180 ms correspond to the maximum separation of the clouds under collective motion and maximally non-uniform relative phase (see chapter 4, section 4.2.5). In (**c**) the visibility is only 0.2, much less than the expected 0.7 and the sinusoidal fit is very poor, clear sign of rapid dephasing. The points in the zero-crossing experiments are highly randomized, preventing fitting.

The most likely cause of instability in our system is related to the fact that the MW synthesizer and the RF generator, which are both directly connected to the local oscillator, cannot reliably lock on its signal. They stay locked for a while, and then they randomly jump to a different phase. This can be inferred from figure 5.15 where points were taken consecutively in a zero-crossing experiment with BEC at 100 ms. It can be seen that the points follow an almost straight line, expected after correction, and then they suddenly jump to a different value of P_z while retaining a

similar slope.

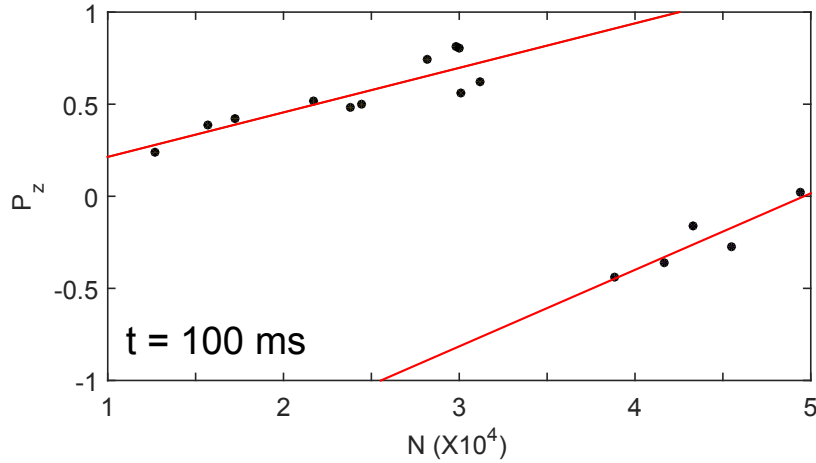


Figure 5.15: Zero-crossing experiment in the atom number domain showing a sudden phase jump. The inability of the generators to lock on the local oscillator might be a possible explanation for the quick dephasing rate experienced in the BEC experiments.

In order to isolate the origin of the problem we have performed phase diffusion experiment with thermal atoms and different combinations of MW synthesizer and local oscillator. The results are summarized in figure 5.16 and show an increase in phase growth rate of ≈ 2.7 times compared to our original setup, independent of the particular MW generator, RF generator or local oscillator used. This is rather disconcerting, because it points in the direction of something shared by all the configurations, which can be the MW amplifier or the MW switch, with the additional complication that the problem might lie in the way trigger pulses are generated (Labview control software) or distributed (National Instrument board). The current state of the system makes further progress impossible and the investigation of this issue is of primary importance.

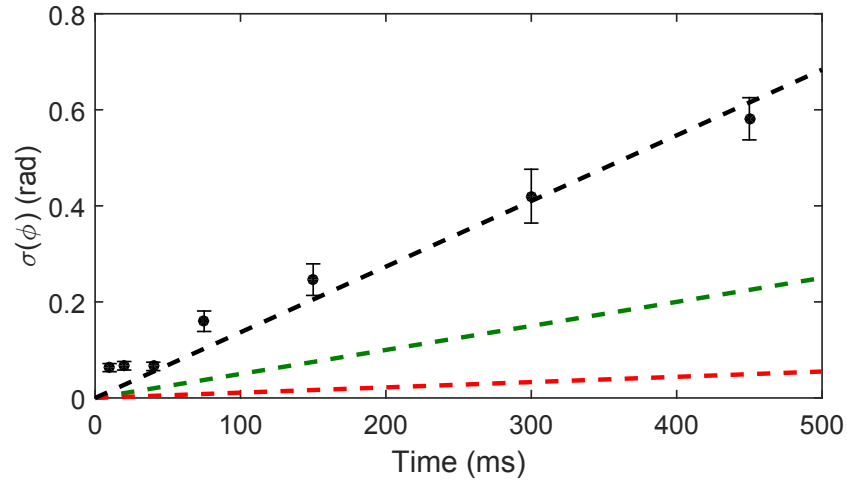


Figure 5.16: Phase evolution with thermal cloud in the current state of the system. The linear fit for the points (**black dashed line**) gives a phase diffusion growth rate of 1.36 rad/s, 2.7 times the original setup (**green dashed line**) and 12.4 times the improved setup (**red dashed line**). Furthermore there is a constant phase spread at small evolution times, absent in the previous measurements.

5.4 Conclusion

In this chapter we initially described the improved a setup that reduces technical noise below the quantum limit previously estimated by Egorov et al [102]. The coherence time of a thermal cloud in a Ramsey interferometer has been extended to 12 seconds. Then we moved to measure the quantum contribution to phase diffusion in BEC, but we were hampered by a technical problem that caused our system to decohere three times faster than observed with the old, non improved setup. The explanation for such poor performance still eludes us, even though we have performed extensive testing on all the components that could be isolated. Unfortunately the setup is complex and some components cannot be easily isolated. Sometimes the only way to test if they are working or not is by replacing them.

Budget considerations have prevented us from replacing key components that might have been responsible for the accelerate dephasing and as it stands, the system is unable to perform Ramsey interferometry on time scale longer than 50 ms.

CHAPTER 6

Rephasing dynamics of a bosonic Josephson junction

Josephson junctions are interacting quantum systems composed of two weakly coupled, macroscopic quantum states. They were first realized in the context of superconductivity, when two superconductors are separated by a thin insulating barrier and the electrons are allowed to tunnel across it. Josephson predicted [108] in 1962 that such system will develop a nondissipative current whose value depends on the relative phase of the order parameter describing each superconductor through the relation

$$I(\phi) = I_c \sin(\phi) \tag{6.1}$$

where I_c is the critical current and ϕ is the relative phase, with each superconductor's phase $\theta(r)$ assumed to be approximately uniform. This effect is called the direct current Josephson effect and differs from the alternating current Josephson effect which arises when a nonzero chemical potential difference $\mu = \mu_2 - \mu_1$ is present, causing the phase to rotate as [108]

$$\frac{d\phi}{dt} = -\frac{\mu}{\hbar} \quad (6.2)$$

and creating an oscillating current across the junction. The Josephson relations apply to any pair of weakly coupled quantum systems that can be described by macroscopic wave functions [109]. BECs are among these systems, since they can be described by the complex order parameter $\Psi(r) = \sqrt{\rho(r)}e^{i\phi}$.

Bosonic Josephson junctions (BJJ) can be experimentally made by spatially separating the condensate in a double well potential with the coupling provided by tunneling. The coupling strength controlled by the height of the potential barrier between the wells. This type of junction is called an external BJJ. Another way to create a BJJ is to have condensed atoms sharing the same trap, but being in different internal states. This is the path we follow at Swinburne and, since we populate the hyperfine states $|F = 1, m = -1\rangle$ and $|F = 2, m = +1\rangle$ of ^{87}Rb , the coupling is provided by MW fields. These junctions are called internal BJJ.

When an external BJJ is subjected to a quantum quench, these systems are expected to show "rephasing" dynamics, first predicted by DallaTorre et al [2]. In other words, initially independent, phase incoherent condensates will develop a well defined phase relationship, present at all time scales, through the combined effect of the atomic interactions and the tunneling coupling. This effect is also expected to be universal, with the strength of the quench only affecting the time scale but ultimately leading to the same outcome. In this chapter we describe both the external and internal Josephson junction and give a description of the condition under which the rephasing effect is expected to take place.

6.1 Double well Josephson junctions

A full quantum description of a double well Josephson junction can be given in a two-mode approximation [110, 111]. Such a description is accurate at very low

temperature due to the small separation between the ground and first excited state of the double well, which are almost degenerate in the weak interaction case, and the much bigger separation between the first and second excited states, greatly reducing the probability for these states to be populated. The field operator can be written as a superposition of these two states [112]

$$\hat{\Psi} = \hat{a}_g \Phi_g(\mathbf{r}) + \hat{a}_e \Phi_e(\mathbf{r}) \quad (6.3)$$

where $\Phi_g(\mathbf{r})$ and $\Phi_e(\mathbf{r})$ are mean field spatial modes obtainable using GPE equation, Eq. 2.3, \hat{a}_g and \hat{a}_e are the annihilation operators for a particle in the ground and excited state respectively. Due to the symmetry of the problem, a more convenient basis to describe the system uses the states for which the populations are sharply peaked on the right or left well. Annihilation operators \hat{a}_L and \hat{a}_R for the left and right side of the well are related to the previously defined ground and excited state annihilation operators by

$$\hat{a}_L = \frac{1}{\sqrt{2}}(\hat{a}_g + \hat{a}_e) \quad \hat{a}_R = \frac{1}{\sqrt{2}}(\hat{a}_g - \hat{a}_e) \quad (6.4)$$

and the field operator in the new basis becomes

$$\hat{\Psi} = \frac{1}{\sqrt{2}}[\hat{a}_L(\Phi_g + \Phi_e) + \hat{a}_R(\Phi_g - \Phi_e)] = \frac{1}{\sqrt{2}}(\Psi_1 + \Psi_2) \quad (6.5)$$

The Hamiltonian for a system of N bosons, trapped in a double well potential and with contact interactions can be written as

$$\hat{H} = \int d\mathbf{r} \left(-\frac{\hbar^2}{2m} \hat{\Psi}^\dagger \nabla^2 \hat{\Psi} + \hat{\Psi}^\dagger V_{DW} \hat{\Psi} + \frac{g}{2} \hat{\Psi}^\dagger \hat{\Psi}^\dagger \hat{\Psi} \hat{\Psi} \right) \quad (6.6)$$

where g is the interaction constant $g = 4\pi\hbar^2 a/m$, a is the s-wave scattering length and V_{DW} is a double well potential. For the case of Oberthaler's first realization of a double well Josephson junction the confining potential was [113]

$$V_{DW} = \frac{1}{2}m(\omega_x^2 x^2 + \omega_y^2 y^2 + \omega_z^2 z^2) + \frac{V_0}{2} \left(1 + \cos \frac{2\pi}{d} x \right) \quad (6.7)$$

After the substitution of equation (6.5) in equation (6.7) we obtain the two mode Hamiltonian [112]

$$\hat{H}_{2m} = \frac{E_c}{8}(\hat{a}_R^\dagger \hat{a}_R - \hat{a}_L^\dagger \hat{a}_L)^2 - \frac{E_j}{N}(\hat{a}_L^\dagger \hat{a}_R + \hat{a}_R^\dagger \hat{a}_L) + \frac{\delta E}{4}(\hat{a}_L^\dagger \hat{a}_R + \hat{a}_R^\dagger \hat{a}_L)^2 \quad (6.8)$$

given the parameters

$$E_c = 8\kappa_{g,e} \quad E_j = \frac{N}{2}(\mu_e - \mu_g) - \frac{N(N+1)}{2}(\kappa_{e,e} - \kappa_{g,g}) \quad (6.9)$$

$$\delta E = \frac{\kappa_{g,g} + \kappa_{e,e} - 2\kappa_{g,e}}{4} \quad \kappa_{i,j} = \frac{g}{2} \int d\mathbf{r} |\Phi_i|^2 |\Phi_j|^2 \quad (6.10)$$

$$\mu_{g,e} = \int d\mathbf{r} \left(-\frac{\hbar^2}{2m} \Phi_{g,e} \nabla^2 \Phi_{g,e} + \Phi_{g,e} (V_{DW} + gN |\Phi_{g,e}|^2) \Phi_{g,e} \right) \quad (6.11)$$

with the term proportional to E_c taking into account interaction within each well, the term in E_j describing tunneling between the two wells and the term in δE representing additional two particle processes. By neglecting the term in δE we arrive at the Bose-Hubbard Hamiltonian [112]

$$\hat{H}_{BH} = \frac{E_c}{2} \hat{n}^2 - E_j \hat{\alpha} \quad (6.12)$$

where

$$\hat{n} = \frac{\hat{a}_R^\dagger \hat{a}_R - \hat{a}_L^\dagger \hat{a}_L}{2} \quad (6.13)$$

is the population imbalance operator, divided by two since a particle jumping from one side to the other of a double well changes the population by two and

$$\hat{\alpha} = \frac{\hat{a}_R^\dagger \hat{a}_L + \hat{a}_L^\dagger \hat{a}_R}{2} \quad (6.14)$$

is the tunneling operator. The mean value of the tunneling operator corresponds to the first order spatial coherence function $g^{(1)}(\mathbf{r}, \mathbf{r}')$ and measures the visibility of the fringes obtained when the condensates are released from their traps. Depending on the ratio between the tunneling and the interaction energy E_c/E_j [114] the ground state of the Bose-Hubbard Hamiltonian can be described by three different regimes [115, 116]:

Rabi regime for $E_c/E_j \ll N^{-2}$, corresponds to the non-interacting regime, where Rabi-like oscillations are driven due to the coupling provided by tunneling. The coherence is high and a relative phase can be defined.

Josephson regime for $N^{-2} \ll E_c/E_j \ll 1$, is the regime we are most interested in, characterized by small fluctuations in the atom numbers leading to Josephson-like oscillations of the population imbalance. The coherence is still high, allowing for the definition of a relative phase like in the Rabi case.

Fock Regime for $1 \ll E_c/E_j$, the system is described by states with a well defined atom number in each well, the coherence vanishes and the phase is undefined. The phase is undefined in the sense that interference patterns can still be observed but the patterns are changing from realization to realization in the same conditions. The states show no temporal evolution and if the initial state has been prepared with a population imbalance, that imbalance will remain constant. The Fock regime is therefore not compatible with the idea of "a single condensate in a double well", but corresponds to two independent condensates on each side of the well. This case is called a fragmented state [117].

A mean field description of the system is possible for large atom numbers by replacing the creation and annihilation operators in equation (6.7) with complex numbers according to the Bogoliubov prescription [118] $\hat{a}_{L,R} = \sqrt{N_{L,R}(t)}e^{i\phi_{L,R}(t)}$ and complex conjugate for the creation operator. The mean field Hamiltonian reads

$$H_{MF} = \frac{E_c}{2}n^2 - E_j\sqrt{1 - \frac{4n^2}{N^2}}\cos\phi \quad (6.15)$$

where $n = (N_R - N_L)/2$ is the population imbalance and $\phi = \phi_R - \phi_L$ is the relative phase. The equation of motion are [111]

$$\frac{dn}{dt} = -\frac{1}{\hbar}\frac{\partial H_{MF}}{\partial\phi} = -\frac{E_j}{\hbar}\sqrt{1 - \frac{4n^2}{N^2}}\sin\phi \quad (6.16)$$

$$\frac{d\phi}{dt} = -\frac{1}{\hbar} \frac{\partial H_{MF}}{\partial n} = \frac{E_c}{\hbar} n + \frac{E_j}{\hbar} \frac{4n}{N^2} \left(\sqrt{1 - \frac{4n^2}{N^2}} \right)^{-1} \cos \phi \quad (6.17)$$

The quantities n and ϕ are canonically conjugate variables and the dynamics correspond to that of a nonrigid pendulum with length proportional to the population imbalance. When $n = 0$ and $\phi = 2m\pi$, with m integer, the system is in the ground state and does not change. For a small population imbalance $n_0^2 \ll N^2$, corresponding to a small initial kick given to the pendulum, or for an initial phase $\sin \phi_0 \approx \phi_0$, corresponding to a small displacement from the ground state position, the equations of motion become

$$\frac{dn}{dt} = -\frac{E_j}{\hbar} \phi \quad \frac{d\phi}{dt} = \left(\frac{E_c}{\hbar} + \frac{4E_j}{\hbar N^2} \right) n \quad (6.18)$$

and current will start to flow across the barrier and the population imbalance will display harmonic (Josephson) oscillations given by

$$n(t) = n_0 \sin(\omega_p t + \phi_0) \quad (6.19)$$

where ω_p is the characteristic plasma frequency

$$\omega_p = \frac{1}{\hbar} \sqrt{E_j \left(E_c + \frac{4E_j}{N^2} \right)}. \quad (6.20)$$

If the initial population imbalance is large enough, so that the kick given to our nonrigid pendulum is able to swing it over the vertical position, the mean population imbalance will be different from zero. The critical value of the initial imbalance is therefore given by

$$n_c = 2 \sqrt{\frac{E_j}{E_c} \left(1 - \frac{4E_j}{N^2 E_c} \right)} \quad (6.21)$$

and above n_c the condensate enters the macroscopic self trapping regime [115], a state ultimately caused by particle self-interaction. The non rigidity of the pendulum allows for oscillations to be found for small amplitude around $\phi = (2m + 1)\pi$, a condition unstable in a rigid pendulum.

6.2 Two component Josephson junction

The internal state evolution of a 2CBEC can be described in Bloch vector notation using the one-axis twisting Hamiltonian [119]

$$\frac{\hat{H}}{\hbar} = \delta \hat{S}_z + \Omega \hat{S}_\theta + \chi \hat{S}_z^2 \quad (6.22)$$

where $\hat{S}_\phi = \cos(\theta)\hat{S}_x - \sin(\theta)\hat{S}_y$ and $\hat{S}_x, \hat{S}_y, \hat{S}_z$ are the spin operator components, defined in second quantization as

$$\begin{aligned} \hat{S}_x &= \frac{1}{2} \int d^3r (\hat{\Psi}_2^\dagger \hat{\Psi}_1 + \hat{\Psi}_1^\dagger \hat{\Psi}_2) & \hat{S}_y &= \frac{1}{2} \int d^3r (\hat{\Psi}_2^\dagger \hat{\Psi}_1 - \hat{\Psi}_1^\dagger \hat{\Psi}_2) \\ \hat{S}_z &= \frac{1}{2} \int d^3r (\hat{\Psi}_2^\dagger \hat{\Psi}_2 - \hat{\Psi}_1^\dagger \hat{\Psi}_1) \end{aligned} \quad (6.23)$$

where $\hat{\Psi}_i = \hat{\Psi}_i(\mathbf{r})$ is the bosonic annihilation operator for an atom in state $|i\rangle$ at position \mathbf{r} . It follows that $\hat{\Psi}_1(\mathbf{r}) = \hat{a}_1 \psi_0(\mathbf{r})$ and $\hat{\Psi}_2(\mathbf{r}) = \hat{a}_2 \psi_2(\mathbf{r})$, where \hat{a}_1 and \hat{a}_2 are bosonic annihilation operators and $\psi_1(\mathbf{r})$ and $\psi_0(\mathbf{r})$ are solution to the GPE equation. The first term in equation(6.22) describes spin precession around the z-axis at the detuning $\delta = \omega_d - \omega_0$, ω_d being the frequency of a two photon driving pulse and ω_0 being the frequency separation of the hyperfine states. The second term describes spin rotations around an axis forming an angle θ with the x-axis at a frequency Ω . It is straightforward to identify Ω with the Rabi frequency and θ with the phase of the two photon coupling. The last, nonlinear term in \hat{S}_z , with strength χ , is due to elastic collision and twists the states on the Bloch sphere around the z-axis with direction and speed of rotation dependent of the state's distance with respect to the equatorial plane. This term is central in the understanding of the rephasing dynamics we want to observe and will be discussed in the next section.

The 2CBEC Hamiltonian can be rewritten in a form similar to equation (6.15), thus highlighting the similarities between a two component BEC and a double well Josephson junction [120]. By noting that

$$S_y^2 + S_x^2 = S^2 - S_z^2 = \frac{N^2}{4} - S_z^2 \quad (6.24)$$

where $S = \sum_j^N s_j$ is the total spin of the system and N is the total number of atoms and

$$S_\theta = \frac{N}{2} \sqrt{1 - \frac{4S_z^2}{N^2}} \cos \phi \quad S_z = \frac{N_2 - N_1}{2} = n \quad \phi = \phi_2 - \phi_1 \quad (6.25)$$

with ϕ the relative phase and n the population imbalance defined in the previous section. The Hamiltonian (6.22), after the substitution of equation (6.24) and (6.25) becomes

$$H_{jj} = \delta n - \Omega \frac{N}{2} \sqrt{1 - \frac{4S_z^2}{N^2}} \cos \phi + \chi n^2 \quad (6.26)$$

which, for $\delta = 0$ is nearly identical to the Hamiltonian of a double well Josephson Junction. Following the same procedure used in the section on double-well Josephson junctions we can write Hamilton's equation for the time evolution of the conjugate variables n and ϕ [50]

$$\frac{dn}{dt} = \frac{\partial H_{jj}}{\partial \phi} = \frac{\Omega N}{2} \sqrt{1 - \frac{4n^2}{N^2}} \sin \phi \quad (6.27)$$

$$\frac{d\phi}{dt} = \frac{\partial H_{jj}}{\partial n} = -2\chi n + \frac{4\Omega n}{N \sqrt{1 - \frac{4n^2}{N^2}}} \cos \phi \quad (6.28)$$

The set of equations (6.27)-(6.28) is exactly the same as for the double well, equations (6.16)-(6.17).

6.3 Universal rephasing dynamics in a quenched Josephson junction

Dalla Torre et al, in their 2013 paper [2], have studied the dynamics of a quantum quench where two initially independent condensates are suddenly coupled. They predicted that the time evolution of physical observables of the system, in the limit of weak coupling, follows a universal scaling law of the form [2]

$$C(t) = \left(\frac{\Delta}{\mu} \right)^\eta R(\Delta t) \quad (6.29)$$

where $C(t)$ is a generic observable, η is the scaling dimension corresponding to the observable $C(t)$, $R(\Delta t)$ is a scaling function, μ is the chemical potential and Δ is the size of the gap opened by the quench in an otherwise gapless Hamiltonian. In this section we will briefly review their findings, with particular attention on the coherence factor $\langle \cos \phi \rangle$ as the relevant observable. As we will see, the effect of the quench will be to "rephase", or force coherence in the initially incoherent independent condensates. The coherence factor is expected to follow the scaling law, equation (6.29), at both short and long evolution time, providing a way to link short-time dynamics, that can be found by perturbing steady state solution, to long time dynamics, where perturbation theory does not apply. The original proposal focused on two condensates trapped in a double well potential, coupled by tunneling. The potential barrier separating each side of the well is initially kept high, the coupling is negligible and the Hamiltonian describes two individual condensates

$$H(t) = \frac{\mu}{N}(\delta n_1^2 + \delta n_2^2) \quad (6.30)$$

where $\delta n_{1,2} = \Psi_{1,2}^\dagger \Psi_{1,2} - N/2$, with $\Psi_{1,2}$ being the bosonic field operators already described in the double well Josephson junction section (Eq.6.5). This Hamiltonian describes interactions among the atoms in the same condensate and is clearly gapless. After some time t , the system is quenched by the sudden lowering of the potential barrier with the condensate coupled through tunneling. The Hamiltonian after the quench reads

$$H(t) = \frac{\mu}{N}(\delta n_1^2 + \delta n_2^2) - \Theta(t)j_\perp(\Psi_1^\dagger \Psi_2 + \text{H.c}) \quad (6.31)$$

where j_\perp is the tunneling coupling and $\Theta(t)$ is the Heaviside step function. This Hamiltonian can be written in Josephson form by using $\Psi_{1,2} = \sqrt{N_{1,2}}e^{i\phi_{1,2}}$, giving

$$H(t) = \frac{2\mu}{N}n^2 - 2\Theta j_\perp N \cos(\sqrt{2}\phi) \quad (6.32)$$

If we treat the quench as a small perturbation we can approximate $\cos(\sqrt{2}\phi) \approx 1 - \phi^2$ and retrieve undamped harmonic oscillations with plasma frequency proportional to

the gap size, $\omega_p = \Delta = 2\sqrt{\mu j_\perp}$, given by

$$\frac{d^2\phi}{dt^2} = -\frac{\Delta^2 \sin(\sqrt{2}\phi)}{\sqrt{2}} \quad (6.33)$$

This however is not the solution found by DallaTorre through exact diagonalization of the full quantum Hamiltonian, equation (6.31). The solution shows strongly damped oscillations at a frequency Δ , clarifying the non-perturbative nature of the problem [2]. In fact the initial state has a large overlap with a macroscopic number of eigenstates of the Hamiltonian after the quench, which forces us to consider all high order expansions of the cosine and highlights the strongly interacting nature of the quench.

The same predictions of damped harmonic oscillations can be obtained by applying a semiclassical approach [121, 122] based on the truncated Wigner approximation. This model correctly reproduces the results of the full quantum model and provides an analytical expression for the time evolution of the relative phase. The application of the semiclassical method leads to the surprising result that the dynamics follow the equation of motion of a simple pendulum, with the quantum nature of the problem entering through the initial conditions, for which ϕ is uniformly distributed between 0 and 2π . It is this uniform distribution of initial conditions which is responsible for the damped oscillations.

In a 2CBEC internal Josephson junction, which is the case of interest for the experimental setup in Swinburne, the application of the method discussed above leads to the equation

$$\frac{d^2\phi}{dt^2} = -\frac{\Omega N}{2} \left(2\chi + \frac{4\Omega n}{N} - 2\Omega^2 \cos \phi \right) \sin \phi \quad (6.34)$$

which simplifies, in the case of weak coupling, to

$$\frac{d^2\phi}{dt^2} \approx -\frac{\Omega N}{2} \left(2\chi + \frac{4\Omega n}{N} \right) \sin \phi \quad (6.35)$$

A graphical representation of the expected dynamics can be obtained using the Bloch sphere, figure 6.1, and considering the one-axis twisting Hamiltonian, equation (6.22). The introduction of the weak coupling displaces the the spin vector from

the equatorial plane and, given $\chi \neq 0$, allows them to rotate around the z-axis. It is remarkable that different rotational velocities and different initial positions work together to change the initial uniform distribution of the spin vectors, with coherence factor defined as $\alpha = \langle \cos \phi \rangle$ [34], equal to zero (incoherent), into a new, partially coherent, distribution with a nonzero value of the coherence factor.

Solutions to sets of equation (6.35), corresponding to different, uniformly distributed initial values of the relative phase and different evolution times can be seen in figure 6.2, while the evolution of the coherence factor is depicted in figure 6.3. The simulations confirm the scaling ansatz of equation (6.29), with oscillation of frequency $\Delta = 2\sqrt{\chi\Omega}$. The initially incoherent system reaches a coherence peak of about $\alpha \approx 0.78$ after a time $t \approx 2$ and then stabilizes around $\alpha \approx 0.4$ for longer times, thus partially "rephasing" the condensates. The universality of the dynamics can be seen in figure 6.4, where the time evolution of the coherence factor follows equation (6.29) for different ratios of coupling and interaction strength, with $\eta = 0$.

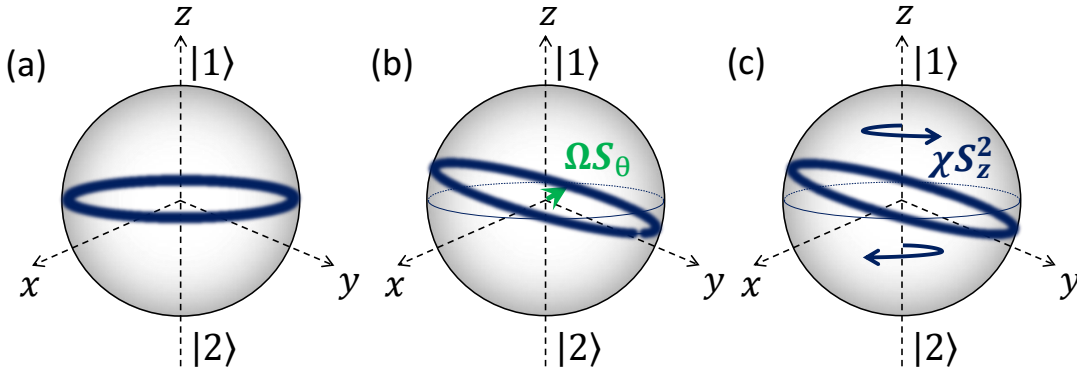


Figure 6.1: Bloch sphere representation of the dynamics involved in rephasing. **(a)** The blue fuzzy circumference on the equator represents a two component BEC with equal population and uniformly distributed relative phase. Such a condition can be created by independently condensing an equal mixture over many repetitions. **(b)** The weak coupling Ω , represented by the green arrow, rotates the circumference around S_θ , here chosen to be aligned with the x -axis. **(c)** Nonlinearities cause the points on the circumference to rotate around the z -axis with a speed proportional to the distance from the equatorial plane, according to χS_z^2 . Furthermore, due to the S_z^2 dependence, points lying in the northern hemisphere rotate counterclockwise, while points in the southern hemisphere rotate clockwise. Simplifying, different points rotates with different speed starting from different initial positions but end up after an evolution time t clustered together more tightly than when they started, thus increasing the chance of detecting them in a specific range. This, combined with the fact that at long evolution times we do not recover the initial uniform relative phase distribution, is the essence of rephasing. Detuning is not shown in in this representation but it also causes rotation around the z -axis proportional to δS_z . However the linear S_z dependence is crucial, since northern and southern hemisphere rotate in the same direction and no change in the probability distribution is caused by detuning.

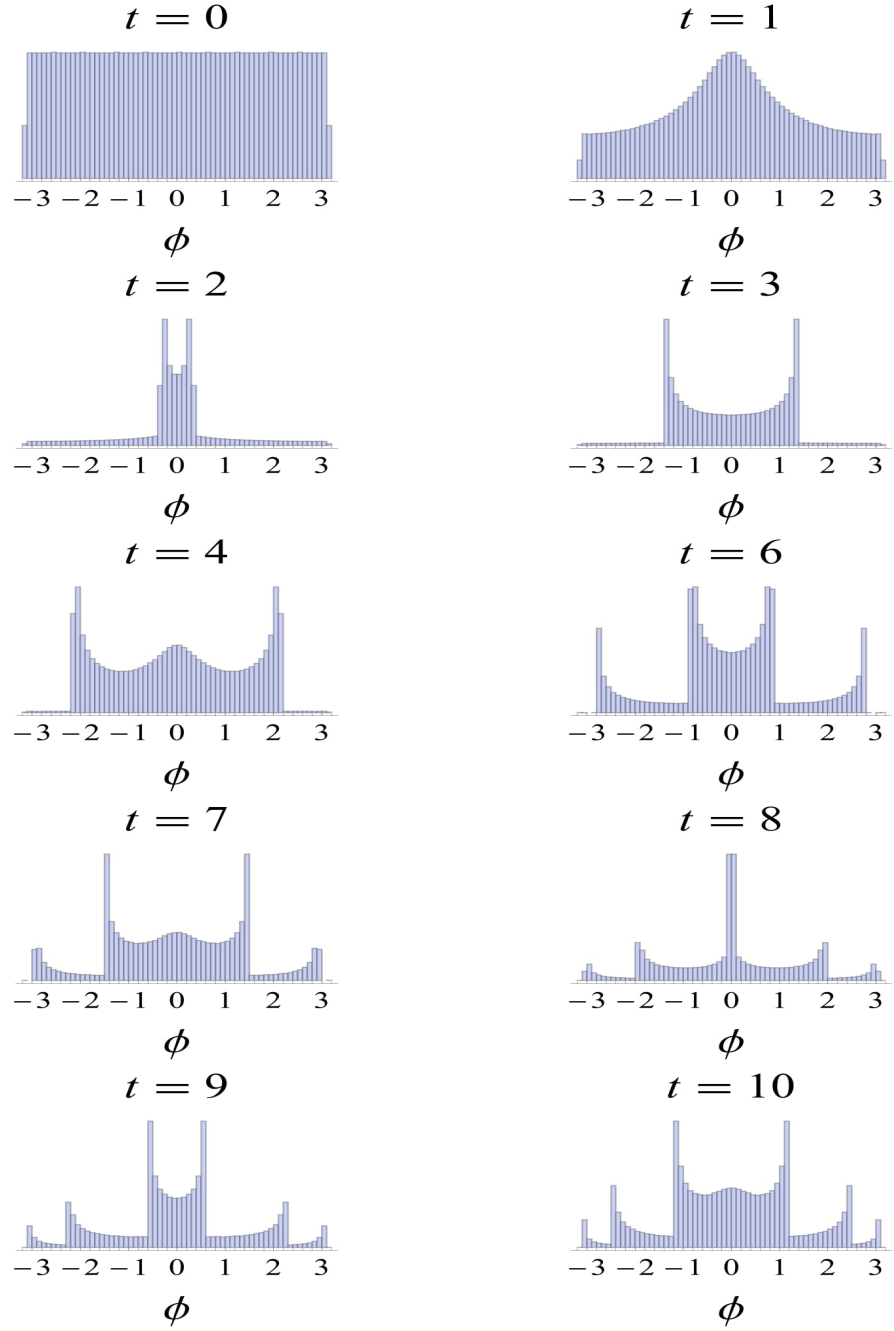


Figure 6.2: Distribution of the relative phase of two initially independent condensates calculated using the semiclassical approach, equation (6.35). The time is expressed in units of inverse plasma frequency, $t = 1/2\sqrt{\Omega\chi}$.

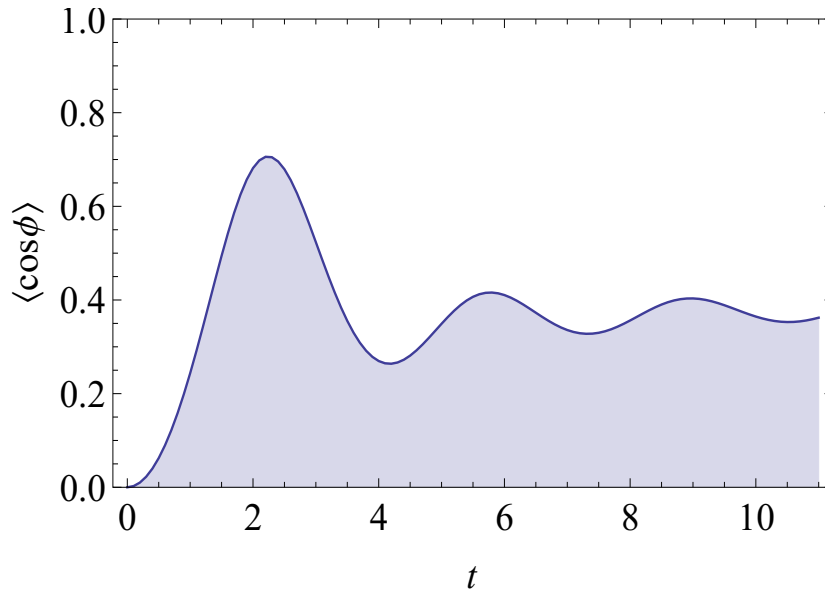


Figure 6.3: Time evolution of the coherence factor $\langle \cos(\phi) \rangle$ obtained with the semiclassical approach, equation (6.35). The time is expressed in units of inverse plasma frequency, $t = 1/2\sqrt{\Omega\chi}$.

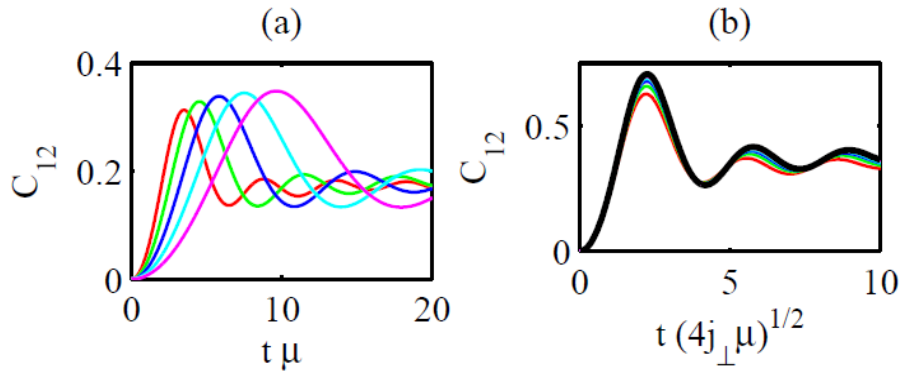


Figure 6.4: Time evolution of the coherence factor calculated by exact diagonalization of the Hamiltonian (6.31) for $N=1000$ particles. (a) Coherence factor for different values of the ratio j_{\perp}/μ , with the red line being characterized by the strongest coupling and the pink one by the weakest. (b) By rescaling the axes, the universal behavior outlined by equation (6.29) is evident, with $\eta = 0$. Adapted from [2].

The model discussed so far involves conditions that need to be analyzed more carefully in order for an experiment to be carried out. The "sudden" quench is modeled with a Heaviside step function, which is clearly an idealization of finite quenching time involved in the experiment. The model of a sudden quench is expected to hold if the finite quenching time τ is smaller than the inverse of the energy of the highest excited scale. This puts a constraint on τ such that $\tau \ll 1/N\Omega$. Witthaut et al. have pointed out in ref. [123] that the most probable excitation path does not connect directly the ground to the highest excited state, thus giving a less stringent condition $\tau \ll 1/2\sqrt{\chi\Omega}$. Another condition involves the coupling, supposed to be weak, setting a constraint $\Omega \ll \mu$. Finally the coefficient χ requires careful consideration, because, along with Ω sets the time scale of the dynamics. The expression for χ can be written as [43]

$$\chi = \frac{1}{2\hbar}(\partial_{N_1}\mu_1 + \partial_{N_2}\mu_2 - \partial_{N_2}\mu_1 - \partial_{N_1}\mu_2)_{\langle N_1 \rangle, \langle N_2 \rangle} \quad (6.36)$$

showing a dependence on the derivatives of the chemical potential, which in turn is defined as

$$\mu_j = \langle \psi_j | h_j | \psi_j \rangle + \sum_{k=1,2} g_{jk} N_k \int dr^3 |\psi_j|^2 |\psi_k|^2 \quad (6.37)$$

and $g_{jk} = 4\pi\hbar^2 a_{jk}/m$ is as usual the interaction strength, with a_{jk} the s-wave scattering length, N_1, N_2 are the mean atom numbers and h_j is the single particle Hamiltonian. If we neglect the dependence of the spatial wave function on the atom number, we can neglect the first term of equation (6.37) and we arrive at the simplified version [124]

$$\chi = \frac{1}{2\hbar}(U_{11} + U_{22} - 2U_{12}) \quad (6.38)$$

$$U_{jk} = g_{jk} \int dr^3 |\psi_j|^2 |\psi_k|^2 \quad (6.39)$$

From equation (6.38) we can see that χ depends on the scattering lengths and on an overlapping integral of the wavefunctions of our 2CBEC. For the states $|F = 1, m = -1\rangle$ and $|F = 2, m = +1\rangle$ of ^{87}Rb used in the experiments, the scattering lengths are very similar in value ($a_{11} = 100.40 a_0$, $a_{12} = 98.01 a_0$, $a_{22} = 95.44 a_0$) [44]

and if the modes overlap equation (6.38) gives $\chi \approx 0$, suppressing the rephasing. Control over the overlapping integral is achieved by relying on the non-miscibility of the condensed states, which leads to a spatial separation of the modes and to a χ different from zero. However having merely a positive χ does not solve the problem, since it still can be small enough to cause rephasing dynamics to happen on a time scale where other dephasing mechanism can hide the effect we are interested to measure.

6.4 Immiscible 2CBEC and nonlinear interactions

A 2CBEC is said to be miscible if the wave function of each component are energetically favored to coexist over the same space. Otherwise the condensate is said to be immiscible and the components wave functions will try to avoid each other. One way to obtain a criterion that marks the passage between miscibility and immiscibility is to use a Bogoliubov-deGennes analysis, which allows us to find the excitation spectrum and the spatial modes of two stationary states. We consider an initially homogeneous two-component condensate whose evolution is described by the CGPE of chapter 2, equation 2.3. For simplicity we set the coupling, the losses, the detuning and the trapping potential to zero ($\Omega = \delta = \Gamma_i = V_i = 0$). Excitations for trapped condensates are more difficult to deal with, but lead to similar results and a discussion can be found in [45]. We assume $\psi_{i,0}(\mathbf{r}, 0)$ to be a steady state solution of the simplified CGPEs, with a temporal evolution given by

$$\psi_{i,0}(\mathbf{r}, t) = e^{-\frac{i\mu_i t}{\hbar}} \sqrt{n_i} \quad (6.40)$$

then we define $\delta\psi_i(\mathbf{r}, t)$ as a perturbation on top of $\psi_{i,0}(\mathbf{r}, t)$ and we replace the new state

$$\psi_i(\mathbf{r}, t) = e^{-\frac{i\mu_i t}{\hbar}} (\sqrt{n_i} + \delta\psi_i(\mathbf{r}, t)) \quad (6.41)$$

in the CGPE. After neglecting terms higher than first order we are left with [46, 125]

$$i\hbar \frac{\partial}{\partial t} \delta\psi_i = -\frac{\hbar^2 \nabla^2}{2m} \delta\psi_i + g_{ii} n_i (\delta\psi_i + \delta\psi_i^*) + g_{i2} \sqrt{n_i n_2} (\delta\psi_2 + \delta\psi_2^*) \quad (6.42)$$

Assuming solutions of the form

$$\delta\psi_i = u_{i,\mathbf{k}} e^{i(\mathbf{k}\cdot\mathbf{r} + \omega t)} \quad \delta\psi_i^* = v_{i,\mathbf{k}} e^{i(\mathbf{k}\cdot\mathbf{r} - \omega t)} \quad (6.43)$$

leads to the Bogoliubov-de Gennes equations

$$\left(\omega - \frac{\hbar^2 k^2}{2m}\right) u_{\mathbf{k},i} = \sum_{j=1,2} g_{ij} \sqrt{n_i n_j} (u_{\mathbf{k},j} + v_{\mathbf{k},j}) \quad (6.44)$$

$$\left(-\omega - \frac{\hbar^2 k^2}{2m}\right) v_{\mathbf{k},i} = \sum_{j=1,2} g_{ij} \sqrt{n_i n_j} (u_{\mathbf{k},j} + v_{\mathbf{k},j}) \quad (6.45)$$

The system of four coupled equations can be further simplified by shifting to the basis of sum and differences of $u_{\mathbf{k},j}$ and $v_{\mathbf{k},j}$ in which the equations can be written as

$$\begin{pmatrix} g_{11}n_1 & g_{12}\sqrt{n_1 n_2} \\ g_{12}\sqrt{n_1 n_2} & g_{22}n_2 \end{pmatrix} \begin{pmatrix} u_{1,j} \pm v_{1,j} \\ u_{2,j} \pm v_{2,j} \end{pmatrix} = \frac{\hbar^2 k^2}{2m} \left(1 - \frac{2m\omega}{\hbar^2 k^2}\right)^2 \begin{pmatrix} u_{1,j} \pm v_{1,j} \\ u_{2,j} \pm v_{2,j} \end{pmatrix} \quad (6.46)$$

and the dispersion relation is given by

$$\omega^2 = \frac{\hbar^2 k^2}{2m} \left(\frac{\hbar^2 k^2}{2m} + 2\eta_{\pm} \right) \quad (6.47)$$

with η_{\pm} eigenvalues of the matrix

$$G = \begin{pmatrix} g_{11}n_1 & g_{12}\sqrt{n_1 n_2} \\ g_{12}\sqrt{n_1 n_2} & g_{22}n_2 \end{pmatrix} \quad (6.48)$$

The two eigenvalues η_+ and η_- corresponds to eigenvectors $(u_{1,j} + v_{1,j}, u_{2,j} + v_{2,j})$ and $(u_{1,j} - v_{1,j}, u_{2,j} - v_{2,j})$ which in turn correspond to in-phase and out of phase oscillations. In the long wavelength limit, $k \rightarrow 0$, the dispersion relation reduces to

$$\omega^2 = \eta_{\pm} = \frac{n}{4} \left(g_{11} + g_{22} \pm \sqrt{(g_{11} - g_{22})^2 + 4g_{12}^2} \right) \quad (6.49)$$

which further reduces, in the case of equal densities $n_j = n/2$, to

$$\omega^2 = \frac{n\hbar^2 \pi}{m} \left(a_{11} + a_{22} \pm \sqrt{(a_{11} - a_{22})^2 + 4a_{12}^2} \right) \quad (6.50)$$

A homogeneous system is thus stable if no imaginary energies exist, which leads to the condition [45, 46]

$$a_{12}^2 \leq a_{11}a_{22} \quad (6.51)$$

If equation (6.51) is violated the condensates will lower their energy by decreasing the overlap for the case of repulsive interaction, or by increasing it for attractive interactions. There is no stable state for attracting condensates in the untrapped case, which will collapse, but the presence of a trapping potential allows for a condensate with a number of particles below a critical value N_c to be stable. For rubidium 87 the scattering lengths do violate equation (6.51) and the ground state for different atom number is shown in figure 6.5, where the immiscibility is clearly visible.

Equation (6.51) is a useful tool for understanding the behavior of 2CBEC, however the situation can change dramatically if a coupling is established between the condensates, as will be illustrated in the next chapter and as highlighted in Ref. [126]. The now dressed states have stationary states that depends on the strength and detuning of the coupling, making the simple picture "component 2 squeezed in the middle and component 1 spread at the edge" typical of the bare states of ^{87}Rb much more complicated. Finally, in a recent paper, Lee et al [127] pointed out the crucial dependence of miscibility on atom number, suggesting that equation (6.51) is not the optimal parameter to characterize the miscibility of trapped atoms since the interaction threshold between miscibility and immiscibility and different regimes of immiscibility depends on the atom number of each component.

The simulation of the ground state of a 2CBEC allows us to estimate the rephasing period since we have access to the overlapping integral and we can calculate the coefficient χ (see figure 6.6).

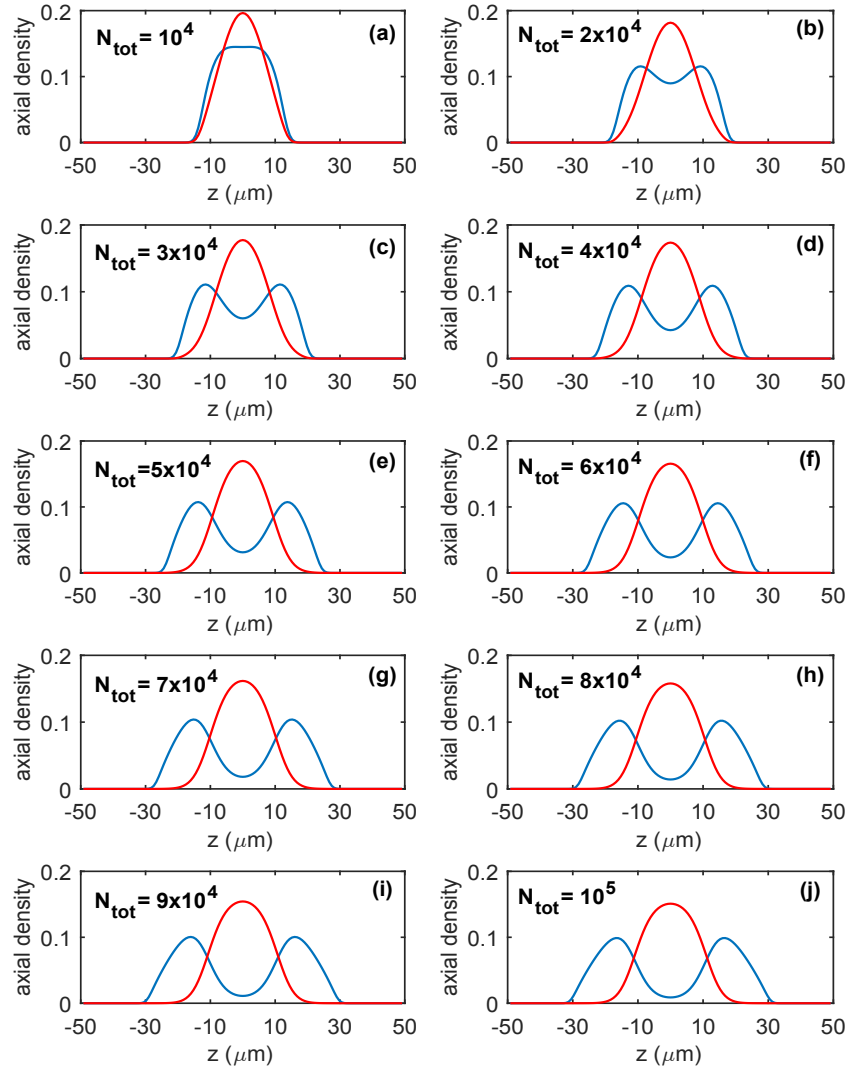


Figure 6.5: Axial density distribution for the ground state of an equally populated two component BEC with total atom number varying between 10^4 (a) to 10^5 (j). The stronger repulsive interaction experienced by the clouds is responsible for the increased separation with increasing particle number. The simulations have been performed for the experimental trap frequencies $\omega_{ax} = 11.7$ Hz and $\omega_r = 97$ Hz.

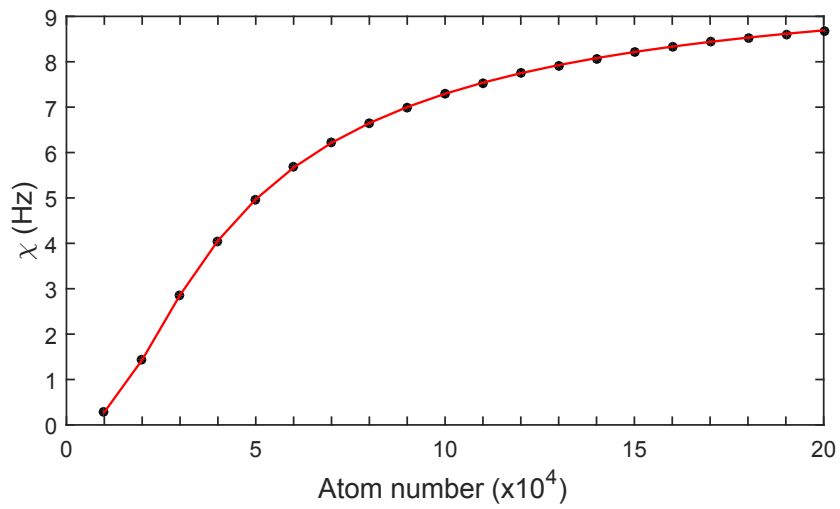


Figure 6.6: Nonlinear coefficient χ as a function of total atom number for the ground state of an equally populated 2CBEC . χ increases by increasing the total number of particles by virtue of the fact that the overlapping between each component wave function decreases.

CHAPTER 7

Rephasing Dynamics of a bosonic Josephson Junction, experimental results

In this chapter we present the result of the experiments aimed at achieving rephasing in a Josephson junction, according to the theory presented in chapter 6. The observation of such dynamics is required to validate the claim previously formulated of universal behavior in systems away from equilibrium. While the original proposal called for a realization in a double well, here at Swinburne we have the technology to allow us to explore a different realisation. For this reason we have realized the alternative condition in which the repulsive interactions experienced by a 50:50 superposition of two hyperfine states of rubidium 87 provide a similar environment for this dynamics to occur. The cleanest and most robust way to achieve this condition is to create the superposition of hyperfine states when the atoms are still not condensed, and then condense them independently. This would guarantee the two component system to be in their ground state, with a uniformly distributed initial relative phase, crucial for our observations, provided by the spontaneous symmetry breaking. Once this condition is achieved, then the "sudden" and "weak" coupling is turned on in the form of a microwave field, and the phase converted in relative population with the application of a $\pi/2$ pulse after varying evolution times, to

recover the expected scaling relation. The universality would follow by varying the strength of the microwave field. This is the focus of the first part of the chapter. However there are technical challenges which have prevented us from obtaining condensates of the required size and purity to be useful, given the stringent requirements outlined in chapter 6. We have consequently opted for a different approach, where we condense the atoms in the same state and transfer half of them with a first $\pi/2$ pulse, wait for the two condensates to separate, then apply the rephasing coupling and finally apply the second $\pi/2$ pulse, but crucially with a phase which is different from the first one. This approach is equivalent to performing a standard Ramsey interferometry, but with a randomized phase relationship between the two pulses, which is equivalent to the uniform distribution of the relative phase achieved with independent condensation. After many realizations, if the rephasing dynamics are present, we should observe a clustering of experimental points around values of relative population close to zero when compared to the case where the microwave coupling is not applied, which in turn would signify a non-zero coherence factor. This approach has its problems as well, since by creating the initial superposition we are triggering other dynamics in the system, like breathing modes and nonuniform phase growth, which affects the absolute value of the visibility. Additionally, a collective oscillation requires around 200 ms to create the right condition (nonlinear coefficient χ large enough to generate rephasing on a meaningful time scale). This time is long enough for other effects, like losses, to affect the coherence of the system and to influence the separation. The results for this "engineered" phase approach will make up most of the second part of the chapter. Finally, in the third part, in an effort to reduce collective oscillations and decrease the waiting time before the application of the coupling, we have explored an adiabatic $\pi/2$ pulse to create the initial superposition. Simulations have shown that if the initial $\pi/2$ pulse of a Ramsey sequence is weak, the system follows the ground state and the oscillations are greatly suppressed. However the solutions now depends on the strength and the detuning of the weak initial $\pi/2$ pulse, leading to configurations that can differ

greatly from the ground state of a 2CBEC, with state $|1\rangle$ at the sides of the trap and state $|2\rangle$ in the middle. Those effects are not necessarily bad. On the contrary, they can even help improve the quality of the interferometry, as will be explained later, but add a layer of complexity in the control of the overlap. Furthermore, for both the adiabatic and non adiabatic "engineered phase" approaches the system cannot be considered suddenly quenched, raising serious concern on their feasibility. All these points and others will be treated more carefully in the concluding section.

7.1 Independent Condensation

Independent condensation of two atomic ensembles trapped in different states is the most straightforward and clean way to create the conditions for the observation of the rephasing dynamics described in chapter two, given our current experimental setup. The experiment requires the creation of a mixture of two hyperfine states before the condensation, so that the two components should truly be initially incoherent. Having fulfilled this condition, over many repetitions we expect to obtain a uniform distribution of initial relative phases. A second $\pi/2$ pulse applied to the condensates after some evolution time t should convert the phase into relative population and the observable P_z , defined as

$$P_z = \frac{N_2 - N_1}{N_1 + N_2} \quad (7.1)$$

where N_1 and N_2 are the populations in each state, should be uniformly distributed between the maximum and minimum value of the visibility. The visibility itself depends on the overlap between the wave functions of the two components, which is not perfect since we need a separation in order to have a nonzero χ . This is expected to decrease the visibility. The homogeneity of the phase across the condensates also influences the visibility, but for a condensate in its ground state, as in this case, there is no relative motion and the phase is indeed uniform. Finally the evolution time t should be short, so that decoherence through losses or phase diffusion does

not affect the system significantly. The distribution of P_z in the absence of coupling should then be compared to the distribution of P_z in the presence of the weak coupling Ω . The coupling, together with the interactions, should trigger the rephasing dynamics causing the experimental points, uniformly distributed across the range of the visibility for the evolution time t in the absence of coupling, to cluster around some specific value of P_z , according to figure 6.2 in chapter 6. The coherence factor $\langle \cos \phi \rangle$ should then move away from zero, with the points more tightly clustered as the contrast approaches 1 and then it should exhibit the damped oscillatory behavior for longer evolution times highlighted in figure 6.3 of chapter 6.

We attempted to produce an incoherent 2CBEC of ^{87}Rb by first trapping the atoms into the state $|F = 1, m_F = -1\rangle$, then by transferring half of them with a $\pi/2$ pulse in state $|F = 2, m_F = +1\rangle$ and finally evaporating the mixture to degeneracy. This approach proved unfeasible at the usual experimental trap bottom of 3.23 Gauss because of Zeeman shift of the magnetic levels. Between the states $|F = 1, m_F = -1\rangle$ and $|F = 2, m_F = +1\rangle$ and their respective $m_F = 0$ states to which they are coupled during evaporation there is a differential shift of ≈ 11 kHz. The result of this shift is that we effectively cut in component $|2\rangle$ while component $|1\rangle$ is still non pure and we always ended up with a decent sized $|2\rangle$ and a relatively thermal $|1\rangle$, or a pure $|1\rangle$ and a tiny $|2\rangle$. Remember that the size of the condensate is a primary concern since, as explained in chapter 6, and as shown in figure 6.6, it drives the spatial separation which in turn determines the nonlinear coefficient χ required for rephasing. The next step consisted of using an RF coupling to evaporate state $|1\rangle$ and a MW field to evaporate state $|2\rangle$ by coupling it to the untrapped $|F = 1, m_F = +1\rangle$.

This approach failed for lack of power in the microwave field. State $|2\rangle$ was barely affected by the coupling and increasing the evaporation length had a negative effect on the total atom number due to the increased importance of losses for this state, since it is not maximally stretched. We decided to lower the trap bottom to the minimum value that allowed us to reliably produce a single component BEC, thus decreasing the Zeeman splitting. It turned out that the minimum value achievable

was ≈ 0.5 G, due to the fact that stray external magnetic field, switch instabilities and current fluctuations can affect the trap bottom at even lower magnetic fields, causing the final number of condensed atoms to fluctuate wildly or preventing condensation altogether. A normal evaporation cycle of 15 seconds would have caused the population of state $|2\rangle$, which has a lifetime of about 500 ms due to spin relaxation, to drop unacceptably low. We have used a two stage evaporation trajectory based on the following scheme

- Efficient cooling of component $|1\rangle$ for 10 seconds in a 0.5 G trap. The final evaporation frequency of this cooling sits at about 400 kHz, 30 kHz above the condensation threshold
- Quick (≈ 1 ms) $\pi/2$ pulse to transfer half of the cold but non condensed atoms in state $|2\rangle$
- Compressing of the trap to increase rethermalization efficiency without changing the trap bottom, stable at 0.5 G, on a 10 ms scale
- 100 ms evaporation of both components from an initial frequency of 420 kHz to the final evaporation frequency of ≈ 370 kHz

This scheme was successful in achieving independent condensation, proof of which is provided in figure 7.1, where the parabolic distribution typical of the condensed state sits on top of a Gaussian distributed thermal fraction. To check that we did actually achieve independent condensation and not just a 50:50 split of atoms already condensed in state $|1\rangle$ we switched off the second evaporation sweep and repeatedly observed simple thermal clouds for the two components. As an additional sign of genuine independent condensation we looked for the separation of the cloud and we checked for the suppression of relative motion. The relative motion was indeed absent, but the separation was rather small.

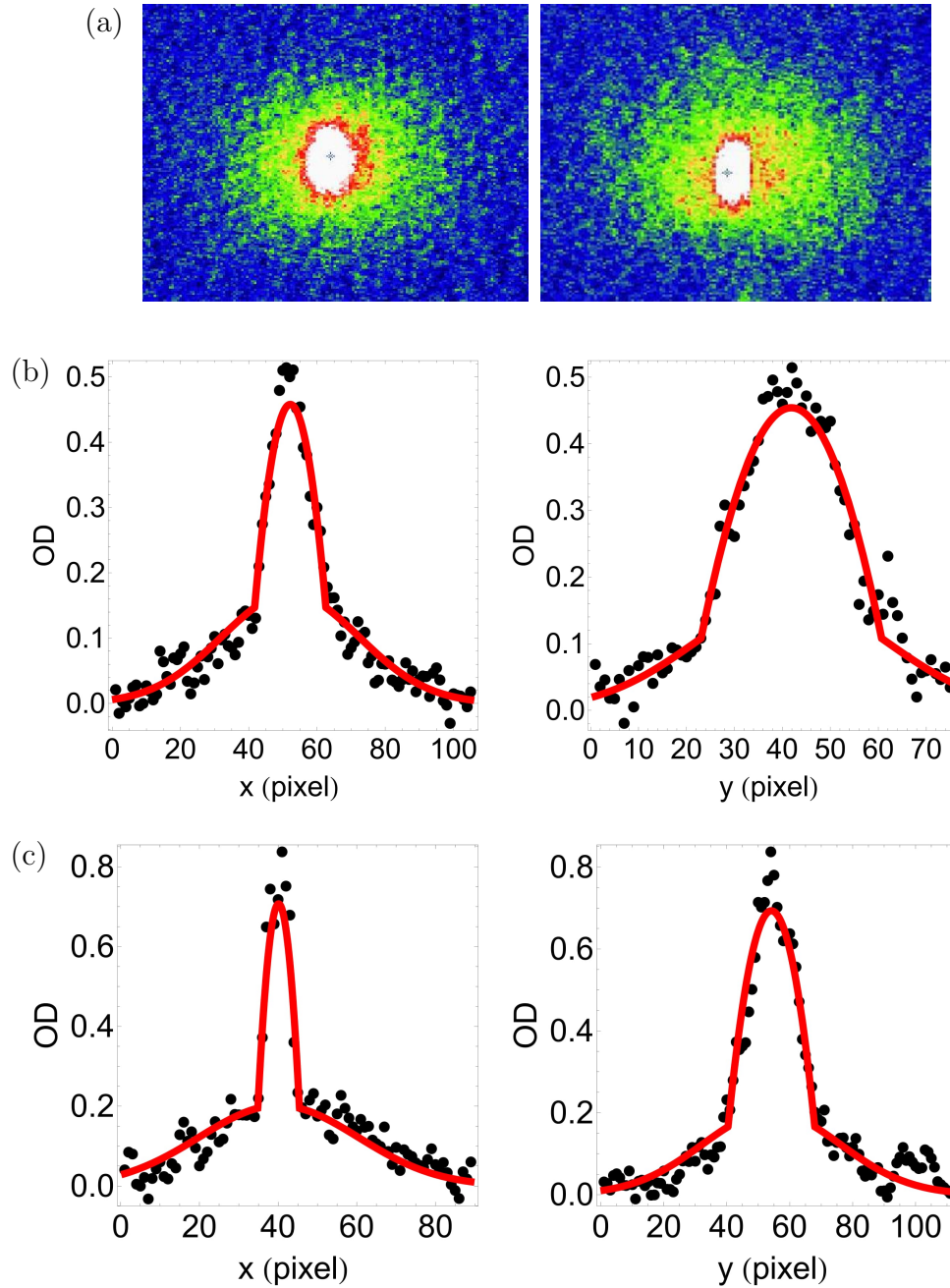


Figure 7.1: (a) Absorption images of a 2CBEC obtained through independent condensation of component $|1\rangle$ (left) and component $|2\rangle$ (right) in a trap with $\omega_{y,z} = 2\pi \cdot 97$ Hz and $\omega_x = 2\pi \cdot 11$ Hz. As can be seen from the images the thermal fraction is substantial, and for this particular case accounts for $\approx 50\%$ of the total atom number. State $|1\rangle$ has $3.45 \cdot 10^4$ atoms of which $1.83 \cdot 10^4$ are condensed. State $|2\rangle$ has $3.18 \cdot 10^4$ atoms, $1.38 \cdot 10^4$ condensed. The compression of component $|2\rangle$ is immediately visible. (b,c) Axial (left) and radial (right) density profile for component $|1\rangle$ (b) and component $|2\rangle$ (c) after independent condensation. The condensed part is clearly visible. The effective pixel size is $4.5\mu\text{m}$.

This was because of the substantial thermal cloud that always accompanies the condensates produced with this method. The actual condensed part corresponds to 50% of the total atom number, which is typically between $6 \cdot 10^4$ to $7 \cdot 10^4$ atoms, giving a value of only $1.5 \cdot 10^4$ to $1.75 \cdot 10^4$ condensed particles in each component, much too small to provide a meaningful separation, as is depicted in figure 7.2. Furthermore such a big thermal cloud has a negative effect on the interferometry measurements, due to the decohering effects of the interaction between condensed and non condensed atom detailed in chapter 4 and in reference [103]. All these reasons forced us to abandon the independent condensation approach and switch to the "engineered phase" method.

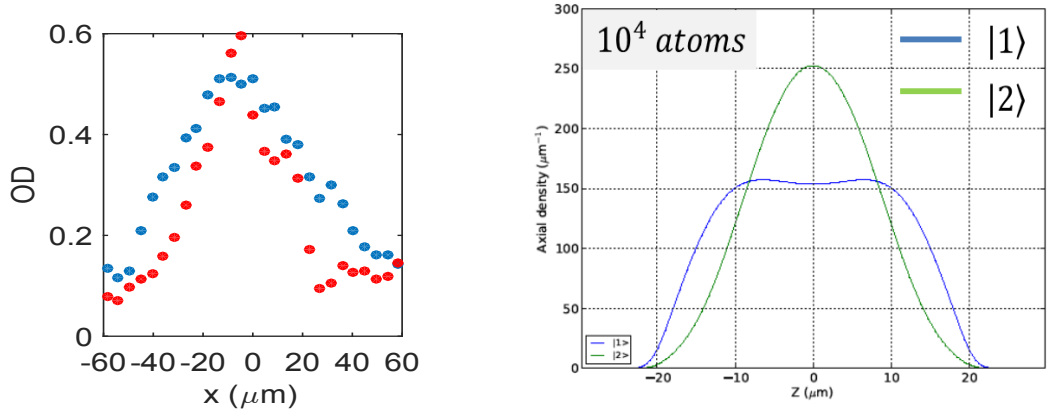


Figure 7.2: (a) Measured spatial density distribution of the condensed part for the cloud shown in figure 7.1. $N_1 = 1.83 \cdot 10^4$ and $N_2 = 1.38 \cdot 10^4$. (b) Simulated density distribution for the ground state of an equally split 2CBEC of $N_{tot} = 2 \cdot 10^4$ atoms. The measurements closely resemble the simulations for the corresponding total number of atoms, but the overlapping is unacceptably high.

7.2 Rephasing through engineered phase

In order to lessen the downsides of independent condensation we opted to implement what we called an "engineered phase" sequence to achieve the conditions for rephas-

ing. The idea is simple: we realize a standard Ramsey sequence with an initial $\pi/2$ pulse with phase ϕ_1 that we vary, from shot to shot, between 0 and 2π , creating a uniform distribution. We then let the system evolve for a time t , we apply a weak coupling Ω with a phase ϕ_2 different from ϕ_1 for a time τ compatible with the expected rephasing period and we apply the second $\pi/2$ pulse with the same phase as the weak coupling. The phase ϕ_2 Figure 7.3 offers a Bloch sphere description of the dynamics involved, and a schematic representation of the experimental sequence. The relative population P_z is related to the relative phase ϕ at time T through

$$P_z = \mathcal{V} \cdot \sin \phi(T) \quad (7.2)$$

where \mathcal{V} is the interference contrast. To make a more immediate comparison with the simulation of chapter 6, expressed in terms of coherence factor $\langle \cos \phi \rangle$, we can recover the phase from the measurements of P_z using

$$\phi(T) = \arcsin(P_z/\mathcal{V}) \quad (7.3)$$

and then average over the cosine. It is clear that in the case without coupling we should recover a uniform distribution of the relative phase with the mean value $\langle \cos \phi \rangle = 0$. Therefore we look for variations in $\langle \cos \phi \rangle$ when the coupling is applied. The coupling is expected to cause the experimental points to cluster around $P_z = 0$, with the extent of the clustering following a damped oscillatory behavior represented in figure 6.3 of chapter 6. However we tread on dangerous ground since the system is not in equilibrium when the actual rephasing pulse is applied, due to the fact that the initial $\pi/2$ pulse already causes the system to be in an excited state. The condition for the system to be suddenly quenched is therefore violated, with implications that require additional theoretical analysis in future extensions of this work.

The requirement for separation of the two wave functions are satisfied only through the effect of breathing, since after the initial, quick $\pi/2$ pulse the wave functions overlap.

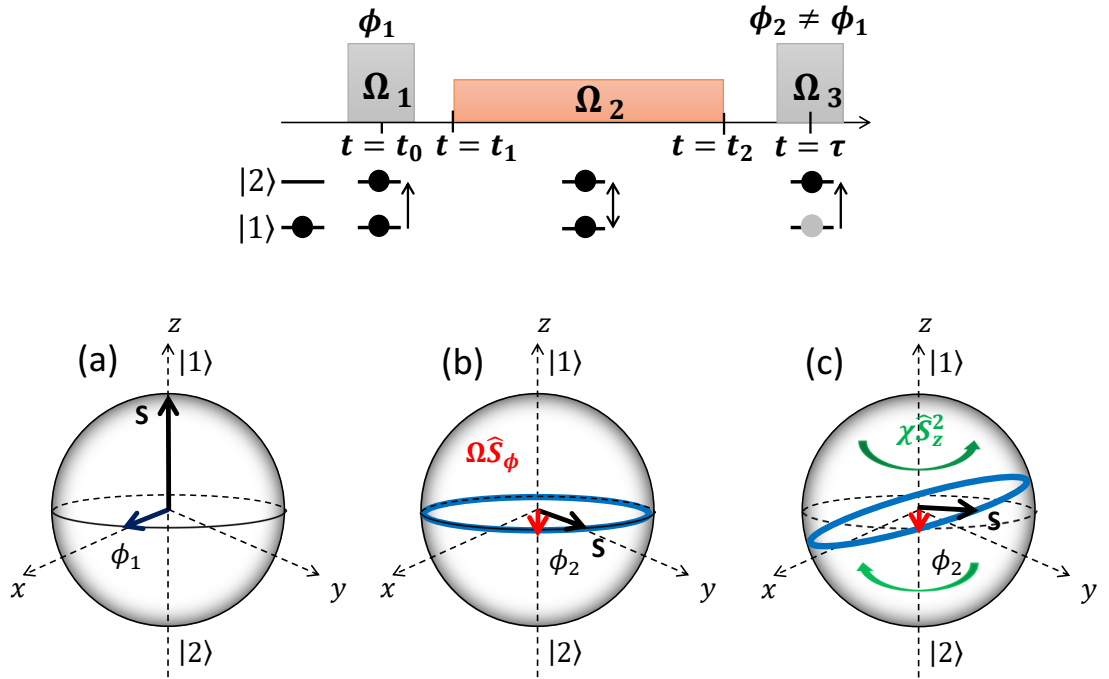


Figure 7.3: Engineered phase rephasing sequence. The condensate, initially ($t = t_0$) in state $|1\rangle$, is coherently transferred by a $\pi/2$ pulse with phase ϕ_1 (**blue arrow**), arbitrarily chosen to be in the x -axis direction, to state $|2\rangle$ (**a**). The mean spin vector S (**black arrow**), under the effect of the $\pi/2$ pulse, rotates around the x -axis until it lies on the equator (**b**) and we have an equal superposition. By varying the value of the phase ϕ_1 we can send the mean spin vector S to an arbitrary position on the equatorial plane thus creating, over many repetition, uniformly distributed initial conditions (**blue circle**). After some time t_1 , chosen to maximize the nonlinear coefficient χ , a weak rephasing pulse (**red arrow**) is applied for a duration $t = t_2$, with a phase ϕ_2 , arbitrarily chosen at the beginning of the experiment and kept constant in each repetition. During this evolution time the S vector rotates around the direction of the weak coupling and at the same time nonlinearities (**green arrows**) cause a rotation around the z -axis whose speed is proportional to χS_z^2 (**c**). A final $\pi/2$ pulse (**red arrow** with the same phase ϕ_2 as the weak coupling pulse converts the relative phase into population difference P_z . If rephasing is observable, the probability of measuring values close to $P_z = 0$ is expected to increase compared to the case when the weak rephasing coupling is absent. The detuning is assumed to be close to zero ($\delta \approx 0$)

The separation is at its maximum after about 200 ms in our current experimental conditions, which is a time long enough for the system to experience decoherence through losses and phase diffusion. What is desirable during the application of the coupling, a small overlap, it is undesirable for the interference contrast, that is improved by a high overlap. Additionally relative motion of the condensates cause the phase to be non-homogeneous, further reducing the contrast. We cannot avoid the relative motion, since it is required for separation and we cannot control the overlap in order to have different overlapping regimes during the coupling and just before the last $\pi/2$ pulse is applied. This does not prevent the rephasing, but makes it more difficult to be detected, since now the points are spread between a shorter range of values of P_z and variations are more difficult to detect.

We also explored a different approach that was aimed at suppressing the collective oscillation, reducing the waiting time before the application of the coupling, but still achieving reasonable separation of the clouds. It uses a very weak $\pi/2$ pulse initially creating the superposition so slowly that the components almost adiabatically follow the ground state. This results in a reduction of the relative motion and a waiting time of only 40 ms. However the miscibility now becomes dependent on the strength of the pulse and the detuning, as well as on the number of atoms, making the initial conditions more difficult to control .

Both methods and their experimental results will be described in detail in the next sections

7.2.1 Rephasing with a fast $\pi/2$ splitting

Here we present the results for the fast $\pi/2$ splitting method. In this experiment we first condense $\approx 10^5$ atoms in state $|F = 1, m_F = -1\rangle$ with a 3.23 G trap bottom and then transfer half of them to $|F = 2, m_F = +1\rangle$ with a MW+RF pulse having a Rabi frequency $\Omega_{\pi/2} = 2\pi \cdot 1$ kHz. The uncertainty associated with our $\pi/2$ transfer is usually $\approx 1\%$, which is a good approximation of an equal superposition.

Additionally this is a non adiabatic transfer and the wave functions are effectively "frozen" during its application. This means that at the end of the coupling the wave functions for the two states almost perfectly overlap and the system is in a non equilibrium state. Subsequently the components will start to oscillate out of phase, with component $|1\rangle$ pushed toward the edge of the trap and component $|2\rangle$ compressed in the middle.

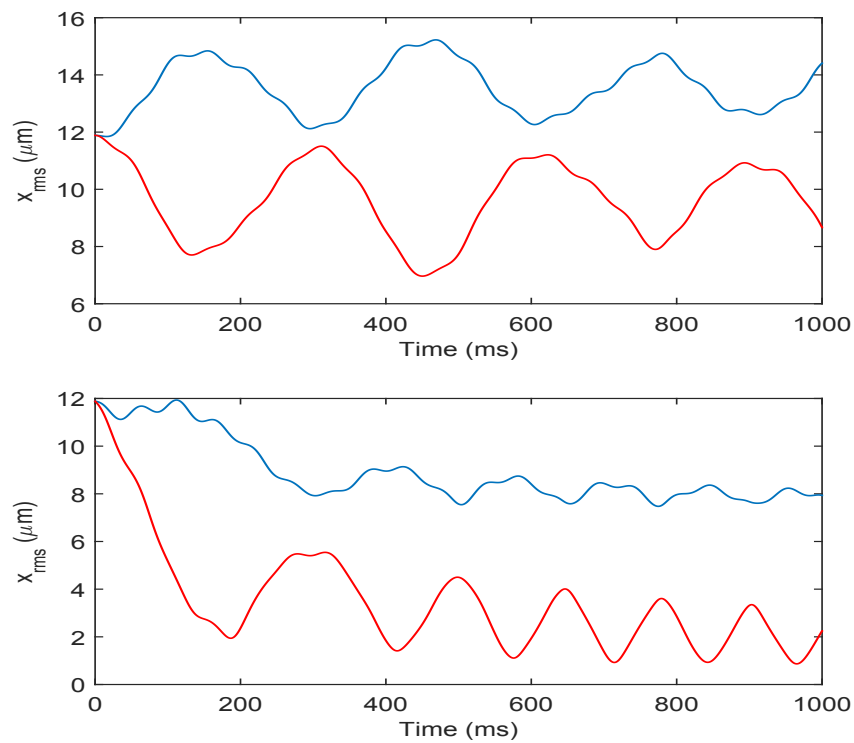


Figure 7.4: Simulated time evolution of the root mean square width, giving an idea of each component's wave function width, defined as in equation (7.4), in the presence (**top**) and absence (**bottom**) of particle losses. Oscillations with a period of ≈ 150 ms are visible in the lossless case, while the situation is more complicated when losses are present. In the lossy case, component $|2\rangle$ (**red trace**), after an initial transient behavior lasting around 400 ms, exhibit almost perfect sinusoidal oscillations with a period of 170 ms. On the other hand the width of component $|1\rangle$ (**blue trace**), after the initial transient, remains almost constant.

Figure 7.4 show CGPE simulation of the root mean square width of the wave functions of each component with respect to the axial direction, which is to say

$$x_{i,rms} = \left(\int x^2 |\Psi_i|^2 dx dy dz \right)^{1/2} \quad (7.4)$$

giving an idea of the width of each component of a condensate with $N_{tot} = 10^5$ in our typical experimental conditions ($\omega_x = 2\pi \cdot 11$ Hz, $\omega_y = \omega_z = 2\pi \cdot 97$ Hz, scattering length and losses as described in chapter 2). The simulations allow us to obtain quantitative results on the period of oscillations, which are in agreement with the measurements previously performed on the setup (see chapter 5 and Ref. [73, 82]).

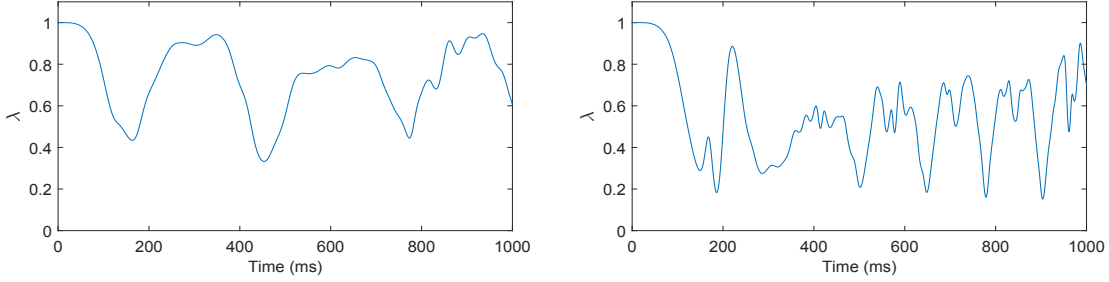


Figure 7.5: Simulated time evolution of the normalized density overlap λ in the presence (**left**) and absence (**right**) of particle loss. The window chosen to perform the experiment lies between 150 and 190 ms, which minimizes waiting time while providing poor overlapping and in turn high nonlinear χ coefficient and shorter rephasing period.

Figure 7.5 shows the evolution of the normalized density overlap λ defined as

$$\lambda = \frac{\int dr^3 |\Psi_1|^2 |\Psi_2|^2}{\sqrt{\int dr^3 |\Psi_1|^4 \int dr^3 |\Psi_2|^4}} \quad (7.5)$$

which is a crucial parameter in determining when the rephasing coupling should be applied. The overlapping is at a minimum after 185 ms, but as can be seen from the simulations, it quickly rises in about 30 ms to a value $\lambda = 0.9$.

Since this is a nonequilibrium situation, the best way to calculate the coefficient χ is through the derivative of the chemical potential, instead of the overlapping

integral, using equation 6.36 of chapter 6. The derivative of the chemical potential is calculated by evolving CGPE with different values of N_1 and N_2 , usually $N_1 = N/2 \pm 10^3$, $N_2 = N/2 \mp 10^3$. The results agree fairly well with the overlapping integral method and give a value of $\chi \approx 9 \text{ s}^{-1}$. With a coupling strength $\Omega = 2\pi \cdot 75 \text{ Hz}$ this gives a characteristic rephasing time $\tau = 1/2\sqrt{\Omega\chi} = 19.2 \text{ ms}$ which brings us into the high overlapping area, grinding the dynamics to an effective halt after a single oscillation. For this reason we apply the rephasing coupling after 150 ms, which provides us with 50 ms of coupling time with a maximum overlap of $\lambda = 0.5$. We wait for 150 ms after the first $\pi/2$ for the best separation condition to happen and we apply a weak coupling in the form of a 2 photon MW+RF field of Rabi frequency $\Omega \approx 2\pi \cdot 75 \text{ Hz}$ and a different phase compared to the first $\pi/2$. With the coupling on, we let the system evolve for a variable time t ranging between 10 and 40 ms and then we apply a second $\pi/2$ pulse that concludes the Ramsey sequence. This second pulse has the same phase as the weak coupling. Additionally this phase changes from realization to realization in order to create a uniform distribution of the relative phase between the first and second $\pi/2$ pulse for any given evolution time t . The atoms are then released, fall under gravity for 10 ms and are imaged using the adiabatic passage method previously described in chapter 3. The phase distribution obtained in the presence of coupling is compared with the phase distribution extracted using the same Ramsey scheme, but in the absence of coupling. We check for variation in the coherence factor $\langle \cos\phi \rangle$ which signifies a tighter clustering of points around $\phi = 0$ compared to the non rephased (absence of coupling) case.

As an additional test to characterize the coherence of the system we perform Ramsey interferometry in the phase domain at 10, 50, 100 and 150 ms. We fit the experimental data with a sinusoidal function, equation 7.2, we recover the visibility \mathcal{V} and, after normalizing the measured P_z by the visibility extracted from the fit, we calculate the phase shift. The phase shift is defined as the departure of experimental

points from the ideal sinusoidal behavior and is calculated as

$$\delta\phi = \arcsin(P_{z(\text{ideal})}) - \arcsin(P_z) \quad (7.6)$$

where $P_{z(\text{ideal})}$ are points lying on the fitted sine for the corresponding relative phase between the Ramsey pulses. Figure 7.7 shows some typical examples of Ramsey fringes at different evolution time as they look after being collected in the experiment, with the sinusoidal fit closely following the experimental points and, in polar representation, the phase shift distribution. Figure 7.8 displays the coherence factor $\langle \cos \phi \rangle$ of the measured phase distributions for different evolution times. The coherence is very high in the first 50 ms, with $\langle \cos \phi \rangle = 0.96$ for $t = 10$ ms and $\langle \cos \phi \rangle = 0.91$ for $t = 50$ ms. It drops to $\langle \cos \phi \rangle = 0.75$ for $t = 100$ ms but then it remains stable at this value after 150 ms of evolution, when the rephasing experiment takes place. The error bars on each point of figure 7.8 are calculated as $\sigma(\phi)/\sqrt{(M-1)}$, where $\sigma(\phi)$ is the phase uncertainty extracted from the fit and M is the number of measurements, with at least $M = 60$.

The results for the rephasing experiment are shown in figure 7.9. The Ramsey fringes, collected in the presence and absence of coupling, form the basis for our analysis. The visibility is low, on average $\mathcal{V} = 0.2$, in agreement with the simulations in figure 5.4, chapter 5. This is mostly due to inhomogeneous phase evolution across the spatial extent of the condensate, but also due to decoherence and poor overlap. As a first step we analyze the unrephased fringes by dividing the measured values of P_z by the visibility and we recover the phase corresponding to each value of P_z through the application of equation 7.3. This serves as an initial phase distribution against which the rephased fringes are compared. The final step in the analysis requires the phase of each of the measured values of P_z in a rephased fringe to be obtained using the same procedure as for the unrephased case. Comparison of the phase of points having the same Ramsey pulses relative phase in the presence and absence of rephasing coupling should allow us to detect the motion due to the coupling and an eventual departure from a uniform phase distribution.

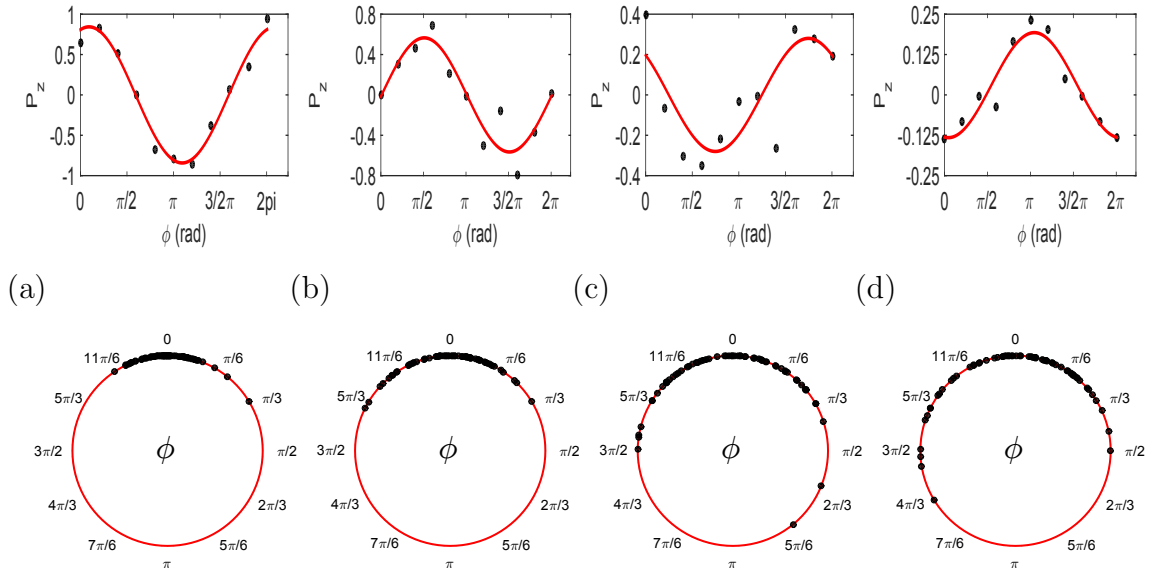


Figure 7.7: Ramsey fringes acquired by varying the phase of the second Ramsey pulse after $t = 10$ ms (a), $t = 50$ ms (b), $t = 100$ ms (c) and $t = 150$ ms (d) of free evolution. The red line is a sinusoidal fit while the black dots are experimental points.

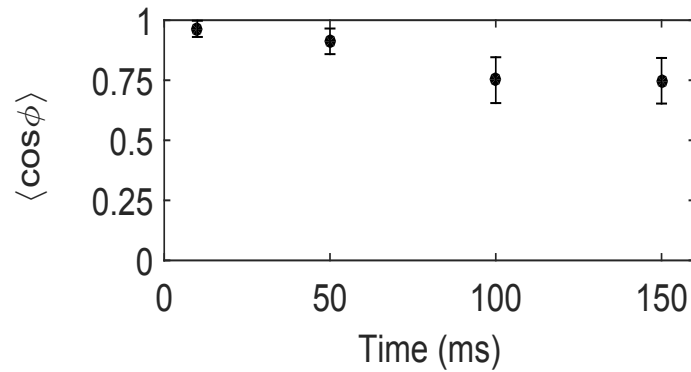


Figure 7.8: Coherence factor obtained by taking the average of the cosine of the phase distributed as in the polar plots of figure 7.7. The coherence is highest for $t = 10$ ms with $\langle \cos \phi \rangle = 0.96$, dropping to $\langle \cos \phi \rangle = 0.74$ after $t = 150$ ms of free evolution.

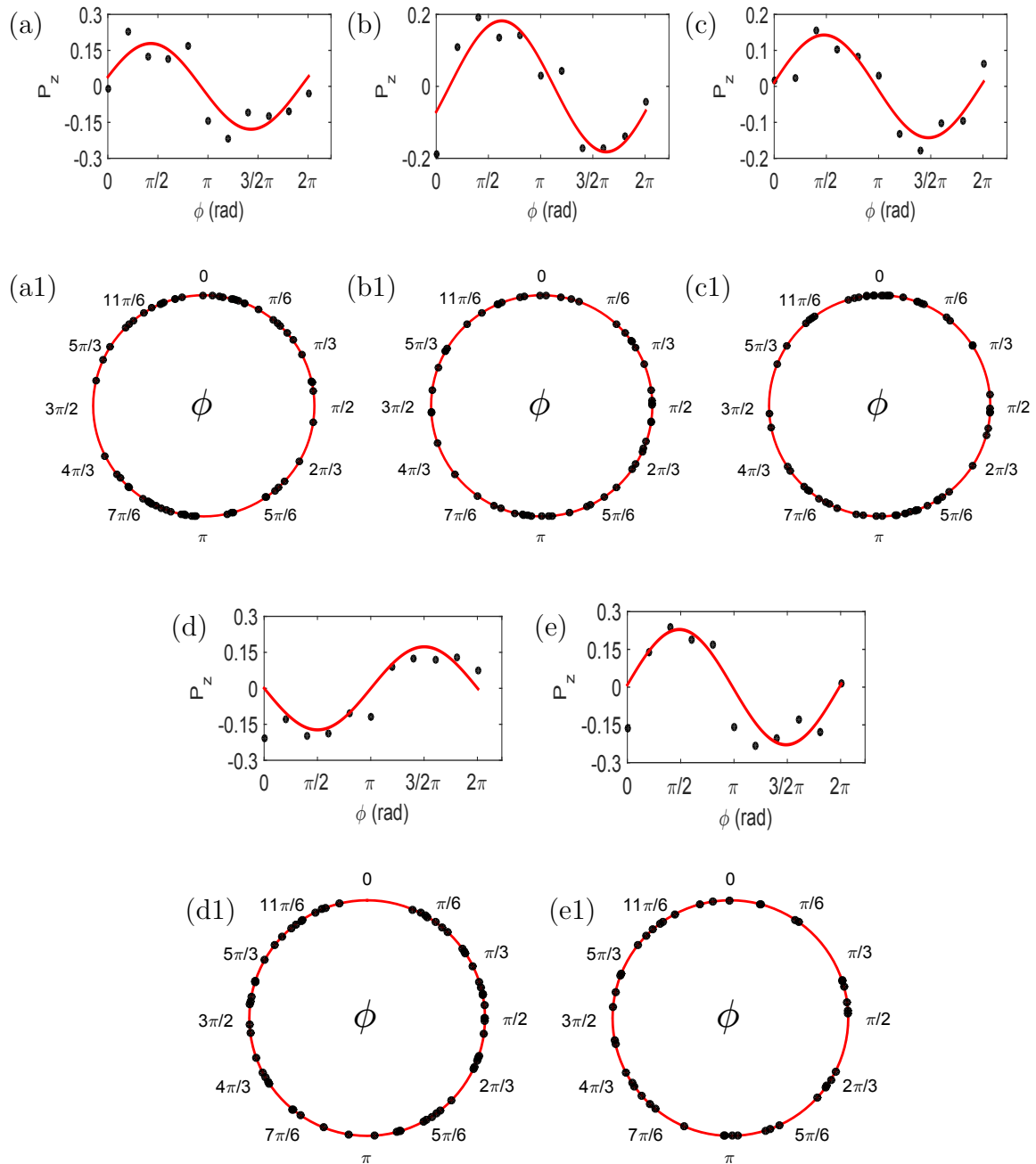


Figure 7.9: (a,b,c,d,e) Ramsey fringes acquired by varying the phase of the second Ramsey pulse after 150 ms of free evolution and the additional application of a rephasing coupling with duration $t = 10$ ms (a), $t = 15$ ms (b), $t = 20$ ms (c), $t = 30$ ms (d) and $t = 40$ ms (e). The red line is a sinusoidal fit while the black dots are experimental points. (a1,b1,c1,d1,e1) Polar plots showing the relative phase distribution corresponding to at least 40 measurements for each duration of the rephasing pulse. The uniformity of the distribution suggests absence of rephasing.

Having access to the phase allows us to plot the experimental data in polar coordinates, providing a visual representation of the phase distribution. Rephasing is expected to alter the distribution from uniform to peaked around $\phi = 0$. The polar plots clearly show uniformly distributed values of the relative phase, which is a first indication that the effect of rephasing is not being observed under the experimental conditions used. Numerical values of the coherence factor $\langle \cos \phi \rangle$ calculated by averaging the cosine of the relative phase distribution for different duration of the rephasing pulse, presented in figure 7.10, are all very close to zero, quantitatively proving the ineffectiveness, under current experimental condition, of the coupling pulse in increasing the coherence of the system. The error bars represents the partial knowledge of the real density distribution resulting from a finite number of measurements, scaling as σ/\sqrt{M} , where σ is the standard deviation of the measured distribution and M is the total number of measurements, never below 44. Possible explanation for this negative result will be provided in the concluding section of this chapter.

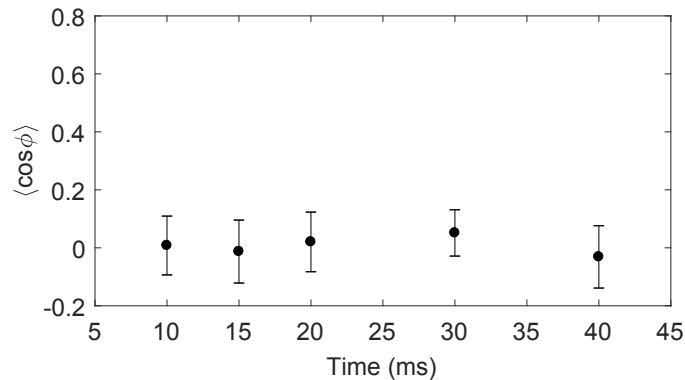


Figure 7.10: Coherence factor obtained by taking the average of the cosine of the phase distribution found in a rephasing experiment with a fast initial $\pi/2$ splitting (polar plot in figure 7.9). The coherence is close to zero, showing no appreciable deviation from a uniformly distributed relative phase.

7.2.2 Adiabatic transfer to 50:50 superposition

In this section we focus on the preparation of a spatially separated two component BEC through the application of a weak coupling pulse that slowly drives half of the particles from state $|1\rangle$ to state $|2\rangle$. Since we could not independently condense each individual state and since the application of a pulse with Rabi frequency $\Omega_r = 2\pi \cdot 1$ kHz leaves the system in a nonequilibrium state that oscillates and takes ≈ 170 ms to separate, by slowly transferring atoms from one state to the other we can obtain a final superposition that has a close resemblance to the actual ground state, greatly suppressed spatial oscillations and can be achieved on a faster timescale. We run simulations for the CGPE with a linear coupling of different strength and different detuning and find unexpected complex dynamics. The dynamics are strongly dependent on the coupling Ω_r and the detuning δ_r . When the coupling is not present we have the usual breathing collective modes and given the particular asymmetry in the intra-species scattering length for rubidium 87 component $|1\rangle$ is pushed to the wings and component $|2\rangle$ in the center. With the coupling strength increased to $\Omega_r \approx 2\pi \cdot 10$, the trend reverses, with component $|2\rangle$ in the wings and $|1\rangle$ in the middle. If the coupling is increased further, with $\Omega_r \approx 2\pi \cdot 30$ Hz, the amplitude of the oscillations decrease to the point that we can consider it a stationary dressed state [126], with very poor time averaged separation.

Immiscibility and spatial separation with an adiabatic transfer

We briefly take a break from experimental measurements and present the result of the simulation for the evolution of a BEC initially in state $|1\rangle$ which is slowly driven by a weak coupling Ω_r . From this simulation we wanted quantitative information about the parameters such as coupling strength, detuning δ_r and evolution time necessary to create an equal superposition that most closely resembled the ground state of a two component BEC. Later in this section, experimental evidence is provided to confirm the prediction of the simulations.

Figure 7.11 shows a simulation for $\Omega_r = 2\pi \cdot 5$ Hz and $\delta_r = -2\pi \cdot 30$ Hz, with $N_{tot} = 3.4 \cdot 10^5$ atoms. The importance of detuning is immediately evident. Due to mean field shift we had to find a value of δ_r that allows for an equal superposition to be created. For the parameters of figure 7.11 only the edges of the clouds are transferred to state $|2\rangle$ and we are always far away from an equal split. Figure 7.12 has the same coupling Ω_r as in figure 7.11, but this time the detuning of $-2\pi \cdot 40$ Hz allows for a much more efficient splitting, creating an almost 50:50 superposition after ≈ 90 ms. The density distribution looks almost identical to the one expected for the ground state, making it a good candidate. However the time required to achieve this condition is somewhat long, and on this timescale dephasing, especially due to losses (we are working with high atom numbers), becomes relevant. (The total population drops from $3.4 \cdot 10^5$ to $2.5 \cdot 10^5$, down by $\approx 30\%$).

Increasing the coupling strength to $\Omega_r = 2\pi \cdot 10$ Hz and with a detuning $\delta_r = 2\pi \cdot 30$ Hz we observed a swap of the density profiles, once again due to detuning allowing coupling on the wings, with $|2\rangle$ on the sides and component $|1\rangle$ in the center (see figure 7.13). This configuration is very different from the ground state, but has the potential advantage of reducing the density of component $|2\rangle$, thus reducing losses in the system (spin relaxation is not suppressed in $|2\rangle$). However this potential advantage is offset by the tendency of component $|1\rangle$ to expand into component $|2\rangle$, making the overlapping time-dependent again. We found conditions that we deemed satisfactory for $\Omega_r = 2\pi \cdot 10$ Hz and $\delta = 2\pi \cdot 40$ Hz, where we obtained a ground state looking axial density distribution after only 30 ms, with very small losses (the population drops only by 8%, figure 7.14). The separation is unfortunately worse than for the actual ground state, but we believed the benefit of suppressed oscillations and reduced waiting time would offset this potential problem. The coefficient χ after 30 ms is ≈ 5 Hz, which is still acceptable.

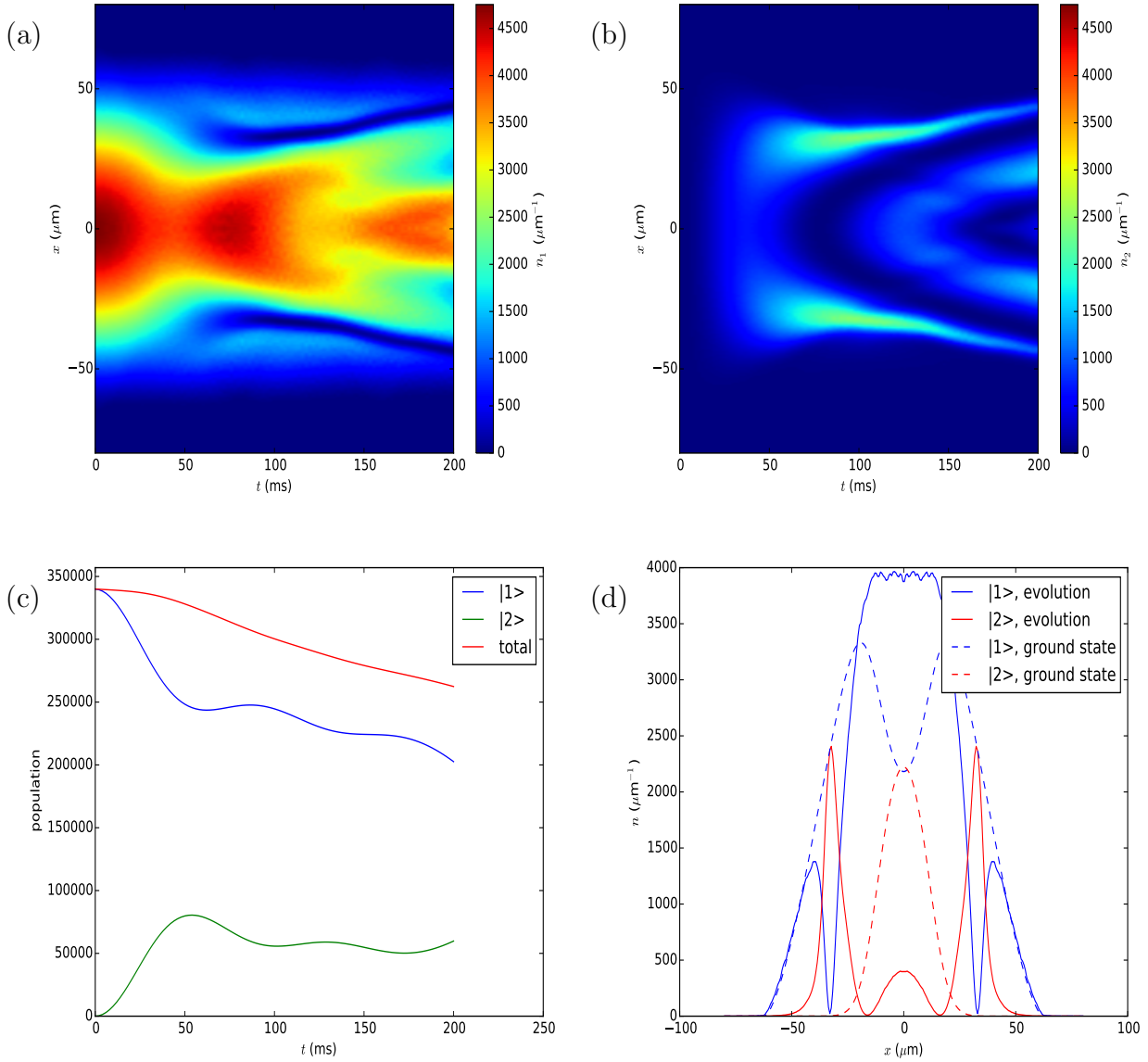


Figure 7.11: **(a)** Axial density evolution for state $|1\rangle$, $\Omega_r = 2\pi \cdot 5$ Hz, $\delta_r = -2\pi \cdot 30$ Hz. **(b)** Axial density evolution for component $|2\rangle$, $\Omega_r = 2\pi \cdot 5$ Hz, $\delta_r = -2\pi \cdot 30$ Hz. **(c)** Evolution of the populations, $N = 3.4 \cdot 10^5$, $\Omega_r = 2\pi \cdot 5$ Hz, $\delta_r = -2\pi \cdot 30$ Hz with losses. Total population in red, component $|1\rangle$ in blue and component $|2\rangle$ in green. **(d)** comparison between the ground state (**dashed lines**) and the state obtained after 100 ms of evolution (**solid lines**). Component $|1\rangle$ is in blue, component $|2\rangle$ is in red.

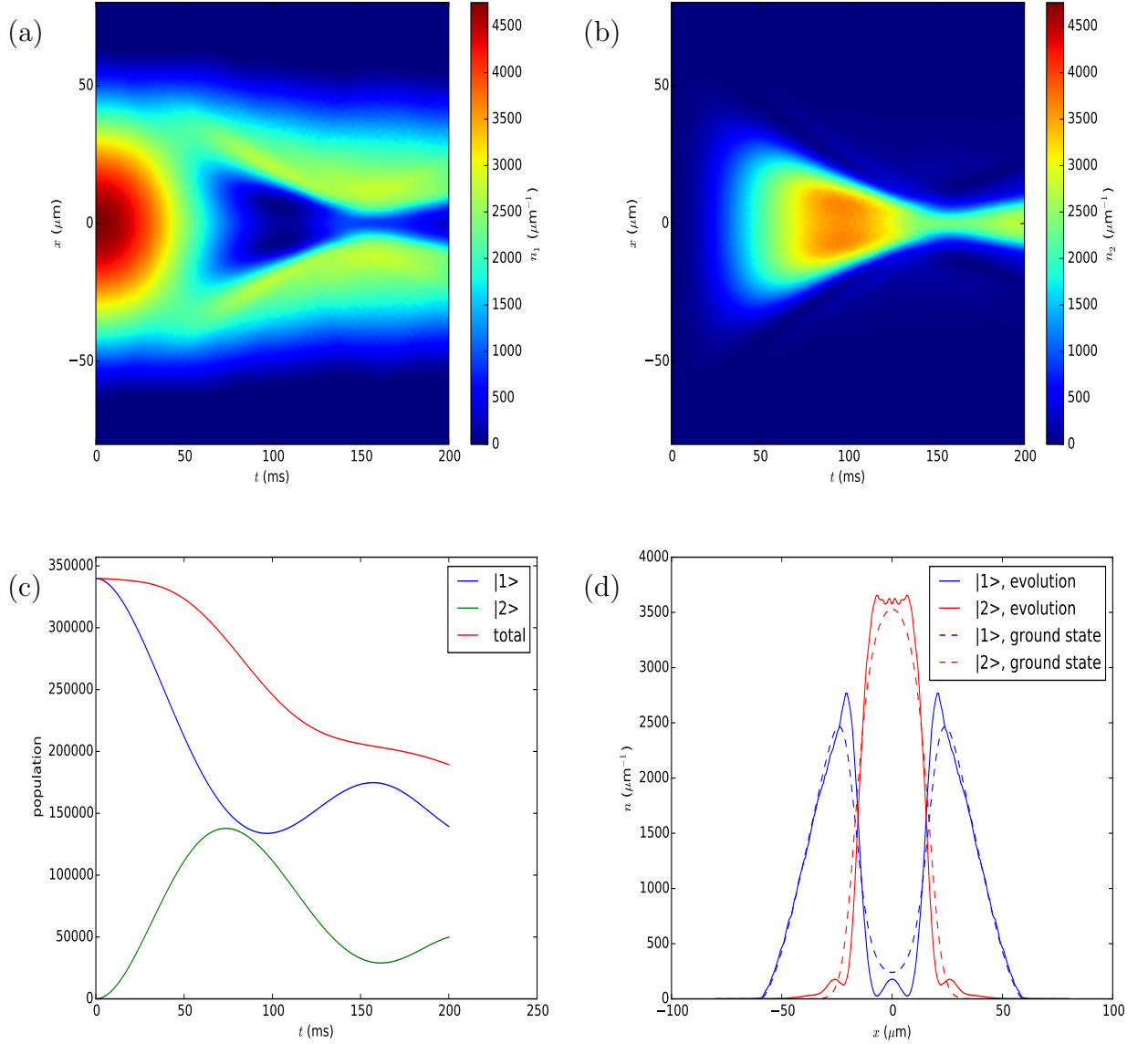


Figure 7.12: (a) Axial density evolution for state $|1\rangle$, $\Omega_r = 2\pi \cdot 5$ Hz, $\delta_r = -2\pi \cdot 40$ Hz. (b) Axial density evolution for component $|2\rangle$, $\Omega_r = 2\pi \cdot 5$ Hz, $\delta_r = -2\pi \cdot 40$ Hz. (c) Evolution of the populations, $N = 3.4 \cdot 10^5$, $\Omega_r = 2\pi \cdot 5$ Hz, $\delta_r = -2\pi \cdot 40$ Hz with losses. Total population in red, component $|1\rangle$ in blue and component $|2\rangle$ in green. (d) Comparison between the ground state (**dashed lines**) and the state obtained after 90 ms of evolution (**solid lines**). Component $|1\rangle$ is in blue, component $|2\rangle$ is in red.

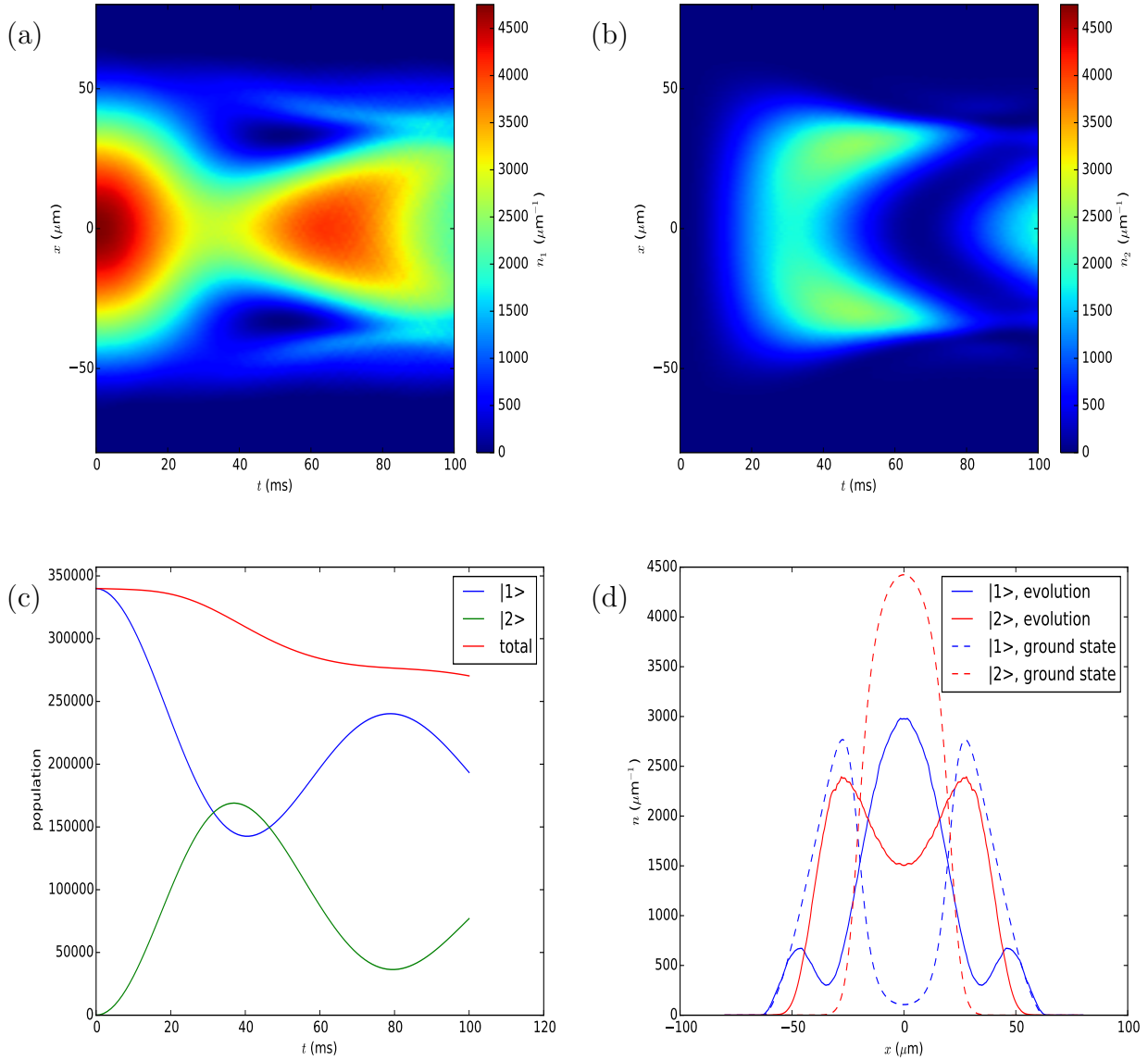


Figure 7.13: **(a)** Axial density evolution for state $|1\rangle$, $\Omega_r = 2\pi \cdot 10$ Hz, $\delta_r = -2\pi \cdot 30$ Hz. **(b)** Axial density evolution for component $|2\rangle$, $\Omega_r = 2\pi \cdot 10$ Hz, $\delta_r = -2\pi \cdot 30$ Hz. **(c)** Evolution of the populations, $N = 3.4 \cdot 10^5$, $\Omega_r = 2\pi \cdot 10$ Hz, $\delta_r = -2\pi \cdot 30$ Hz with losses. Total population in red, component $|1\rangle$ in blue and component $|2\rangle$ in green. **(d)** comparison between the ground state (**dashed lines**) and the state obtained after 40 ms of evolution (**solid lines**). Component $|1\rangle$ is in blue, component $|2\rangle$ is in red.

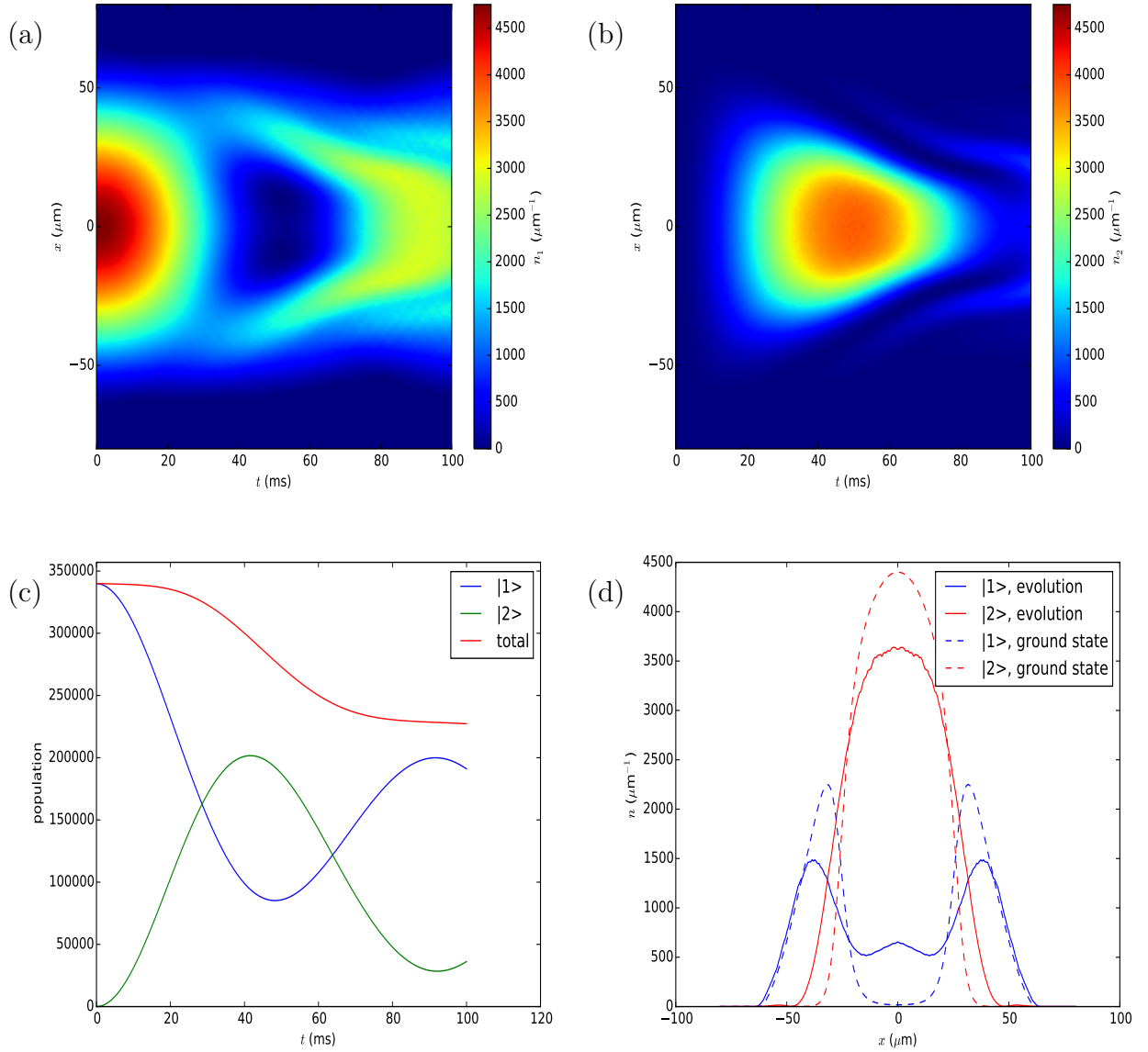


Figure 7.14: **(a)** Axial density evolution for state $|2\rangle$, $\Omega_r = 2\pi \cdot 10$ Hz, $\delta_r = -2\pi \cdot 40$ Hz. **(b)** Axial density evolution for component $|1\rangle$, $\Omega_r = 2\pi \cdot 10$ Hz, $\delta_r = -2\pi \cdot 40$ Hz. **(c)** Evolution of the populations, $N = 3.4 \cdot 10^5$, $\Omega_r = 2\pi \cdot 10$ Hz, $\delta_r = -2\pi \cdot 40$ Hz with losses. Total population in red, component $|1\rangle$ in blue and component $|2\rangle$ in green. **(d)** comparison between the ground state (*dashed lines*) and the state obtained after 28 ms of evolution (*solid lines*). Component $|1\rangle$ is in blue, component $|2\rangle$ is in red.

We run experiments to check if the adiabatic coupling method was indeed able to produce the simulated density patterns and suppress collective oscillations. The trap bottom was set at 3.23 G, the strength of the coupling pulse at $\Omega_r = 2\pi \cdot 10$ Hz and the detuning $\approx -2\pi \cdot 40$ Hz. The detuning has been measured using Ramsey oscillations. For perfectly resonant Ramsey pulses, the frequency of Ramsey oscillations in our typical trap condition and for $2 \cdot 10^5$ atoms is $\approx 2\pi \cdot 15$ Hz, given by collisional shift. The correct field detuning is characterized by a Ramsey frequency $\approx 2\pi \cdot 25$ Hz. This frequency value can be obtained by using a field positively detuned by $2\pi \cdot 10$ Hz or a field negatively detuned by $-2\pi \cdot 55$ Hz. The Ramsey fringes would have the same frequency for both cases. However, in the event of a positively detuned field, increasing its frequency would increase the frequency of the Ramsey oscillations. If the field happens to be negatively detuned, increasing its frequency decreases the frequency of Ramsey oscillations, thus providing an easy way to find the correct detuning. The atoms were subject to the weak coupling field for a minimum of 10 ms to a maximum of 100ms, than immediately released from the trap and imaged after 10 ms time of flight, with both population imaged at the same time using the adiabatic passage method described in chapter 3. The results are displayed in figure 7.15-7.16.

The experimental results follow the simulations quite closely, with component $|2\rangle$ compressing in the middle as expected and component $|1\rangle$ more broadly distributed in the trap. From the images there is a hint of the double structure in component $|1\rangle$, but we were unable to clearly resolve it, the inability attributed to our lack of imaging resolution. The overlap cannot reliably be estimated from measurements, due to the falling time and the additional manipulation involved in the imaging process, forcing us to rely on simulated values. On a side note, our estimate of $3.4 \cdot 10^5$ atoms proved to be too optimistic since we could produce condensates with no more than $2.5 \cdot 10^5$ atoms for this particular experiment, which had the effect of shifting the conditions for acceptable 50:50 superposition and overlap after 40 ms of evolution, compared to 30 ms for $3.4 \cdot 10^5$, as can be seen in figure 7.16. We

identified the conditions at $t=40$ ms as the most desirable and we proceeded to test the absence of collective oscillations for this configuration by holding, without any coupling applied, the atoms for as much as 100 ms and measuring the width of each condensate. While the oscillations were not completely suppressed, they were less intense than with the quick $\pi/2$ pulse (figure 7.18).

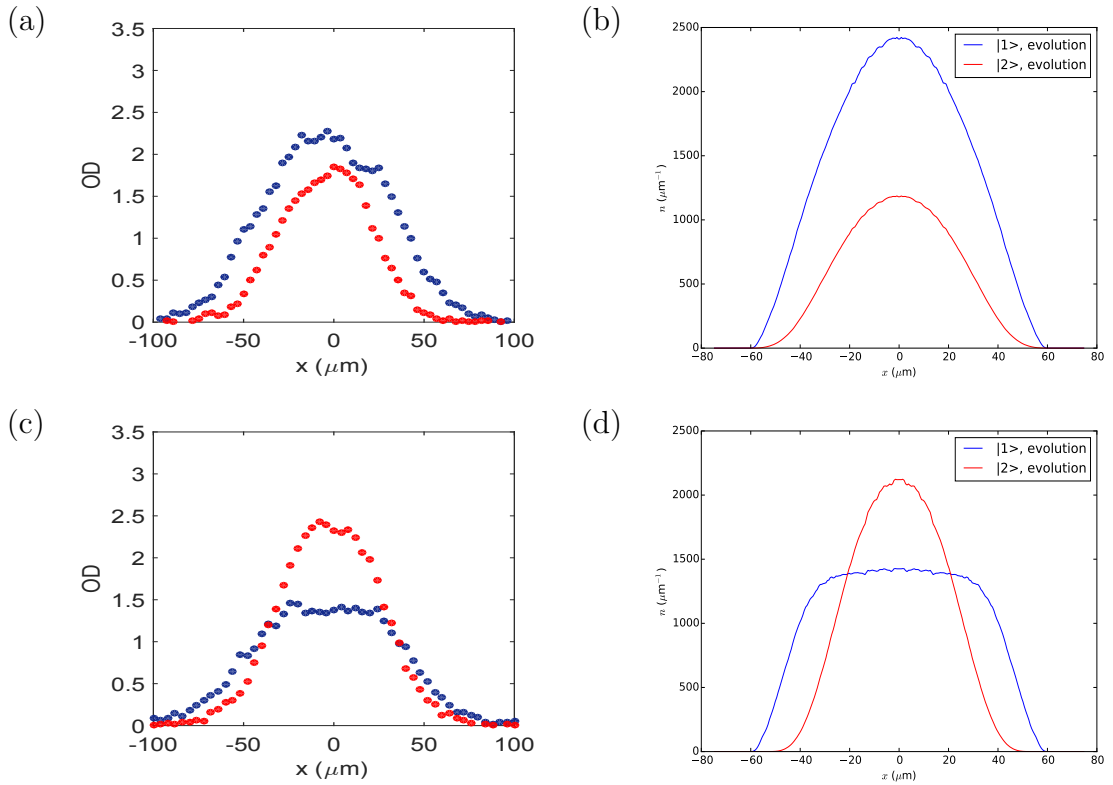


Figure 7.15: Experimentally measured density distributions after (a) $t = 20$ ms, $N_1 = 1.72 \cdot 10^5$, $N_2 = 2.48 \cdot 10^5$, $N_2/(N_1 + N_2) = 30.44\%$ and (c) $t = 30$ ms, for component $|1\rangle$ (**blue dots**) and component $|2\rangle$ (**red dots**). $N_1 = 1.05 \cdot 10^5$, $N_2 = 1.07 \cdot 10^5$, $N_2/(N_1 + N_2) = 50.38\%$. (b,d) Theoretically simulated density distribution after $t = 20$ ms and $t = 30$ ms, $N = 2.4 \cdot 10^5$. Component $|1\rangle$ is in blue and component $|2\rangle$ is in red. The Rabi frequency of the adiabatic coupling is $\Omega_r = 2\pi \cdot 10$ Hz, detuning is kept at $\delta = -2\pi \cdot 40$ Hz. Trap bottom is set at $B_0 = 3.23$ G while trap frequencies have the typical values of $2\pi \cdot 11$ Hz in the axial direction and $2\pi \cdot 97$ Hz in the radial direction.

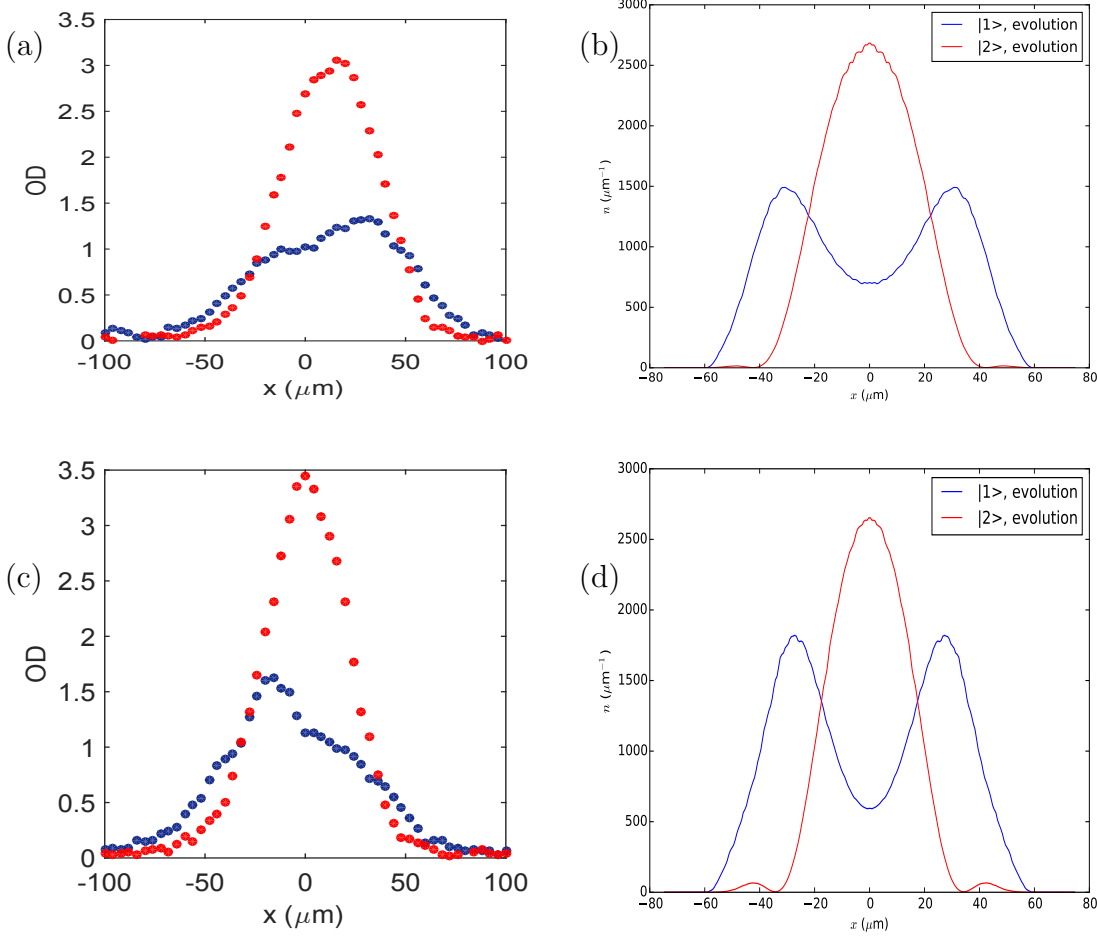


Figure 7.16: Experimentally measured density distributions after (a) $t = 40$ ms, $N_1 = 8.13 \cdot 10^4$, $N_2 = 1.17 \cdot 10^5$, $N_2/(N_1 + N_2) = 59.01\%$ and (c) $t = 50$ ms, for component $|1\rangle$ (blue dots) and component $|2\rangle$ red dots. $N_1 = 8.34 \cdot 10^4$, $N_2 = 1.15 \cdot 10^5$, $N_2/(N_1 + N_2) = 57.59\%$. (b,d) Theoretically measured density distribution after $t = 40$ ms and $t = 50$ ms, $N = 2.4 \cdot 10^5$. Component $|1\rangle$ is in blue and component $|2\rangle$ is in red. The Rabi frequency of the adiabatic coupling is $\Omega_r = 2\pi \cdot 10$ Hz, detuning is kept at $\delta = -2\pi \cdot 40$ Hz. Trap bottom is set at $B_0 = 3.23$ G while trap frequencies have the typical values of $2\pi \cdot 11$ Hz in the axial direction and $2\pi \cdot 97$ Hz in the radial direction.

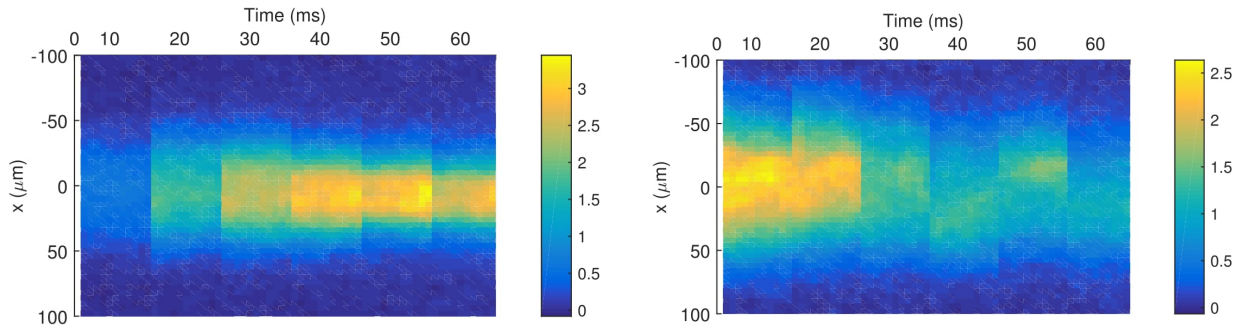


Figure 7.17: Experimentally measured spatial evolution of the optical density of component $|2\rangle$ (**left**) and component $|1\rangle$ (**right**)

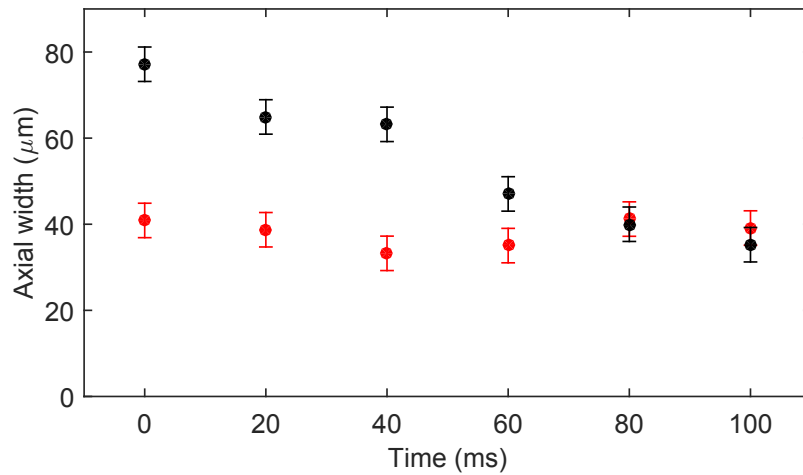


Figure 7.18: Axial oscillation widths for state $|2\rangle$ after the application of a quick $\pi/2$ preparation pulse (**black**) and an adiabatic $\pi/2$ pulse (**red**). For the adiabatic pulse case the time has to be understood as waiting time after the initial 40 ms required to create the superposition; the oscillations, while not absent, are strongly reduced.

Rephasing with an adiabatic coupling

This experiment was performed in a similar way to the fast $\pi/2$ splitting described in section 7.2.1, the only difference being the Rabi frequency of the initial pulse, set at $\Omega_r = 2\pi \cdot 10$ Hz, detuned by $\delta_r = -2\pi \cdot 40$ Hz, and the higher initial atom number,

with initial N_{tot} ranging from $2 \cdot 10^5$ to $3 \cdot 10^5$ instead of 10^5 . The total number of particles was increased to compensate for the generally smaller separation achievable with this method (the higher the total number of particles the more the components will push apart). After the required number of particles has been condensed, they were slowly transferred to a 50:50 superposition of state $|1\rangle$ and state $|2\rangle$ over 30 ms. The phase ϕ_1 of this initial preparation pulse was again varied, from shot to shot, between 0 and 2π , creating a uniform distribution. At this point the preparation coupling was switched off and we waited for 20 ms. The suppression of oscillations allowed us to consider the spatial distribution stationary during this waiting time. We then sent the rephasing coupling pulse, with a Rabi frequency $\Omega = 2\pi \cdot 75$ Hz and a duration between 20 and 40 ms, with a phase $\phi_2 \neq \phi_1$ arbitrarily chosen at the beginning of the experiment and kept constant afterwards. The observable measured was once again P_z , and from the experimental data points we extracted $\langle \cos \phi \rangle$ and its distribution using the same method outlined in section 7.2.1. The interference contrast \mathcal{V} , calculated as the amplitude of a sinusoidal fit of a Ramsey fringe in the experimental conditions had an average value of 0.3, mostly due to poor overlap and coherence issues. A key difference from the fast $\pi/2$ experiment lies in the fact that we are now using two Ramsey pulses of different strength, the first being slow and the second being fast. This forces us to use two different RF generator, since the amplitude is manually set at the beginning of the experiment for each generator and cannot be changed during the experiment. The RF generators are both clocked and synchronized by the MW generator internal 10 MHz quartz oscillator, but the coherence of the system is not as good as the coherence achieved after 50 ms for the fast $\pi/2$ experiment using a single RF generator, being equal to 0.8 instead of 0.91 (see figure 7.19).

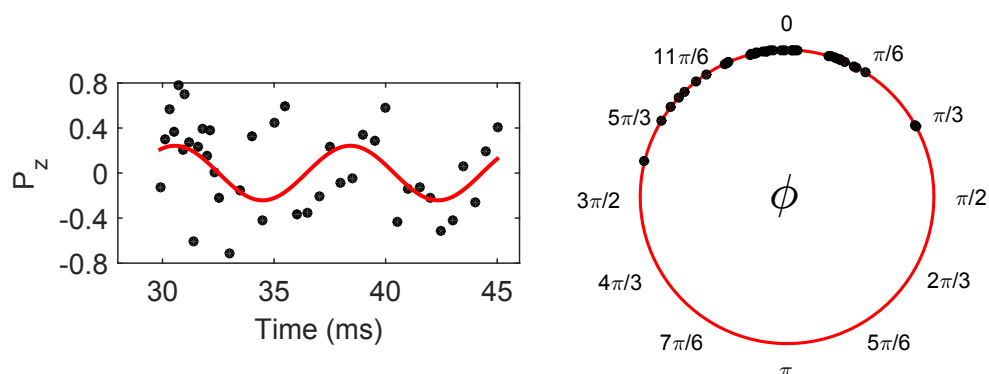


Figure 7.19: Ramsey interferometry in time domain used to measure the coherence of the adiabatic coupling experiment. The red line is a sinusoidal fit while the black dots are experimental points. The Polar plot provides a graphical representation of the coherence of the system and is constructed by first recovering the phase of each experimental point using equation (7.3) and then calculating the phase shift with equation (7.6). The coherence is degraded by the imperfect synchronization of the two RF generators used to produce the initial slow preparation pulse and the final fast reading pulse. $\langle \cos \phi \rangle \approx 0.8$ after 30 ms of free evolution.

Typical examples of Ramsey fringes as they are acquired in the experiment along with polar plot showing the relative phase distribution are shown in figure 7.20, while the coherence factor, calculated as the average of the cosine of the relative phase distribution plotted in figure 7.20, is displayed in figure 7.21. The results again show no appreciable contribution coming from the rephasing pulse to changing the distribution of the relative phase. The rephasing is once again undetectable in the experimental conditions.

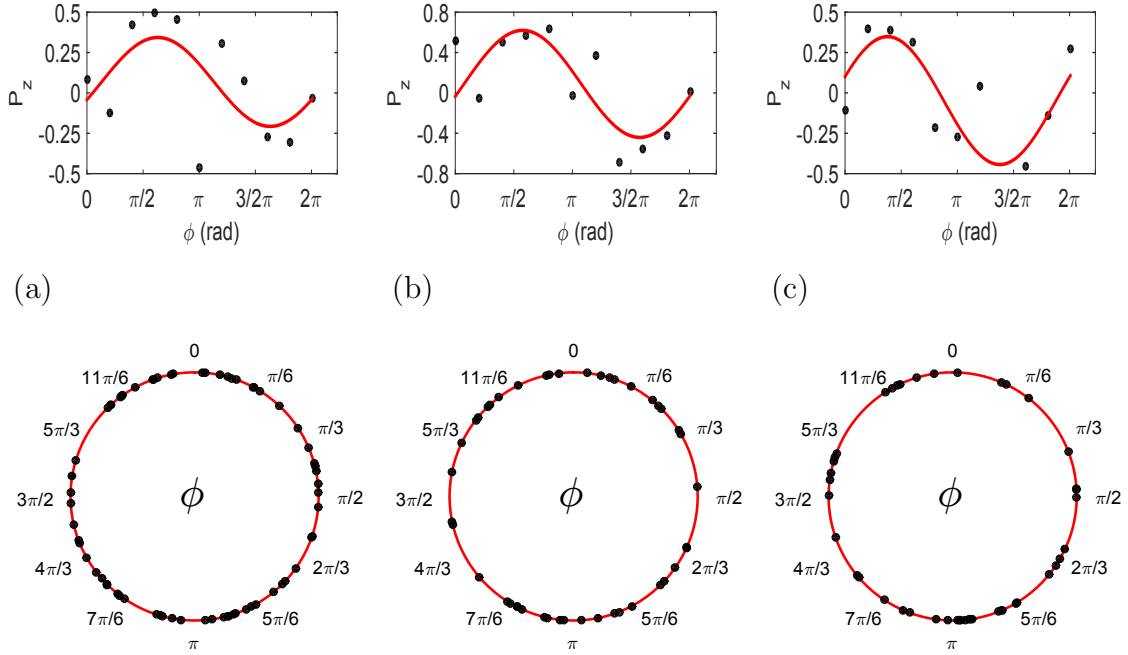


Figure 7.20: **(a,b,c)** Ramsey fringes acquired by varying the phase of the second Ramsey pulse after slowly transferring 50% of the population from state $|1\rangle$ to state $|2\rangle$ over 50 ms and the additional application of a rephasing coupling with duration $t = 20$ ms **(a)**, $t = 30$ ms **(b)** and $t = 40$ ms **(c)**. The red line is a sinusoidal fit while the black dots are experimental points. The circumferences are polar plots showing the relative phase distribution corresponding to at least 40 measurements for each duration of the rephasing pulse. The uniformity of the distribution suggests absence of rephasing.

7.3 Conclusions

We were unable to observe any significant change from the expected null value of in the coherence factor $\langle \cos \phi \rangle$, corresponding to a uniform distribution of relative phase, in experiments when a weak coupling was applied to an equal superposition of atoms in the two hyperfine states $|F = 1, m_F = -1\rangle$ and $|F = 2, m_F = +1\rangle$.

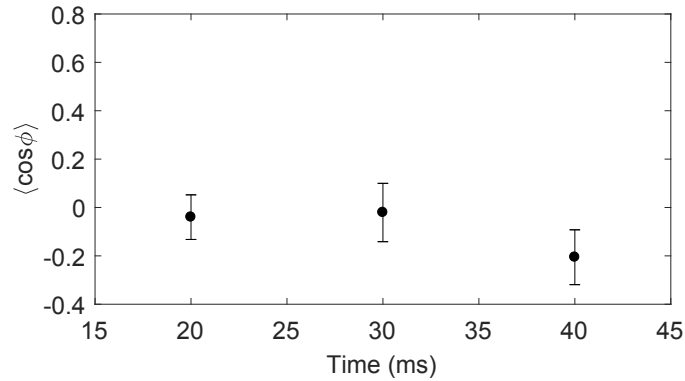


Figure 7.21: Coherence factor obtained by taking the average of the cosine of the phase distribution found in a rephasing experiment with an adiabatic coupling (polar plot in figure 7.20). The coherence is close to zero for the three different duration of the rephasing pulse, showing no appreciable deviation from a uniformly distributed relative phase.

In these experiments the way the relative phase is distributed can be interpreted as measurements of the coherence of the condensate. This is because the condensate has a well defined relative phase in each iteration of the experiment, but every iteration uses a different relative phase of the coherent pulses used to manipulate the BEC in a Ramsey sequence. This should create a uniform distribution of relative phases over many repetitions, with zero average. This condition is the closest we could get to "initial incoherence" after we abandoned the independent condensation strategy for the reasons outlined in section 7.1. The theoretical framework presented in chapter 6 suggests that even for this case, the application of a weak coupling should change the distribution of the relative phase and consequently the coherence factor compared to the case when no coupling is applied. The weak coupling is expected to shift the coherence factor away from zero. These effects are to be associated with a narrower distribution of possible phases, thus justifying the term "rephasing", since the weak coupling is forcing coherence by effectively eliminating some phase configurations in the "initially incoherent" (on average) system where all phase configurations are

equally probable. However, as already mentioned, no change has been observed in experiments performed with this weak coupling. In what follows we will present some possible explanations for this negative result:

Poor initial coherence

The measurements on the coherence have shown that the system is only partially coherent before the application of the rephasing pulse. The reason for the decoherence is easily found for the fast $\pi/2$ rephasing experiment, since the system has to evolve for 150 ms before the optimal condition for rephasing are met. For the adiabatic transfer to a 50:50 superposition experiment the decoherence comes through imperfect synchronization of the RF generators needed to produce the field required to perform the experiments. In both cases the coherence factor $\langle \cos \phi \rangle$ acquires similar values, 0.74 for the fast $\pi/2$ and 0.8 for the adiabatic preparation. The experiment we performed relied on the creation of a uniformly distributed relative phase between the vector representing the state of the system and the Ramsey pulses used to manipulate it, achieved by assuming the state vector static and by changing the relative phase between the Ramsey pulses. The vector was allowed to move, in our model, only when the weak rephasing coupling was applied, and the motion was expected to increase the likelihood of finding the state in phase with the coupling pulse. The rotation speed was therefore only dependent on the relative phase between the pulses, which replaces in our experiment the relative phase between the condensate used in the theory, since now, due to the fact that we are not independently condensing, but coherently transferring, each state has one and the same phase. This is consistent with the theoretical explanation given in chapter 6. It was the relative phase between the condensates that determined how far away from the equator the state would have gone once the constant phased weak coupling was to be applied, in turn determining the state's rotation speed, only now the roles between coupling

and state are reversed. It is therefore not surprising that, if the initial phase of the system is random, the effect we are trying to detect gets hidden and smeared out. This is because decoherence acts to create a uniform distribution of relative phases and rephasing does exactly the opposite, departing from it toward a more peaked one. This is just a qualitative analysis, since we did not run simulations for a less than ideal coherent system and we do not know if the level of coherence found in our system is enough to destroy rephasing or it only reduces its effect and changes its characteristic time.

The system is not quenched by the rephasing pulse

The theoretical background presented in chapter 6 assumed the system to be in the ground state of a gapless Hamiltonian, which was a condition satisfied by the independent condensation approach. Then, the sudden quench represented by the weak rephasing coupling would have opened up a gap, exciting non-adiabatic dynamics in the system. The coupling had to be weak, i.e. less than the chemical potential, to keep the newly formed Josephson Junction in the Josephson regime and avoiding the Rabi regime that would have suppressed rephasing. Unfortunately, creating a superposition by splitting the condensate with a Ramsey $\pi/2$ pulse with $\omega = 2\pi \cdot 1$ kHz effectively quenches the system much before the actual weak rephasing pulse is applied, opening the gap effectively at $t=0$, when only a single component is present and furthermore the pulse strength does not satisfy the condition of being much weaker than the chemical potential. The same is true for the adiabatic transfer to a 50:50 superposition, with the difference that the pulse does satisfy the weak condition and the system adiabatically evolves to a new state but now the rephasing pulse can be seen as a mere continuation of the preparation pulse itself and there is nothing "sudden" and the gap is opened when we only have a single component, clearly not representing the Hamiltonian described by equation 6.31. These considerations cast a doubt on the observability of the dynamics,

but more theoretical analysis is required for a final answer and we did not have the resources to carry it out.

Rephasing happens on a longer timescale

A possibility might be that rephasing is actually observable in our set of experiments, but it happens on a longer time scale. This might come from errors in the predictions of the rephasing period as done in chapter 6 or simply through the neglect of relevant effects that might increase the period itself. We did not make observations for longer than 40 ms after the application of the rephasing pulse, mostly due to considerations regarding the extent of the overlapping, which is time dependent, asymmetric losses, heavily affecting state $|2\rangle$ and decoherence, especially in the quick $\pi/2$ pulse case, that required a preliminary evolution time of 150 ms.

Losses reduce the observability

We mostly focused our attention on how losses influence the oscillation dynamics and the overlapping between the two components. but there is another aspect of losses that should be analyzed: losses cause the Bloch vector to move away from the equator, thus modifying the subsequent evolution, as shown in figure 7.22. From a qualitative point of view, the fact that our initial condition is not represented by a circumference sitting at the equator removes a symmetry from the problem and is expected to reduce the maximum value of $\langle \cos \phi \rangle$ and possibly affect the period of oscillations as well, since the equation of motion in the new initial conditions has a non trivial dependence on the initial conditions themselves, the rephasing coupling and the nonlinear coefficient. Quantitative information can only come from additional simulation for initial conditions different to the equal split.

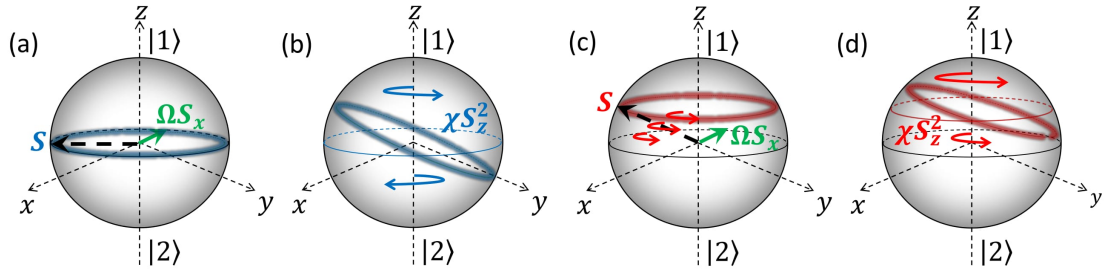


Figure 7.22: Bloch sphere representation of a rephasing sequence for an even (**a,b**) and an uneven (**c,d**) superposition of atoms in state $|1\rangle$ and $|2\rangle$. The details of the evolution have been explained in the caption of figure 7.3. Here the attention should be directed to the fact that asymmetric losses takes the mean spin vector S away from the equatorial plane. When an equal superposition is produced, the mean spin vector S starts to rotate around the z -axis only after the rephasing coupling has been applied, since $S_z = 0$ on the equatorial plane. When asymmetric losses are present, the vector starts to rotate independently of the application of the coupling. However this can be seen as just an offset, since all the points in the relative phase distribution will rotate counterclockwise by the same amount, which is given by the extent of the losses in the time between the preparation of the superposition and the application of the rephasing coupling. For this reason, rephasing is expected to happen anyway, since what matters for rephasing is the difference in rotational speed of points that occupy different positions on the circumference representing relative phase after it has been rotated by the rephasing pulse. In this regard points further away from the equator still rotate faster than points closer to the equator, but this time all the points rotate in the same direction, since they are all in the northern hemisphere and we have lost the symmetry that made points at the same distance from the equator but on opposite hemispheres rotate with the same speed. Furthermore the dynamics are made more complicated by the inversion in the rotation that the points will experience after crossing the equatorial plane. We do not have quantitative results, but from a qualitative point of view a departure from an even superposition causes a decrease in the amount of rephasing observable.

CHAPTER 8

Summary and future directions

In this thesis we have described the theoretical justification for the existence of universal rephasing dynamics in a Josephson Junction originally proposed by Dalla Torre et al. [2] for a double well (external Josephson junction) and by us extended to the two-component BEC case (internal Josephson junction). Chapter 6 provides an introduction to the physics of the Josephson junction, either internal or external, presents the main results obtained by Dalla Torre et al. and details the calculations needed to extend the description to a two-component system. It also presents our simulations of the universal rephasing dynamics for an internal Josephson junction that appear to be very similar to the results obtained in [2]. The chapter deals extensively with a major difference from Dalla Torre's double well model, the nonlinear coefficient χ . CGPE simulations had to be performed to make predictions on the magnitude of this crucial parameter, whose strength depends on the overlapping of the wavefunctions as well as the derivative of the chemical potentials, both evolving in a complex way.

We have attempted to detect the rephasing experimentally, using different approaches described in depth in chapter 7. The first approach used independent condensation of two hyperfine states in the same magnetic trap to create an initially incoherent

(over many repetitions) system, to which the rephasing sequence was to be applied. Difficulty related to the purity and the size of the condensates created with this method forced us to abandon it in favor of a different approach we called "engineered phase rephasing". At its core this experiment is a Ramsey interferometry sequence in phase domain, where the relative phase of the Ramsey pulses changes from realization to realization while the condensate superposition's phase remains constant, barring decoherence effects. We artificially "engineer" a uniform relative phase distribution, replacing nature's spontaneous symmetry breaking process during condensation, which also have a uniformly distributed probability of picking any phase between 0 and 2π . The rephasing, triggered by the application of a weak coupling in the form of an external microwave field, should have caused this distribution to shift away from being uniform, with an increased probability for the system to be in phase with the second Ramsey pulse (relative phase $\phi = 0$). We did not observe any change in the coherence factor $\langle \cos \phi \rangle$, which measure, as the name suggests, the degree of coherence of the system. For all the experimental points taken, corresponding to different duration of the rephasing coupling, the coherence factor was very close to zero, signifying uniformity in the relative phase distribution and hence incoherence. The coherence factor, from theoretical simulations, was expected to increase to $\langle \cos \phi \rangle \approx 0.7$ and then to oscillate around a mean value $\langle \cos \phi \rangle \approx 0.4$, but none of this behavior was observed. We provided possible explanation to justify the fact that we were not able to observe such phenomena in the end section of chapter 7.

It is clear however that two-component BECs are not the optimal system to detect such dynamics and the double well system originally proposed is in the opinion of the author of this thesis is far better suited. The reason is simple: by forcing the spatial separation of the two components and subsequent increase of the interaction parameter in the two component BEC in order to replace the double well potential as a way to control the optimal conditions for rephasing, we are giving away a lot of flexibility and we are introducing additional decohering effects mostly due to the

long waiting time. What can be done immediately after condensation in a double well, needs at least 150 ms of evolution in a two-component BEC experiment , with the corollary of losses, phase diffusion and lost contrast. The level of control over the nonlinear coefficient χ , fundamental in determining the rephasing characteristic time, is markedly inferior than the tunneling strength that takes its place in the double well case. The coefficient χ is continuously changing, even during rephasing, and its determination requires accurate knowledge of the state of the system just before the coupling is applied. On the contrary, the tunneling strength is controlled by the experimenter and kept constant throughout the measurements.

The rephasing dynamics expected from the theoretical model proved to be undetectable under the experimental conditions. However the numerical simulations were run under ideal conditions, without taking into account potentially relevant decoherence effects. Additionally, the inability to condense directly in the two states without a substantial thermal fraction forced us to explore different techniques, which do not satisfy the sudden quench condition, casting a shadow on the possibility to use the simulations to predict the outcome of the experiment.

Previous experiments at Swinburne have identified local oscillator instability as the dominant source of decoherence limiting the coherence time of Ramsey measurements. In chapter 5 we provided evidence on the implementation of a new microwave system that reduces technical noise below the quantum limit previously estimated by Egorov and Opanchuk. The coherence time of a thermal cloud in a Ramsey interferometer has been extended to 12 seconds. The enhanced stability of the system can be exploited in future experiments requiring high precision measurements and long phase accumulation time.

Bibliography

- [1] Bogdan opanchuk. *Quasiprobability methods in quantum interferometry of ultracold matter*. PhD thesis, Swinburne university of technology, Melbourne, Australia, 2014. (Cited on pages xiv, 69, and 70.)
- [2] Emanuele G. Dalla Torre, Eugene Demler, and Anatoli Polkovnikov. Universal rephasing dynamics after a quantum quench via sudden coupling of two initially independent condensates. *Phys. Rev. Lett.*, 110:090404, Feb 2013. (Cited on pages xv, 3, 6, 98, 104, 106, 110, and 153.)
- [3] P. Kapitza. Viscosity of liquid helium below the λ -point. *Nature*, 141(3558):74–74, jan 1938. (Cited on page 1.)
- [4] J. F. Allen and A. D. Misener. Flow phenomena in liquid helium II. *Nature*, 142(3597):643–644, oct 1938. (Cited on page 1.)
- [5] S. N. Bose. Plancks gesetz und lichtquantenhypothese. *Zeitschrift für Physik*, 26(1):178–181, dec 1924. (Cited on page 1.)
- [6] F. London. The λ -phenomenon of liquid helium and the Bose-Einstein degeneracy. *Nature*, 141(3571):643–644, apr 1938. (Cited on page 1.)
- [7] M. H. Anderson, J. R. Ensher, M. R. Matthews, C. E. Wieman, and E. A. Cornell. Observation of Bose-Einstein condensation in a dilute atomic vapor. *Science*, 269(5221):198–201, jul 1995. (Cited on page 2.)

-
- [8] C. C. Bradley, C. A. Sackett, J. J. Tollett, and R. G. Hulet. Evidence of Bose-Einstein condensation in an atomic gas with attractive interactions. *Phys. Rev. Lett.*, 75:1687–1690, Aug 1995. (Cited on page 2.)
- [9] K. B. Davis, M. O. Mewes, M. R. Andrews, N. J. van Druten, D. S. Durfee, D. M. Kurn, and W. Ketterle. Bose-Einstein condensation in a gas of sodium atoms. *Phys. Rev. Lett.*, 75:3969–3973, Nov 1995. (Cited on page 2.)
- [10] M. R. Andrews. Observation of interference between two Bose condensates. *Science*, 275(5300):637–641, jan 1997. (Cited on page 2.)
- [11] J. R. Abo-Shaeer, C. Raman, J. M. Vogels, and W. Ketterle. Observation of vortex lattices in Bose-Einstein condensates. *Science*, 292(5516):476–479, apr 2001. (Cited on page 2.)
- [12] S. Burger, K. Bongs, S. Dettmer, W. Ertmer, K. Sengstock, A. Sanpera, G. V. Shlyapnikov, and M. Lewenstein. Dark solitons in Bose-Einstein condensates. *Phys. Rev. Lett.*, 83:5198–5201, Dec 1999. (Cited on page 2.)
- [13] J. Denschlag. Generating solitons by phase engineering of a Bose-Einstein condensate. *Science*, 287(5450):97–101, jan 2000. (Cited on page 2.)
- [14] L. Khaykovich. Formation of a matter-wave bright soliton. *Science*, 296(5571):1290–1293, may 2002. (Cited on page 2.)
- [15] Kevin E. Strecker, Guthrie B. Partridge, Andrew G. Truscott, and Randall G. Hulet. Formation and propagation of matter-wave soliton trains. *Nature*, 417(6885):150–153, may 2002. (Cited on page 2.)
- [16] Markus Greiner, Olaf Mandel, Tilman Esslinger, Theodor W. Hänsch, and Immanuel Bloch. Quantum phase transition from a superfluid to a Mott insulator in a gas of ultracold atoms. *Nature*, 415(6867):39–44, jan 2002. (Cited on pages 2 and 62.)

-
- [17] E. P. Gross. Structure of a quantized vortex in boson systems. *Il Nuovo Cimento*, 20(3):454–477, may 1961. (Cited on page 2.)
- [18] L. P. Pitaevskii. Vortex lines in an imperfect Bose gas. *Sov. Phys. JEPT.*, 13(2):451454, 1961. (Cited on page 2.)
- [19] S. De Palo, C. Castellani, C. Di Castro, and B. K. Chakraverty. Effective action for superconductors and BCS-Bose crossover. *Phys. Rev. B*, 60:564–573, Jul 1999. (Cited on page 2.)
- [20] D. Rozas, C. T. Law, and Jr. G. A. Swartzlander. Propagation dynamics of optical vortices. *Journal of the Optical Society of America B*, 14(11):3054, nov 1997. (Cited on page 2.)
- [21] M. Greiner, O. Mandel, T. Esslinger, T. W. Hänsch, and I. Bloch. Quantum phase transition from a superfluid to a Mott insulator in a gas of ultracold atoms. *Nature*, 415:39–44, January 2002. (Cited on page 2.)
- [22] I. Bloch. Ultracold quantum gases in optical lattices. *Nature Physics*, 1:23–30, October 2005. (Cited on page 2.)
- [23] W. C. Stwalley. Stability of Spin-Aligned Hydrogen at Low Temperatures and High Magnetic Fields: New Field-Dependent Scattering Resonances and Predissociations. *Physical Review Letters*, 37:1628–1631, December 1976. (Cited on page 2.)
- [24] E. Tiesinga, B. J. Verhaar, and H. T. C. Stoof. Threshold and resonance phenomena in ultracold ground-state collisions. *Phys. Rev. A*, 47:4114–4122, May 1993. (Cited on page 2.)
- [25] C. J. Myatt, E. A. Burt, R. W. Ghrist, E. A. Cornell, and C. E. Wieman. Production of two overlapping Bose-Einstein condensates by sympathetic cooling. *Phys. Rev. Lett.*, 78:586–589, Jan 1997. (Cited on page 3.)

- [26] M. R. Matthews, D. S. Hall, D. S. Jin, J. R. Ensher, C. E. Wieman, E. A. Cornell, F. Dalfovo, C. Minniti, and S. Stringari. Dynamical response of a Bose-Einstein condensate to a discontinuous change in internal state. *Phys. Rev. Lett.*, 81:243–247, Jul 1998. (Cited on page 3.)
- [27] Norman F. Ramsey. A molecular beam resonance method with separated oscillating fields. *Physical Review*, 78(6):695–699, jun 1950. (Cited on page 3.)
- [28] D. S. Hall, M. R. Matthews, C. E. Wieman, and E. A. Cornell. Measurements of relative phase in two-component Bose-Einstein condensates. *Phys. Rev. Lett.*, 81:1543–1546, Aug 1998. (Cited on pages 3 and 64.)
- [29] A. Sinatra and Y. Castin. Binary mixtures of Bose-Einstein condensates: Phase dynamics and spatial dynamics. *The European Physical Journal D - Atomic, Molecular and Optical Physics*, 8(3):319–332, feb 2000. (Cited on pages 3 and 62.)
- [30] A. Sinatra, Y. Castin, and E. Witkowska. Coherence time of a Bose-Einstein condensate. *Physical Review A*, 80(3), sep 2009. (Cited on pages 3 and 67.)
- [31] Julian Grond, Ulrich Hohenester, Igor Mazets, and Jörg Schmiedmayer. Atom interferometry with trapped Bose-Einstein condensates: impact of atom-atom interactions. *New Journal of Physics*, 12(6):065036, 2010. (Cited on pages 3 and 62.)
- [32] M. Gustavsson, E. Haller, M. J. Mark, J. G. Danzl, G. Rojas-Kopeinig, and H.-C. Nägerl. Control of interaction-induced dephasing of Bloch oscillations. *Phys. Rev. Lett.*, 100:080404, Feb 2008. (Cited on page 3.)
- [33] C. Deutsch, F. Ramirez-Martinez, C. Lacroûte, F. Reinhard, T. Schneider, J. N. Fuchs, F. Piéchon, F. Laloë, J. Reichel, and P. Rosenbusch. Spin self-rephasing and very long coherence times in a trapped atomic ensemble. *Phys. Rev. Lett.*, 105:020401, Jul 2010. (Cited on pages 3, 85, and 86.)

- [34] L. Pitaevskii and S. Stringari. Thermal vs quantum decoherence in double well trapped Bose-Einstein condensates. *Physical Review Letters*, 87(18), oct 2001. (Cited on pages 3 and 107.)
- [35] Anatoli Polkovnikov, Krishnendu Sengupta, Alessandro Silva, and Mukund Vengalattore. Colloquium. *Rev. Mod. Phys.*, 83:863–883, Aug 2011. (Cited on page 3.)
- [36] T W B Kibble. Topology of cosmic domains and strings. *Journal of Physics A: Mathematical and General*, 9(8):1387–1398, aug 1976. (Cited on page 4.)
- [37] W. H. Zurek. Cosmological experiments in superfluid helium? *Nature*, 317(6037):505–508, oct 1985. (Cited on page 4.)
- [38] Michael Kolodrubetz, Bryan K. Clark, and David A. Huse. Nonequilibrium dynamic critical scaling of the quantum Ising chain. *Phys. Rev. Lett.*, 109:015701, Jul 2012. (Cited on page 4.)
- [39] C. De Grandi, A. Polkovnikov, and A. W. Sandvik. Universal nonequilibrium quantum dynamics in imaginary time. *Phys. Rev. B*, 84:224303, Dec 2011. (Cited on page 4.)
- [40] C. Karrasch, J. Rentrop, D. Schuricht, and V. Meden. Luttinger-liquid universality in the time evolution after an interaction quench. *Phys. Rev. Lett.*, 109:126406, Sep 2012. (Cited on page 4.)
- [41] Lorenzo Campos Venuti and Paolo Zanardi. Universality in the equilibration of quantum systems after a small quench. *Phys. Rev. A*, 81:032113, Mar 2010. (Cited on page 4.)
- [42] E V Albano, M A Bab, G Baglietto, R A Borzi, T S Grigera, E S Loscar, D E Rodriguez, M L Rubio Puzzo, and G P Saracco. Study of phase transitions from short-time non-equilibrium behaviour. *Reports on Progress in Physics*, 74(2):026501, 2011. (Cited on page 4.)

- [43] Yun Li, P. Treutlein, J. Reichel, and A. Sinatra. Spin squeezing in a bimodal condensate: spatial dynamics and particle losses. *The European Physical Journal B*, 68(3):365–381, Jan 2009. (Cited on pages 4, 64, 76, and 111.)
- [44] M. Egorov, B. Opanchuk, P. Drummond, B. V. Hall, P. Hannaford, and A. I. Sidorov. Measurement of s -wave scattering lengths in a two-component Bose-Einstein condensate. *Phys. Rev. A*, 87:053614, May 2013. (Cited on pages 4, 11, and 111.)
- [45] Robert Graham and Dan Walls. Collective excitations of trapped binary mixtures of Bose-Einstein condensed gases. *Phys. Rev. A*, 57:484–487, Jan 1998. (Cited on pages 4, 112, and 114.)
- [46] B. D. Esry, Chris H. Greene, James P. Burke, Jr., and John L. Bohn. Hartree-Fock theory for double condensates. *Phys. Rev. Lett.*, 78:3594–3597, May 1997. (Cited on pages 4, 112, and 114.)
- [47] L.P. Pitaevskii and S. Stringari. *Bose-Einstein Condensation*. International Series of Monographs on Physics. Clarendon Press, 2003. (Cited on pages 5, 10, 11, and 12.)
- [48] Russell anderson. *Nonequilibrium dynamics and relative phase evolution of two-component Bose-Einstein condensates*. PhD thesis, Swinburne university of technology, Melbourne, Australia, 2009. (Cited on pages 6, 37, and 38.)
- [49] C. J. Pethick and H. Smith. *Bose-Einstein Condensation in Dilute Gases*. Cambridge University Press (CUP), 2008. (Cited on pages 10, 12, and 85.)
- [50] J. Williams, R. Walser, J. Cooper, E. Cornell, and M. Holland. Nonlinear Josephson-type oscillations of a driven, two-component Bose-Einstein condensate. *Phys. Rev. A*, 59:R31–R34, Jan 1999. (Cited on pages 10 and 104.)
- [51] E. A. Burt, R. W. Ghrist, C. J. Myatt, M. J. Holland, E. A. Cornell, and C. E. Wieman. Coherence, correlations, and collisions: What one learns about Bose-

- Einstein condensates from their decay. *Phys. Rev. Lett.*, 79:337–340, Jul 1997. (Cited on page 10.)
- [52] K. M. Mertes, J. W. Merrill, R. Carretero-González, D. J. Frantzeskakis, P. G. Kevrekidis, and D. S. Hall. Nonequilibrium dynamics and superfluid ring excitations in binary Bose-Einstein condensates. *Phys. Rev. Lett.*, 99:190402, Nov 2007. (Cited on page 11.)
- [53] Franco Dalfovo, Stefano Giorgini, Lev P. Pitaevskii, and Sandro Stringari. Theory of Bose-Einstein condensation in trapped gases. *Rev. Mod. Phys.*, 71:463–512, Apr 1999. (Cited on page 13.)
- [54] A. Muñoz Mateo and V. Delgado. Ground-state properties of trapped Bose-Einstein condensates: extension of the Thomas-Fermi approximation. *Phys. Rev. A*, 75:063610, Jun 2007. (Cited on page 13.)
- [55] Weizhu Bao. Ground states and dynamics of multicomponent Bose-Einstein condensates. *Multiscale Modeling & Simulation*, 2(2):210–236, 2004. (Cited on page 14.)
- [56] Weizhu Bao, Dieter Jaksch, and Peter A. Markowich. Numerical solution of the Gross-Pitaevskii equation for Bose-Einstein condensation. *Journal of Computational Physics*, 187(1):318 – 342, 2003. (Cited on pages 14 and 15.)
- [57] Xavier Antoine and Romain Duboscq. GPESLab, a Matlab toolbox to solve Gross-Pitaevskii equations i: Computation of stationary solutions. *Computer Physics Communications*, 185(11):2969 – 2991, 2014. (Cited on page 14.)
- [58] F. Chevy, V. Bretin, P. Rosenbusch, K. W. Madison, and J. Dalibard. Transverse breathing mode of an elongated Bose-Einstein condensate. *Phys. Rev. Lett.*, 88:250402, Jun 2002. (Cited on page 15.)
- [59] S. E. Pollack, D. Dries, R. G. Hulet, K. M. F. Magalhães, E. A. L. Henn, E. R. F. Ramos, M. A. Caracanhas, and V. S. Bagnato. Collective excitation

- of a Bose-Einstein condensate by modulation of the atomic scattering length. *Phys. Rev. A*, 81:053627, May 2010. (Cited on page 15.)
- [60] L. Salasnich, A. Parola, and L. Reatto. Effective wave equations for the dynamics of cigar-shaped and disk-shaped bose condensates. *Phys. Rev. A*, 65:043614, Apr 2002. (Cited on pages 15 and 16.)
- [61] Luis E. Young-S., L. Salasnich, and S. K. Adhikari. Dimensional reduction of a binary Bose-Einstein condensate in mixed dimensions. *Phys. Rev. A*, 82:053601, Nov 2010. (Cited on page 15.)
- [62] A. M. Kamchatnov and V. S. Shchesnovich. Dynamics of Bose-Einstein condensates in cigar-shaped traps. *Phys. Rev. A*, 70:023604, Aug 2004. (Cited on page 15.)
- [63] Elliott H. Lieb and Werner Liniger. Exact analysis of an interacting Bose gas. I. the general solution and the ground state. *Phys. Rev.*, 130:1605–1616, May 1963. (Cited on page 16.)
- [64] M. Girardeau. Relationship between systems of impenetrable bosons and fermions in one dimension. *Journal of Mathematical Physics*, 1(6):516–523, nov 1960. (Cited on page 16.)
- [65] Belén Paredes, Artur Widera, Valentin Murg, Olaf Mandel, Simon Fölling, Ignacio Cirac, Gora V. Shlyapnikov, Theodor W. Hänsch, and Immanuel Bloch. Tonks–Girardeau gas of ultracold atoms in an optical lattice. *Nature*, 429(6989):277–281, may 2004. (Cited on page 16.)
- [66] Weizhu Bao, Dieter Jaksch, and Peter A. Markowich. Numerical solution of the Gross–Pitaevskii equation for Bose–Einstein condensation. *Journal of Computational Physics*, 187(1):318–342, may 2003. (Cited on page 17.)

- [67] Xavier Antoine and Romain Duboscq. Gpelab, a matlab toolbox to solve gross-pitaevskii equations ii: Dynamics and stochastic simulations. *Computer Physics Communications*, 193:95–117, 2015. (Cited on page 17.)
- [68] Weizhu Bao and Jie Shen. A fourth-order time-splitting Laguerre–Hermite pseudospectral method for Bose-Einstein condensates. *SIAM Journal on Scientific Computing*, 26(6):2010–2028, jan 2005. (Cited on page 18.)
- [69] Daniel A Steck. Rubidium 87 D line data, 2001. (Cited on pages 20, 30, 34, 43, and 44.)
- [70] B.H. Bransden and C.J. Joachain. *Physics of Atoms and Molecules*. Pearson Education. Prentice Hall, 2003. (Cited on pages 20 and 21.)
- [71] E. Merzbacher. *Quantum Mechanics*. Wiley, 1998. (Cited on page 21.)
- [72] G. Breit and I. I. Rabi. Measurement of nuclear spin. *Phys. Rev.*, 38:2082–2083, Dec 1931. (Cited on page 21.)
- [73] Valentin Ivannikov. *Analysis of a trapped atom clock with losses*. PhD thesis, Swinburne university of technology, Melbourne, Australia, 2013. (Cited on pages 23, 69, 76, 77, 83, 88, and 128.)
- [74] T. Bergeman, Gidon Erez, and Harold J. Metcalf. Magnetostatic trapping fields for neutral atoms. *Physical Review A*, 35(4):1535–1546, feb 1987. (Cited on pages 24 and 25.)
- [75] Harold J. Metcalf and Peter van der Straten. *Laser Cooling and Trapping*. Springer New York, 1999. (Cited on pages 25, 29, and 30.)
- [76] J. Pérez-Ríos and A. S. Sanz. How does a magnetic trap work? *American Journal of Physics*, 81(11):836–843, nov 2013. (Cited on page 25.)

- [77] C. Henkel, S. Pötting, and M. Wilkens. Loss and heating of particles in small and noisy traps. *Applied Physics B*, 69(5-6):379–387, dec 1999. (Cited on page 27.)
- [78] D. M. Harber, J. M. McGuirk, J. M. Obrecht, and E. A. Cornell. *Journal of Low Temperature Physics*, 133(3/4):229–238, 2003. (Cited on page 27.)
- [79] M. P. A. Jones, C. J. Vale, D. Sahagun, B. V. Hall, and E. A. Hinds. Spin coupling between cold atoms and the thermal fluctuations of a metal surface. *Phys. Rev. Lett.*, 91:080401, Aug 2003. (Cited on page 27.)
- [80] Yu ju Lin, Igor Teper, Cheng Chin, and Vladan Vuletić. Impact of the Casimir-Polder potential and Johnson noise on Bose-Einstein condensate stability near surfaces. *Physical Review Letters*, 92(5), feb 2004. (Cited on page 27.)
- [81] H. Ott, J. Fortagh, G. Schlotterbeck, A. Grossmann, and C. Zimmermann. Bose-Einstein condensation in a surface microtrap. *Physical Review Letters*, 87(23), nov 2001. (Cited on page 27.)
- [82] Mikhail Egorov. *Coherence and collective oscillations of a two-component Bose-Einstein condensate*. PhD thesis, Swinburne university of technology, Melbourne, Australia, 2012. (Cited on pages 28, 40, 69, 75, 76, 77, 83, 89, and 128.)
- [83] J. Dalibard and C. Cohen-Tannoudji. Laser cooling below the Doppler limit by polarization gradients: simple theoretical models. *Journal of the Optical Society of America B*, 6(11):2023, nov 1989. (Cited on page 32.)
- [84] D. M. Harber, H. J. Lewandowski, J. M. McGuirk, and E. A. Cornell. Effect of cold collisions on spin coherence and resonance shifts in a magnetically trapped ultracold gas. *Phys. Rev. A*, 66:053616, Nov 2002. (Cited on pages 35 and 85.)

- [85] Iurii Mordovin. *Radio-frequency induced association of molecules in ^{87}Rb* . PhD thesis, Swinburne university of technology, Melbourne, Australia, 2015. (Cited on pages 43 and 45.)
- [86] R. Loudon. *The quantum theory of light*. Clarendon Press, 1973. (Cited on page 43.)
- [87] G. Reinaudi, T. Lahaye, Z. Wang, and D. Guéry-Odelin. Strong saturation absorption imaging of dense clouds of ultracold atoms. *Optics Letters*, 32(21):3143, oct 2007. (Cited on page 44.)
- [88] R. P. Anderson, C. Ticknor, A. I. Sidorov, and B. V. Hall. Spatially inhomogeneous phase evolution of a two-component Bose-Einstein condensate. *Physical Review A*, 80(2), aug 2009. (Cited on pages 49, 66, and 76.)
- [89] Lev Davidovich Landau and Evgenii Lifshits. *Non-Relativistic Theory*. (Cited on page 49.)
- [90] Ettore Majorana. Atomi orientati in campo magnetico variabile. *Il Nuovo Cimento*, 9(2):43–50, feb 1932. (Cited on page 49.)
- [91] W. M. Itano, J. C. Bergquist, J. J. Bollinger, J. M. Gilligan, D. J. Heinzen, F. L. Moore, M. G. Raizen, and D. J. Wineland. Quantum projection noise: Population fluctuations in two-level systems. *Phys. Rev. A*, 47:3554–3570, May 1993. (Cited on page 54.)
- [92] A. Sørensen, L.-M. Duan, J. I. Cirac, and P. Zoller. *Nature*, 409(6816):63–66, jan 2001. (Cited on page 54.)
- [93] A. Messiah. *Quantum Mechanics*. Dover books on physics. Dover Publications, 1961. (Cited on page 54.)
- [94] Norman Ramsey. *Molecular Beams*. Oxford University Press (OUP), jan 1986. (Cited on page 57.)

-
- [95] S.M. Barnett and P.M. Radmore. *Methods in Theoretical Quantum Optics*. Oxford Series in Optical and Imaging Sciences. Clarendon Press, 2002. (Cited on page 60.)
- [96] Roy J. Glauber. Coherent and incoherent states of the radiation field. *Phys. Rev.*, 131:2766–2788, Sep 1963. (Cited on page 61.)
- [97] C. Gardiner and P. Zoller. *Quantum Noise: A Handbook of Markovian and Non-Markovian Quantum Stochastic Methods with Applications to Quantum Optics*. Springer Series in Synergetics. Springer, 2004. (Cited on page 61.)
- [98] M. Lewenstein and L. You. Quantum phase diffusion of a Bose-Einstein condensate. *Phys. Rev. Lett.*, 77:3489–3493, Oct 1996. (Cited on page 62.)
- [99] B. Opanchuk, M. Egorov, S. Hoffmann, A. I. Sidorov, and P. D. Drummond. Quantum noise in three-dimensional BEC interferometry. *EPL (Europhysics Letters)*, 97(5):50003, 2012. (Cited on page 62.)
- [100] Michael W. Jack. Decoherence due to three-body loss and its effect on the state of a Bose-Einstein condensate. *Phys. Rev. Lett.*, 89:140402, Sep 2002. (Cited on page 62.)
- [101] B. Opanchuk and P. D. Drummond. Functional Wigner representation of quantum dynamics of Bose-Einstein condensate. *Journal of Mathematical Physics*, 54(4):042107, apr 2013. (Cited on page 64.)
- [102] M. Egorov, R. P. Anderson, V. Ivannikov, B. Opanchuk, P. Drummond, B. V. Hall, and A. I. Sidorov. Long-lived periodic revivals of coherence in an interacting Bose-Einstein condensate. *Phys. Rev. A*, 84:021605, Aug 2011. (Cited on pages 66, 69, 76, 81, 84, 90, and 95.)
- [103] A. Sinatra, Y. Castin, and E. Witkowska. Nondiffusive phase spreading of a Bose-Einstein condensate at finite temperature. *Physical Review A*, 75(3), mar 2007. (Cited on pages 66 and 123.)

- [104] C. Solaro, A. Bonnin, F. Combes, M. Lopez, X. Alauze, J.-N. Fuchs, F. Piéchon, and F. Pereira Dos Santos. Competition between spin echo and spin self-rephasing in a trapped atom interferometer. *Phys. Rev. Lett.*, 117:163003, Oct 2016. (Cited on page 85.)
- [105] C. Lhuillier and F. Laloë. Transport properties in a spin polarized gas, II. *Journal de Physique*, 43(2):225–241, 1982. (Cited on page 86.)
- [106] EP Bashkin. Spin waves in polarized paramagnetic gases. *JETP Lett*, 33(1), 1981. (Cited on page 86.)
- [107] PA Altin, Gordon McDonald, Daniel Doering, JE Debs, TH Barter, JD Close, NP Robins, SA Haine, TM Hanna, and RP Anderson. Optically trapped atom interferometry using the clock transition of large ^{87}Rb Bose-Einstein condensates. *New Journal of Physics*, 13(6):065020, 2011. (Cited on pages 87, 88, and 89.)
- [108] B.D. Josephson. Possible new effects in superconductive tunnelling. *Physics Letters*, 1(7):251–253, jul 1962. (Cited on page 97.)
- [109] Juha Javanainen. Oscillatory exchange of atoms between traps containing Bose condensates. *Phys. Rev. Lett.*, 57:3164–3166, Dec 1986. (Cited on page 98.)
- [110] G. J. Milburn, J. Corney, E. M. Wright, and D. F. Walls. Quantum dynamics of an atomic Bose-Einstein condensate in a double-well potential. *Phys. Rev. A*, 55:4318–4324, Jun 1997. (Cited on page 98.)
- [111] A. Smerzi, S. Fantoni, S. Giovanazzi, and S. R. Shenoy. Quantum coherent atomic tunneling between two trapped Bose-Einstein condensates. *Phys. Rev. Lett.*, 79:4950–4953, Dec 1997. (Cited on pages 98 and 101.)
- [112] R Gati and M K Oberthaler. A bosonic Josephson junction. *Journal of Physics B: Atomic, Molecular and Optical Physics*, 40(10):R61–R89, may 2007. (Cited on pages 99 and 100.)

-
- [113] Michael Albiez, Rudolf Gati, Jonas Fölling, Stefan Hunsmann, Matteo Cristiani, and Markus K. Oberthaler. Direct observation of tunneling and nonlinear self-trapping in a single bosonic Josephson junction. *Phys. Rev. Lett.*, 95:010402, Jun 2005. (Cited on page 99.)
- [114] Janne Ruostekoski and Dan F Walls. Bose-Einstein condensate in a double-well potential as an open quantum system. *Physical Review A*, 58(1):R50, 1998. (Cited on page 100.)
- [115] Srikanth Raghavan, Augusto Smerzi, Stefano Fantoni, and SR Shenoy. Coherent oscillations between two weakly coupled Bose-Einstein condensates: Josephson effects, π oscillations, and macroscopic quantum self-trapping. *Physical Review A*, 59(1):620, 1999. (Cited on pages 100 and 102.)
- [116] G. J. Milburn, J. Corney, E. M. Wright, and D. F. Walls. Quantum dynamics of an atomic Bose-Einstein condensate in a double-well potential. *Phys. Rev. A*, 55:4318–4324, Jun 1997. (Cited on page 100.)
- [117] Erich J. Mueller, Tin-Lun Ho, Masahito Ueda, and Gordon Baym. Fragmentation of Bose-Einstein condensates. *Phys. Rev. A*, 74:033612, Sep 2006. (Cited on page 101.)
- [118] N Bogoliubov. On the theory of superfluidity. *J. Phys*, 11(1):23, 1947. (Cited on page 101.)
- [119] Masahiro Kitagawa and Masahito Ueda. Squeezed spin states. *Phys. Rev. A*, 47:5138–5143, Jun 1993. (Cited on page 103.)
- [120] Tilman Zibold, Eike Nicklas, Christian Gross, and Markus K. Oberthaler. Classical bifurcation at the transition from Rabi to Josephson dynamics. *Physical Review Letters*, 105(20), nov 2010. (Cited on page 103.)
- [121] M. J. Steel, M. K. Olsen, L. I. Plimak, P. D. Drummond, S. M. Tan, M. J. Collett, D. F. Walls, and R. Graham. Dynamical quantum noise in trapped

- Bose-Einstein condensates. *Phys. Rev. A*, 58:4824–4835, Dec 1998. (Cited on page 106.)
- [122] Alice Sinatra, Carlos Lobo, and Yvan Castin. Classical-field method for time dependent Bose-Einstein condensed gases. *Phys. Rev. Lett.*, 87:210404, Nov 2001. (Cited on page 106.)
- [123] D. Witthaut, E. M. Graefe, and H. J. Korsch. Towards a generalized Landau-Zener formula for an interacting Bose-Einstein condensate in a two-level system. *Phys. Rev. A*, 73:063609, Jun 2006. (Cited on page 111.)
- [124] Max F. Riedel, Pascal Böhi, Yun Li, Theodor W. Hänsch, Alice Sinatra, and Philipp Treutlein. Atom-chip-based generation of entanglement for quantum metrology. *Nature*, 464(7292):1170–1173, mar 2010. (Cited on page 111.)
- [125] BD Esry. Hartree-Fock theory for Bose-Einstein condensates and the inclusion of correlation effects. *Physical Review A*, 55(2):1147, 1997. (Cited on page 112.)
- [126] E. Nicklas, W. Muessel, H. Strobel, P. G. Kevrekidis, and M. K. Oberthaler. Nonlinear dressed states at the miscibility-immiscibility threshold. *Physical Review A*, 92(5), nov 2015. (Cited on pages 114 and 134.)
- [127] Kean Loon Lee, Nils B. Jørgensen, I-Kang Liu, Lars Wacker, Jan J. Arlt, and Nick P. Proukakis. Phase separation and dynamics of two-component Bose-Einstein condensates. *Phys. Rev. A*, 94:013602, Jul 2016. (Cited on page 114.)

Publications

L. Rosales-Zárate, R. Y. Teh, S. Kieseewetter, A. Brolis, K. Ng and M. D. Reid.
Decoherence of Einstein–Podolsky–Rosen steering. *J. Opt. Soc. Am. B* 32,
A82-A91 (2015).